Best
Available
Copy

UNCLASSIFIED

AD 257 514

Reproduced
by the

ARMED SERVICES TECHNICAL INFORMATION AGENCY
ARLINGTON HALL STATION
ARLINGTON 12, VIRGINIA



UNCLASSIFIED

NOTICE: When government or other drawings, specifications or other data are used for any purpose other than in connection with a definitely related government procurement operation, the U. S. Government thereby incurs no responsibility, nor any obligation whatsoever; and the fact that the Government may have formulated, furnished, or in any way supplied the said drawings, specifications, or other data is not to be regarded by implication or otherwise as in any manner licensing the holder or any other person or corporation, or conveying any rights or permission to manufacture, use or sell any patented invention that may in any way be related thereto.

25514
CATALOGED BY ASTIA
AS AD No. _____
NOX

RESEARCH REPORT No. 60-91

FUNDAMENTALS OF ULTRASONIC WELDING

PHASE II

J. Byron Jones
Nicholas Maropis
John G. Thomas
Dennison Bancroft

ASTIA
JUN 13 1961

AEROPROJECTS INCORPORATED
WEST CHESTER, PENNSYLVANIA

December, 1960

Released to ASTIA by the
Bureau of NAVAL WEAPONS
without restriction.

Prepared under
Contract NOas 59-6070-c

Submitted to
BUREAU OF NAVAL WEAPONS
WASHINGTON 25, D.C.

$2.50

FUNDAMENTALS OF ULTRASONIC WELDING
PHASE II

by

J. Byron Jones
Nicholas Marcpis
John G. Thomas
Dennison Bancroft

December 1960

FINAL REPORT
(RR-60-91)

Submitted to
Bureau of Naval Weapons

Covering Period
December 1, 1958 - February 1, 1960

17200

AEROPROJECTS INCORPORATED
West Chester, Pennsylvania

FOREWORD

This report covers the work accomplished under Phase II of a study of the fundamentals of ultrasonic welding by Aeroprojects Incorporated under Navy Contract NOas 59-6070-c. Mr. R. M. Gustafson of the Materials Branch, Airborne Equipment Division, Bureau of Naval Weapons, provided liaison and technical assistance. The Contract was administered through the Bureau of Naval Weapons Representative, Verton, Morton, Pennsylvania.

The authors acknowledge with appreciation the interest, cooperation, assistance, and criticism of: Dr. William C. Elmore, Chairman, Department of Physics, Swarthmore College; Dr. Ernest F. Nippes, Director of Welding Research, Department of Metallurgical Engineering, Rensselaer Polytechnic Institute, Dr. Frederick N. Rhines, Head Professor, Metallurgical Research Laboratories, University of Florida; and Dr. George S. Ansell, Research Professor of Metallurgy, Rensselaer Polytechnic Institute.

ABSTRACT

This Phase II extends earlier research which developed instrumentation and techniques to permit the work here reported. Photoelastic investigations show that ultrasonic welds are initiated as a result of vibration-induced interfacial shear stresses combining with the interfacial shear stresses resulting from the normal clamping force to produce alternately, on the side toward which the vibratory force acts, islands of local slip within an area of elastic strain. A proper clamping force is productive of a best impedance match to effect energy delivery into the weld locale. Sheet thickness and the Vickers microhardness indentation number are combined to permit a first approximation of the energy required to produce welds between metallic sheets. Optical and electron microscope observations and pertinent discussion are presented. Autoradiographic techniques are used to follow surface film dispersion, and it is suggested that dispersion strengthening may be associated with ultrasonic welds. Bonds are not uncommonly characterized by internal deformations without significant external deformation. Recrystallization can occur in ultrasonic welds, but does not appear to be a common denominator. The temperature achieved during vibratory welding is measured to be in the range of about 35 to 50% of the absolute melting temperature. No evidence of melting was observed in any monometallic weld.

SUMMARY

Since ultrasonic or vibratory welding is a dynamic force-induced process, the normal and the shear stress distributions at the weld interface and at the tip-work interface were determined by comprehensive photoelastic analysis for four discrete loading conditions critical in generating a vibratory weld between two sheets. It is shown that local slip--within an area of elastic strain--and not gross sliding undoubtedly occurs. Seven factors basic to the ultrasonic welding process were deduced and are discussed.

The energy associated with producing an ultrasonic weld was investigated. Line power, electrical power to the transducers, and vibratory power to the weld locale are differentiated. The significance of the minimal power value in the power to clamping force welding threshold relationship is determined and analyzed by means of surface plots, and it is concluded that a proper clamping force is productive of a best impedance match between sonotrode tip and weldment. An equation is developed which will permit calculation of the terminal impedance of a vibratory energy coupler. Preliminary determination of the resistive and reactive components of weld impedance in copper and aluminum suggest avenues for improving the process.

Analysis of experimentally determined data relating sheet thickness, material hardness, and vibratory energy requisite to producing welds in several materials evolved an equation relating these parameters which, for the first time, permits approximations of welding machine characteristics for joining previously untried metals or alloys of varying thicknesses. Using the Vickers microhardness indentation number of a metal as a measure of weldability is justified because room-temperature property relationships maintain at similar fractions of the absolute melting temperature and because temperature measurements during welding show that the weld zone reaches about 35-50% of the absolute melting temperature for all materials investigated.

Ultrasonic welds in several materials were studied by means of optical and electron microscopy, and autoradiographic techniques were utilized to follow surface film dispersion in such dispersion in such welds. Bonds are characterized by plastic deformation suggestive of ultrasonic plasticity and by dispersion of surface coatings possibly productive of dispersion strengthening in the weld zone. Recrystallization, while not unusual, is not a common denominator in these welds, and subgrain formation sometimes occurs in the region near the weld interface. Welds fail in a ductile manner. No evidence of melting was observed.

TABLE OF CONTENTS

		Page
	FOREWORD	i
	ABSTRACT	ii
	SUMMARY	iii
I	INTRODUCTION	1
II	STRESS DISTRIBUTION IN THE WELD ZONE	3
	A. Technical Approach	3
	B. Results	5
	C. Interpretation of Results	20
III	ENERGY DELIVERED TO THE WELD ZONE	26
	A. Electrical Power to Transducer	29
	B. Acoustical Power	30
	C. Significance of Threshold Curves	32
	D. Weld Zone Impedance	49
IV	MATERIAL PROPERTIES AND WELDABILITY	59
	A. Experimental Equipment, Materials, and Procedures	61
	B. Energy Required to Produce Welds	66
	C. Temperature in the Weld Zone	69
	D. Effect of Surface Condition on Weldability	73
	E. Welding Energy as a Function of Hardness and Thickness.	77
V	METALLURGY AND INTERFACIAL DISTURBANCE	90
	A. Optical Studies	91
	B. Examination of Weldments by Autoradiographic Techniques	100
	C. Characterization of Weldments by Electron Microscopy	106
	D. Results	108
VI	CONCLUSIONS	135
	A. Photoelastic	135
	B. Energy Delivered to the Weld Zone	136
	C. Material Properties and Weldability	137
	D. Metallurgy and Interfacial Disturbance	138
APPENDIX A	PHOTOELASTIC STRESS ANALYSIS	139
B	INVESTIGATION OF CONTACT SURFACE SHEARING STRESS	154
C	MEASUREMENT OF TRANSMITTED ULTRASONIC POWER	157
D	DETERMINATION OF THE TRANSDUCER TERMINAL IMPEDANCE	161
E	THE POWER-FREQUENCY INTERACTION	165
REFERENCES		168

LIST OF FIGURES

Figure		Page
1	Stress Distributions in the Model Just Below the Tip - Normal Load Only	7
2	Stress Distributions in the Model Just Below the Tip - Normal Load Plus Transverse Thrust Before Sliding	8
3	Stress Distribution Just Below Tip - Normal Load Plus Transverse Thrust After Sliding	9
4	Stress Distribution in the Model Just Below the Tip - Transverse Force Reversed After Slip	10
5	Stress Distributions at the Model Interface - Normal Load Only	11
6	Stress Distributions at the Model Interface - Normal Load Plus Transverse Thrust, No Sliding	12
7	Stress Distribution at the Model Interface - Normal Load Plus Transverse Thrust After Sliding	13
8	Stress Distribution at the Model Interface - Transverse Force Reversed After Sliding	14
9	Ultrasonic Weld Produced Between Two Strips of 2014-T6 Aluminum Sheet	20
10	Ratio of Shearing Stress to Normal Stress as a Function of Normal Stress for Various Normal Loads	21
11	Block Diagram of Ultrasonic Welding System	26
12	Threshold Curve for Welding 0.020-Inch 1100-H18 Aluminum Alloy	28
13	Threshold Curve for Welding 0.009-Inch 1100-H18 Aluminum Alloy	34
14	Threshold Curve for Welding 0.005-Inch Cold-Rolled Stainless Steel	34
15	Threshold Curve for Welding 0.010-Inch Annealed 302 Stainless Steel	35
16	Threshold Curve for Welding 0.020-Inch Half-Hard Copper.	35

LIST OF FIGURES (Continued)

Figure		Page
17	Method for Measuring Deformation Data	36
18	Effect of Clamping Force and Power on Tensile-Shear Strength of a Weld in 0.020-Inch 1100-H18 Aluminum Alloy.	39
19	Effect of Clamping Force and Power on Tensile-Shear Strength of a Weld in 0.009-Inch 1100-H18 Aluminum Alloy.	39
20	Effect of Clamping Force and Power on Tensile-Shear Strength of a Weld in 0.005-Inch 302 Cold-Rolled Stainless Steel	40
21	Effect of Clamping Force and Power on Tensile-Shear Strength of a Weld in 0.010-Inch Annealed Stainless Steel	40
22	Effect of Clamping Force and Power on Tensile-Shear Strength of a Weld in 0.020-Inch Half-Hard Copper	41
23	Effect of Clamping Force and Power on Cross-Tension Strength of a Weld in 0.020-Inch 1100-H18 Aluminum Alloy.	41
24	Effect of Clamping Force and Power on Cross-Tension Strength of a Weld in 0.009-Inch 1100-H18 Aluminum Alloy.	42
25	Effect of Clamping Force and Power on Cross-Tension Strength of a Weld in 0.005-Inch 302 Stainless Steel . .	42
26	Effect of Clamping Force and Power on Cross-Tension Strength of a Weld in 0.010-Inch 302 Stainless Steel . .	43
27	Effect of Clamping Force and Power on Cross-Tension Strength of a Weld in 0.020-Inch Half-Hard Copper	43
28	Effect of Clamping Force and Power on Weld Area in 0.020-Inch 1100-H18 Aluminum Alloy	44
29	Effect of Clamping Force and Power on Weld Area in 0.005-Inch Cold-Rolled 302 Stainless Steel	44
30	Effect of Clamping Force and Power on Weld Area in 0.010-Inch 302 Stainless Steel	45
31	Effect of Clamping Force and Power on Weld Area in 0.020-Inch Half-Hard Copper	45

LIST OF FIGURES (Continued)

Figure		Page
32	Effect of Clamping Force and Power on Thickness Deformation of a Weld in 0.020-Inch 1100-H18 Aluminum Alloy	46
33	Effect of Clamping Force and Power on Thickness Deformation of a Weld in 0.005-Inch Stainless Steel	46
34	Effects of Clamping Force and Power on Thickness Deformation of a Weld in 0.010-Inch Annealed 302 Stainless Steel.	47
35	Effect of Clamping Force and Power on Thickness Deformation of a Weld in 0.020-Inch Half-Hard Copper	47
36	Effect of Clamping Force and Power on Temperature in the Weld Area in 0.020-Inch 1100-H18 Aluminum Alloy	48
37	Effect of Clamping Force and Power on Temperature in the Weld Area in 0.009-Inch 1100-H18 Aluminum Alloy	48
38	Threshold Curve, with Typical Temperatures Noted at Interface, for Various Power and Clamping Force Levels for Welding 0.020-Inch Half-Hard OFHC Copper	49
39	The Transducer Instrumented with 21 Dynamic Strain Gages and Rotary Switch	50
40	Approximate Standing-Wave Ratio Data Obtained for 0.050-Inch 1100-H14 Aluminum	52
41	Approximate Standing-Wave Ratio Data Obtained for 0.032-Inch 2024-T3 Alclad	53
42	Approximate Standing-Wave Ratio Data Obtained For 0.032-Inch Copper	54
43	Resistive and Reactive Components of Weld Impedance in 0.020-Inch 1100-H18 Aluminum	56
44	Resistive and Reactive Components of Weld Impedance in 0.032-Inch Copper	57
45	Ratio of Weld Zone Impedance to Coupler Impedance for 0.020-Inch 1100-H18 Aluminum and 0.032-Inch Copper	58
46	Schematic of Lateral-Drive Welding System	62
47	Schematic of Reed-Wedge Welding System	62

LIST OF FIGURES (Continued)

Figure		Page
48	Comparison of Power Required to Weld Type 302 Stainless Steel and Nickel	78
49	Comparison of Power Required to Weld 1100-H18 and 1100-0 Aluminum Alloys	78
50	Total Acoustic Energy Required to Weld Several Materials with 28-Kilocycle Experimental Welding Array	81
51	Acoustic Energy Per Unit Weld Area Required to Weld Several Materials with 28-Kilocycle Experimental Welding Array	82
52	Acoustical Energy Required to Generate a Weld as a Function of Hardness with Parameter of Material Thickness	83
53	Acoustical Energy Required to Generate a Weld as a Function of Material Thickness with Parameter of Vickers Hardness	83
54	Acoustical Energy Required to Generate a Weld as a Function of Hardness with Parameter of Material Thickness	84
55	Acoustic Energy Required to Weld as a Function of Vickers Hardness with Parameters of Material Thickness	86
56	Sample Welds Between Strips of 2014-T6 Aluminum Alloy	92
57	Sample Welds Between Strips of Type 302 Stainless Steel	93
58	Ultrasonic Welds in 0.020-Inch 1100-H18 Aluminum Along the Threshold Curve	95
59	Ultrasonic Weld in 0.020-Inch "A" Nickel	96
60	Ultrasonic Weld in 0.008-Inch PH 15-7 Molybdenum Stainless Steel	96
61	Photomicrograph of Interpenetration of Mating Surfaces of 0.024-Inch 430 Stainless Steel and 0.028-Inch A-100-AT Titanium Alloy--Showing Structural Changes in the Titanium Alloy Resulting From Heat Generated During Ultrasonic Welding	97
62	Ultrasonic Weld in 0.080-Inch 2014-T6 Aluminum with 0.001-Inch 1100 Aluminum Foil Insert	97

LIST OF FIGURES (Continued)

Figure		Page
63	Photomicrograph of Ultrasonic Weld Between 0.030-Inch AISI-Type 0.2 Tool Steel (0.90% Carbon) and 0.030-Inch Armco Iron--Illustrating the Diffusion of Carbon into the Iron	99
64	Photomicrographs of 0.020-Inch Thickness of Titanium-8 Manganese Alloy Sections Taken Transversely and Longitudinally to the Vibratory Motion Occurring During Ultrasonic Welding--Showing Block-Like Orientation Effect	101
65	Photomicrographs of 0.025-Inch Thicknesses of 302 Stainless Steel Taken Transversely and Longitudinally to the Vibratory Motion Occurring During Ultrasonic Welding--Showing Block-Like Orientation Effect	102
66	Ultrasonic Welds in 0.012-Inch Inconel X in the Solution-Heat-Treated Condition	104
67	Interfacial Area of Ultrasonic Weld in Anodized (3000 Å) Aluminum	107
68	Schematic Representation of Cross Section of Positive Shadowed Replica	109
69	Optical Photomicrographs of Interfacial Areas in Ultrasonic Weld Between Two Sheets of 0.032-Inch Armco Ingot Iron	111
70	Electron Micrograph of Polished and Etched Iron Showing Considerable Subgrain Boundary Shear	112
71	Electron Micrograph of Polished and Etched Iron Showing Pitting From Etchant	113
72	Electron Micrograph of Polished and Etched Iron Showing Continuity of Interface Film	114
73	Electron Micrograph of Polished and Etched Iron Showing Subgrain Boundaries Near the Weld Zone	115
74	Optical Micrograph of Weld in 0.032-Inch Commercially Pure Copper	116
75	Electron Micrograph of Polished and Etched Copper Showing Finely Dispersed Surface Film Adjacent to Weld Interface	117

LIST OF FIGURES (Continued)

Figure		Page
76	Electron Micrograph of Polished and Etched Copper Showing Degradation of Original Weld Interface Film	118
77	Electron Micrograph of Polished and Etched Copper Showing Effective Dispersion of Weld Interface Film	119
78	Electron Micrograph of Copper Peeled Surface	121
79	Electron Micrograph of Copper Showing Cleavage Facets of the Fracture Surface of the Weld Interface	122
80	Electron Micrograph of Copper Showing Plastic Deformation Associated with Fracture	123
81	Electron Micrograph of Copper Showing Plastic Deformation Which Occurred During Failure	124
82	Electron Micrograph of Copper Showing Lower Ductility Near Center of Weld Zone	125
83	Optical Photomicrographs of Ultrasonic Welds in 0.032-Inch 1100-H14 Aluminum	126
84	Electron Micrograph of Polished and Etched Aluminum Showing Voids and Dispersed Material at Weld Interface	127
85	Electron Micrograph of Polished and Etched Aluminum Showing Degradation of Oxide Film at Weld Interface	128
86	Electron Micrograph of the Peeled Weld Surface of Aluminum	130
87	Electron Micrograph of the Peeled Weld Surface of Aluminum	131
88	Electron Micrograph of the Peeled Weld Surface of Aluminum	132
89	Electron Micrograph of Fracture Surface Across Weld Interface of Aluminum	133
90	Electron Micrograph of Fracture Surface Near the Weld Interface of Aluminum	134

LIST OF FIGURES (Concluded)

Figure		Page
A-1	Sign Conventions for Photoelastic Data	140
A-2	Resolution and Transformation of the Stress Tensor	141
A-3	Plot of Shearing Stress Slope $\partial\tau_{xy}/\partial_y$ as a Function of X	143
A-4	Sketch Showing the Path of Integration for Determining σ_x and σ_y at the Arbitrary Point x = a, y = 0.	144
A-5	Isochromatic Fringe Pattern and Isoclinic Lines	147
A-6	Superposition of Relevant Photoelastic Data	148
A-7	Hypothetical Sketch of Isochromatic Fringes (dotted lines) Superposed on Isoclinic Lines (solid lines) in a Photoelastic Model	150
A-8	Shearing Stress Distributions Within the Model	151
B-1	Schematic of Apparatus Used to Establish Maximum Supportable Shearing Stress	155

LIST OF TABLES

Table		Page
I	Loading Conditions and Locales For Photoelastic Analysis	6
II	Summary of Standing-Wave-Ratio (SWR) Data From Oscillograms	55
III	Room-Temperature Physical and Mechanical Properties of Materials Used in the Weldability Study	64
IV	Acoustic Properties of Selected Materials	65
V	Minimum Power Transmission Data For Welding Various Materials at 28 Kilocycles	67
VI	Minimum Power Transmission Data For Welding Various Materials at 15 Kilocycles	68
VII	Order of Weldability of Several Materials	70
VIII	Weld-Zone Temperatures Achieved in Representative Metals	72
IX	Scouting Investigation of Weld-Zone Temperatures Achieved in Metals of Special Interest	72
X	Tensile-Shear Strength Data From Latin Square Design Experiment on Aluminum Oxide Film Impregnated 0.0335-Inch High-Purity Aluminum	76
XI	Analysis of Variance For The Experimental Data Presented in Table I	76
XII	Machine Settings Used For Welding Samples Examined By Electron Microscopy	108
A-1	Sample of Numerical Data	149

I. INTRODUCTION

The objective of the several phases of this over-all research program is to develop a phenomenological theory of ultrasonic welding that will account for the observed effects and that can be used to improve the design of ultrasonic welding equipment and to extend its usefulness in joining the newer, high-temperature, corrosion-resistant materials of particular significance to the various military and atomic energy programs.

Phase I of this investigation, completed earlier (4)*, involved the development of special instrumentation and techniques implicit in excavating and interpreting information from observable interacting factors involved in the ultrasonic welding process. It included preliminary study of certain ultrasonic weld phenomena and considered the influence of material properties on weldability. In particular,

a. Accumulated evidence had shown that ultrasonic welding may be accomplished, at least in part, as a result of deformation at and near the interface being joined, it was clear that understanding the transient stresses producing such deformation is important. Therefore photoelastic techniques were considered and later developed, so that the internal dynamic stress pattern associated with the applied static and superimposed oscillating shear force associated with welding could be observed and photographed. A special strain frame for applying the requisite force system was devised and routinely utilized. Recourse to the laborious frozen stress technique was obviated by development of direct observation triaxially restrained photoelastic models. This work was carried far enough to establish its usefulness in studying this facet of the welding process.

b. Since it is self evident that a theory of the mechanism of vibratory welding must consider the energy required to produce a weld, the Phase I work considered avenues by which we could ascertain net power and the instantaneous values thereof in time, during which a weld was generated. No practical method for measuring ultrasonic power transmitted through metallic coupling rods was available, but analysis indicated a standing elastic wave measurement technique be suited to standard oscillographic data recording. The SWR method was developed, its validity established in calorimetric experiments, and its use reduced to routine. It is to be noted that this approach is inclusive: for example, when frequency, power, and its variation in time are known, such an ancillary variable as tip amplitude is easily obtained when there is reason to know it. More important, the actual weld impedance during formation can be ascertained, and this information is fundamental to developing both the process and the equipment to implement it. Consideration was

---

* Numbers in parentheses refer to LIST OF REFERENCES at end of report.

given to determining the energy passing through and beyond the weld zone, since this, too, is included but should be deducted from the transmitted ultrasonic power data determined by the SWR technique.

c. Since it is well known that there is a temperature rise of some magnitude during the formation of an ultrasonic weld, the need for reliable information on weld-zone heating and for correlating it with the process variables was obvious. Material properties are transiently affected by heat; recrystallization, diffusion, phase change, and the possible interaction of such normal metallurgical phenomena with vibratory stresses, all pointed to the need for a practical technique to determine transient temperatures at the weld zone interface. Accordingly, a single fine-wire thermocouple technique was developed to accomplish sensing, from which reproducible records were obtained with rapid-response equipment. The technique was utilized to obtain preliminary, but significant, information on the process variables--power, clamping force, and weld time--for copper, aluminum, and iron. The validity of the temperatures obtained was confirmed by means of a meltable insert technique.

d. Explorations were made into the characteristics of the interface disturbance routinely observed in ultrasonic welds in various materials. This facet of Phase I served to orient much of the work carried out in Phase II which is discussed in this report. An autoradiographic technique involving Beta emission was utilized experimentally as a candidate technique for studying interfacial displacements where standard metallography is inadequate. Lower-energy Beta radiation was deemed essential to obtaining meaningful information in the course of this Phase II research. Metal displacement, recrystallization, diffusion, phase transformation, and miscellaneous other effects were noted in various materials.

e. A statistical approach to define the relation of material properties to ultrasonic weldability was considered at length, but the complexity thereof and time involved appeared to be excessive. Success in developing the SWR method for measuring the net energy required to generate a weld suggested a less complex method; that an "order of weldability" in terms of energy and material thickness, should yield a correlation with one or more material properties which could be determined by systematic analysis of material properties data, including properties at temperatures. It was determined that the net energy involved in generating a weld of a unit area between, for example, two sheets of 0.001-in. thickness aluminum, and stainless steel, embraced a large range -- in the order of 1 to 100 watts, respectively, with copper sheets of the same thickness falling between.

II. STRESS DISTRIBUTION IN THE WELD ZONE

A. Technical Approach

In the course of investigating the vibration-induced stress distributions productive of ultrasonic welds, a strain frame was developed during Phase I for loading photoelastic models in a fashion that essentially duplicated any instantaneous loading condition associated with the actual accomplishment of such bonds between two pieces of sheet metal (4).

Triaxially restrained photoelastic models were developed which permitted direct observation of a changing stress pattern (4), and motion pictures showing the changing stress pattern, as can be seen with such triaxially restrained models, were obtained. It was observed that when the sonotrode tip reached the stick-slip condition, rapid and significant changes took place in the stress pattern. By using these models the laborious frozen-stress technique could be obviated, within practical limits.

Moreover, the simple plank model proved to be sufficiently similar to the triaxially restrained model to be used with reasonable accuracy for studying the static stress conditions associated with normal loading, normal plus transverse loading just prior to slip, and normal plus transverse loading just after slip.

A literature study disclosed information on point-loaded models (19,21,28,40), but nothing more analogous to the situation in ultrasonic welding geometry was found. It was decided that for an adequate understanding further study was required to differentiate between local slip and gross sliding. This was accomplished by analysis of photographic data obtained from photoelastic models loaded to provide evidence of both the normal stress (σ_y) and the shearing stress (τ_{xy}) distribution around the affected interface.

Normally, a photoelastic analysis is carried only far enough to obtain the maximum shearing stress gradient (by counting fringes). In this case, however, it is necessary to make a comprehensive analysis to evaluate the principal stresses. Accordingly, the following investigation was carried out.

Photoelastic plank models were loaded under these conditions:

a. Tip radius, R = 30t (equivalent to 3-in. tip radius on 0.050-in.-thick metal sheet)

b. Normal force, 300 lb

c. Lateral force at "stick-before-slip", 76-80 lb

d. Lateral force just after slip, indeterminate

e. Lateral force after slip was reversed, 50-55 lb.

Fringe patterns were photographed by circularly polarized light while isoclinic patterns were photographed at 15-deg angular increments with plane polarized light. From these data, the normal and shear stress values were obtained analytically by utilizing equations from Lee ( ) as follows:

$$\tau_{xy} = 1/2\,(\sigma_1 - \sigma_2) \sin 2\phi\,, \tag{1}$$

$$\sigma_{x_1} - \sigma_{x_o} + \int_{x=0}^{x=x_1} \frac{\partial \tau_{xy}}{\partial_y}\, dx = 0, \tag{2}$$

$$\sigma_y - \sigma_x \pm \sqrt{(\sigma_1 - \sigma_2)^2 - (4\tau_{xy})^2}\,, \tag{3}$$

where

τ_{xy} = shear stress

$\sigma_1 - \sigma_2$ = difference in the principal stresses

ϕ = angle of isoclinic

σ_{x_1} = component of principal stresses along the x axis

σ_{x_o} = component of principal stresses at the point of origin, σ_y

$\frac{\partial \tau_{xy}}{\partial_y}$ = shear stress gradient in y direction at point of interest

σ_y = the normal stress.

The analytical procedures utilized in making these relatively complete photoelastic investigations are discussed in Appendix A of this report.

B. Results

Table I is a summary of the loading conditions under which the various stress components were determined.

Figures 1 through 8 contain all the numerical results of the photoelastic investigation. The accuracy of these data permit reading the stress patterns to $\pm$ 0.05 fringe, and the orientation of the isoclinics to about $\pm 1^\circ$. From Eq (1) we infer that the magnitude of the error, $\delta \tau_{xy}$, in τ_{xy} is given by

$$\delta \tau_{xy} = \left\{ 1/4 \sin^2 2\phi \left[\delta(\sigma_1 - \sigma_2) \right]^2 + (\sigma_1 - \sigma_2)^2 \cos^2 2\phi \, (\delta \phi)^2 \right\}^{1/2}, \qquad (4)$$

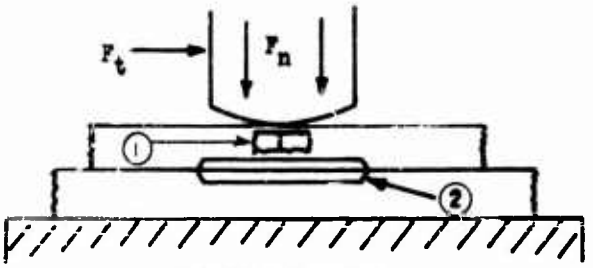
which at worst is about 0.05 fringe. The values of τ_{xy} are of the order of 1.0 fringe, so that the accuracy might be expected to be about 5% for the larger values of this quantity. Actually, this estimate appears somewhat optimistic, for, as has been noted, the over-all accuracy of the figures may be checked by integrating the shearing stress across the model and comparing this result with the known transverse thrust. The maximum discrepancy thus detected was somewhat less than 10%.

The accuracy of the curves for σ_x and σ_y is more difficult to estimate, since the curves were determined, as noted previously, by a numerical differentiation followed by a numerical integration. The errors introduced in the first process tend to be reduced in the second, but it is clearly not easy to estimate magnitudes. In the case of σ_y, it is possible to check its integral across the model against the known normal load, again to an accuracy of somewhat less than 10%. Accuracy of about 10% of the maximum fringe value, or of the order of 0.5 fringe at the weld interface, and of 3 fringes near the tip can be inferred.

Before analysis of the data is presented, it is necessary to distinguish between "sliding", that is, gross displacement of one member of the model weldment with respect to the other, and "slip", a local relative interfacial displacement at some small island region of the interface together with a lack of such displacement at other surrounding regions. Both slip and sliding result in a relief of interfacial shearing stress, which is different at different points on the interface. With a local slip, relief of stress must be accompanied by a growth of stress in some other region. Furthermore, in slip, the magnitude of the relative displacement is very small and frequently may not exceed values permitted by gross elastic distortion of the material. In both processes, however,

Table I

LOADING CONDITIONS AND LOCALES FOR PHOTOELASTIC ANALYSIS



Reaction Element

Case	Applied Condition	Stress Under Tip One	Stress at Interface Two
I	F_n, Normal Force, 300 lb	σ_y, Normal	σ_y, Normal
		σ_x, Transverse	σ_x, Resolved Transverse
		τ_{xy}, Shear	τ_{xy}, Shear
II	F_n, Normal Force, 300 lb, plus F_t, Transverse Force before Slip, 76-lb machine load 52-lb model load	σ_y, Normal	σ_y, Normal
		σ_x, Transverse	σ_x, Resolved Transverse
		τ_{xy}, Shear	τ_{xy}, Shear
III	F_n, Normal Force, 300 lb, plus F_t, Transverse Force after Slip (statically indeterminate)	σ_y, Normal	σ_y, Normal
		σ_x, Transverse	σ_x, Transverse
		τ_{xy}, Shear	τ_{xy}, Shear
IV	F_n, Normal Force, 300 lb, plus F_t, Transverse Force Reversed after Slip, 52 lb	σ_y, Normal	σ_y, Normal
		σ_x, Transverse	σ_x, Resolved Transverse
		τ_{xy}, Shear	τ_{xy}, Shear

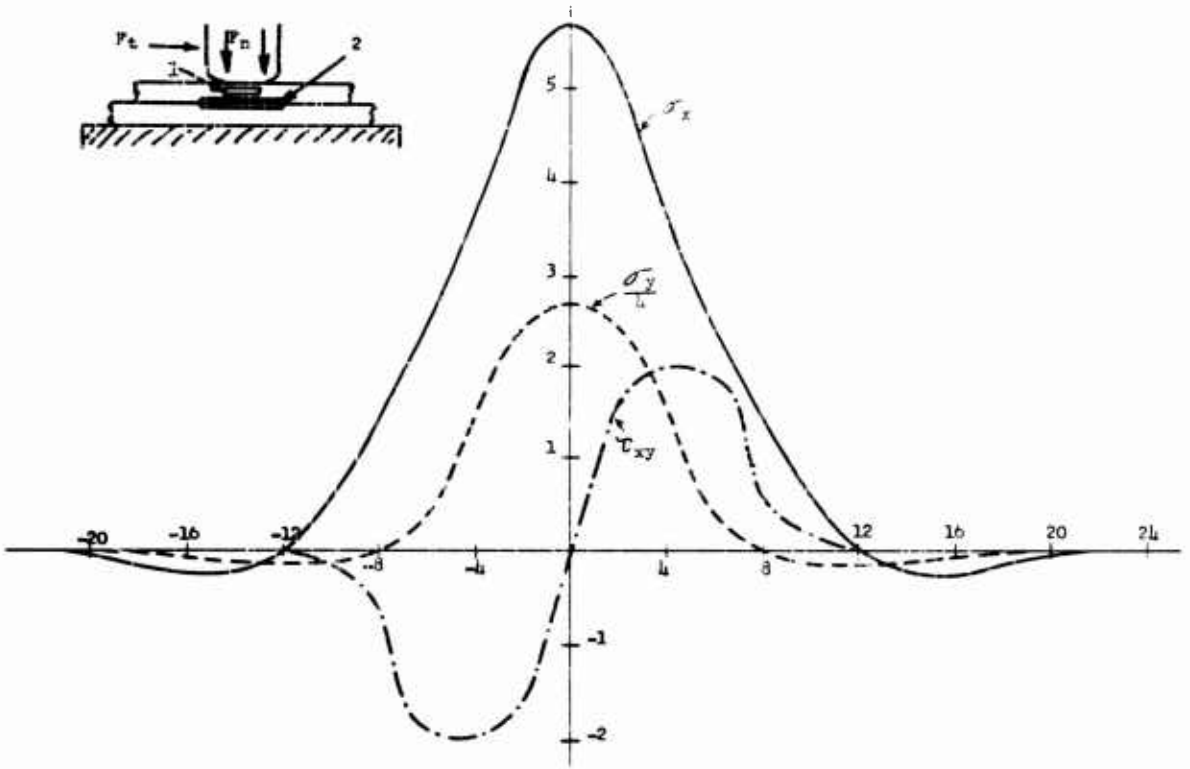


Fig. 1: STRESS DISTRIBUTIONS IN THE MODEL JUST BELOW THE TIP - NORMAL LOAD ONLY
Case 1, Tip, of Table I

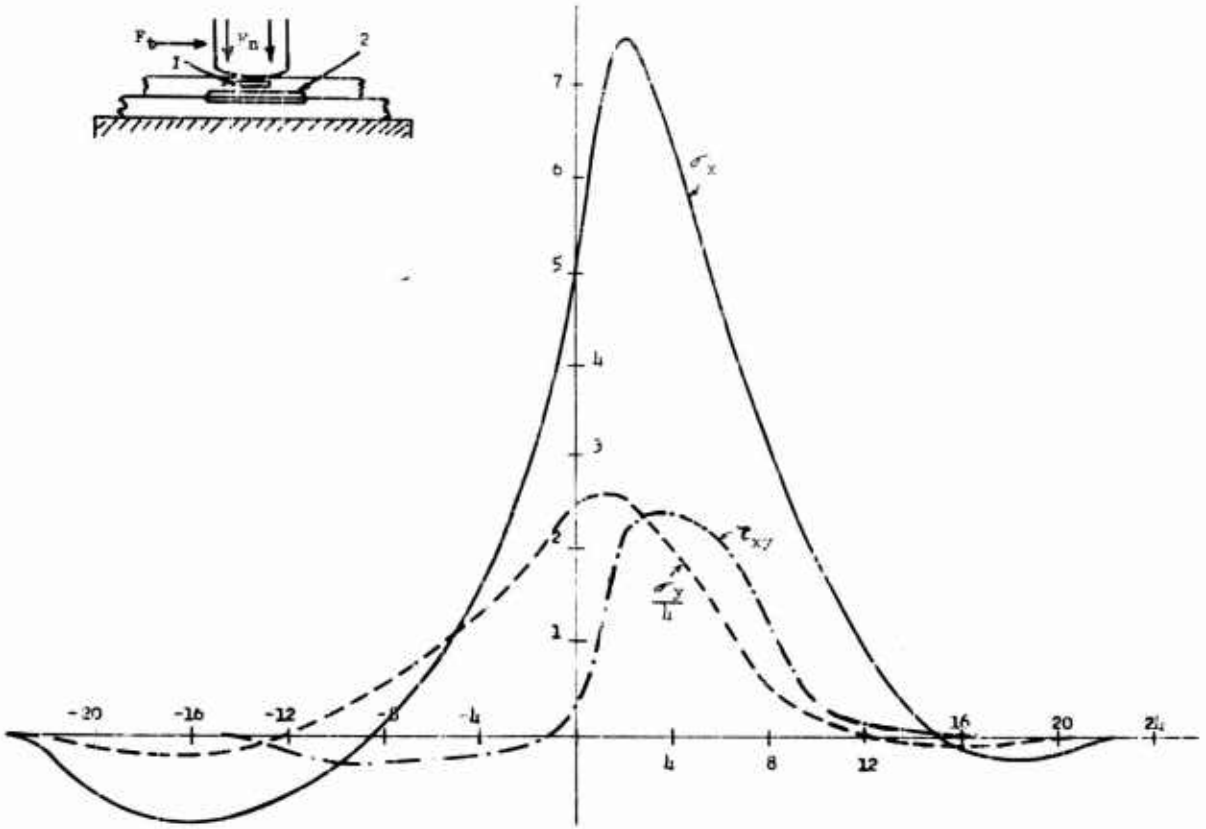


Fig. 2: STRESS DISTRIBUTIONS IN THE MODEL JUST BELOW THE TIP-NORMAL LOAD PLUS TRANSVERSE THRUST BEFORE SLIDING

Case II, Tip, of Table I

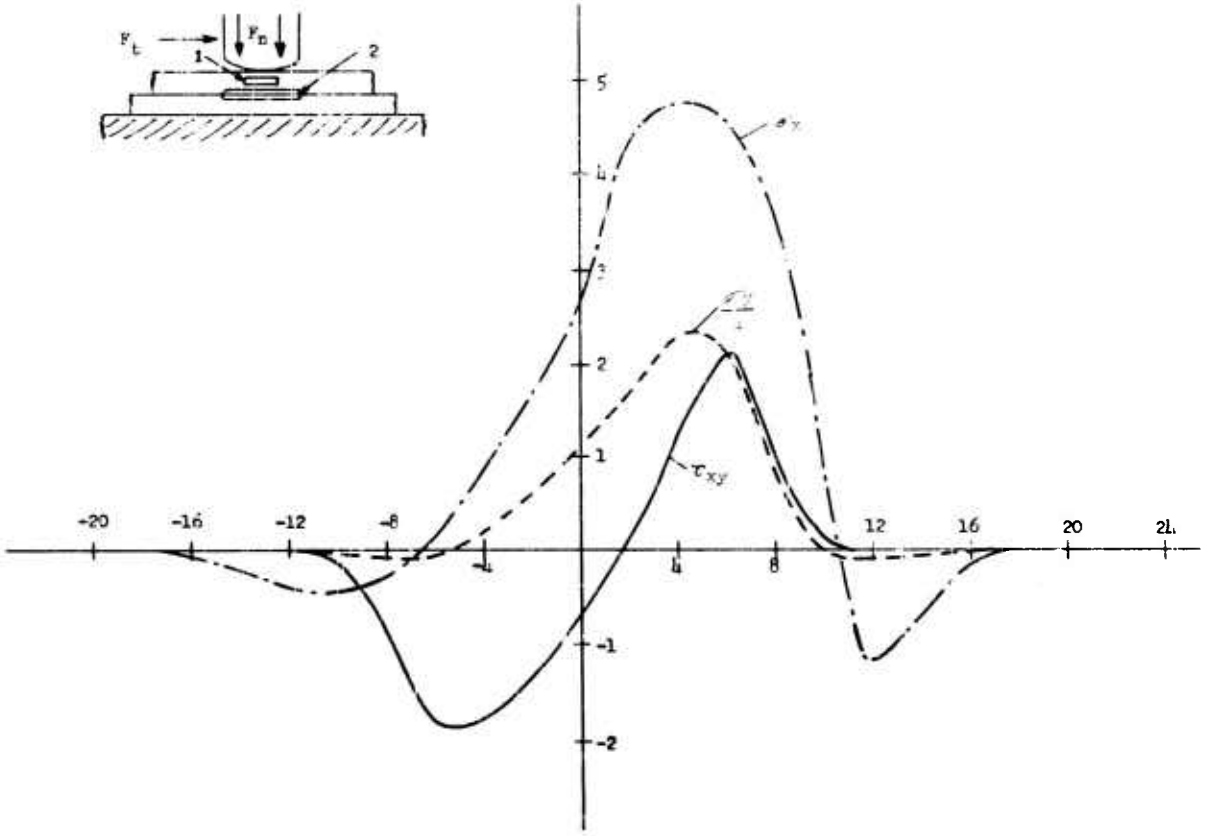


Fig. 3: STRESS DISTRIBUTION JUST BELOW TIP - NORMAL LOAD PLUS TRANSVERSE THRUST AFTER SLIDING

Case III, Tip, of Table I

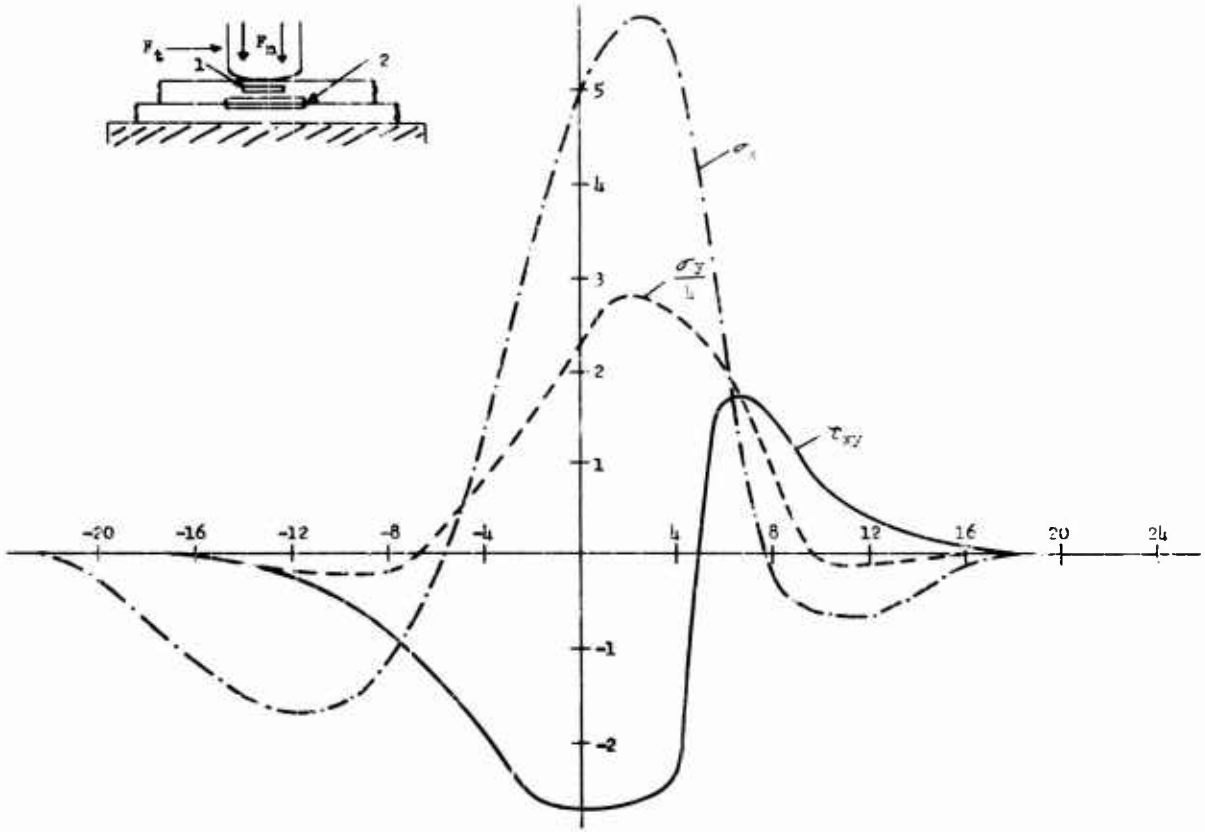


Fig. 4: STRESS DISTRIBUTION IN THE MODEL JUST BELOW THE TIP - TRANSVERSE FORCE REVERSED AFTER SLIP

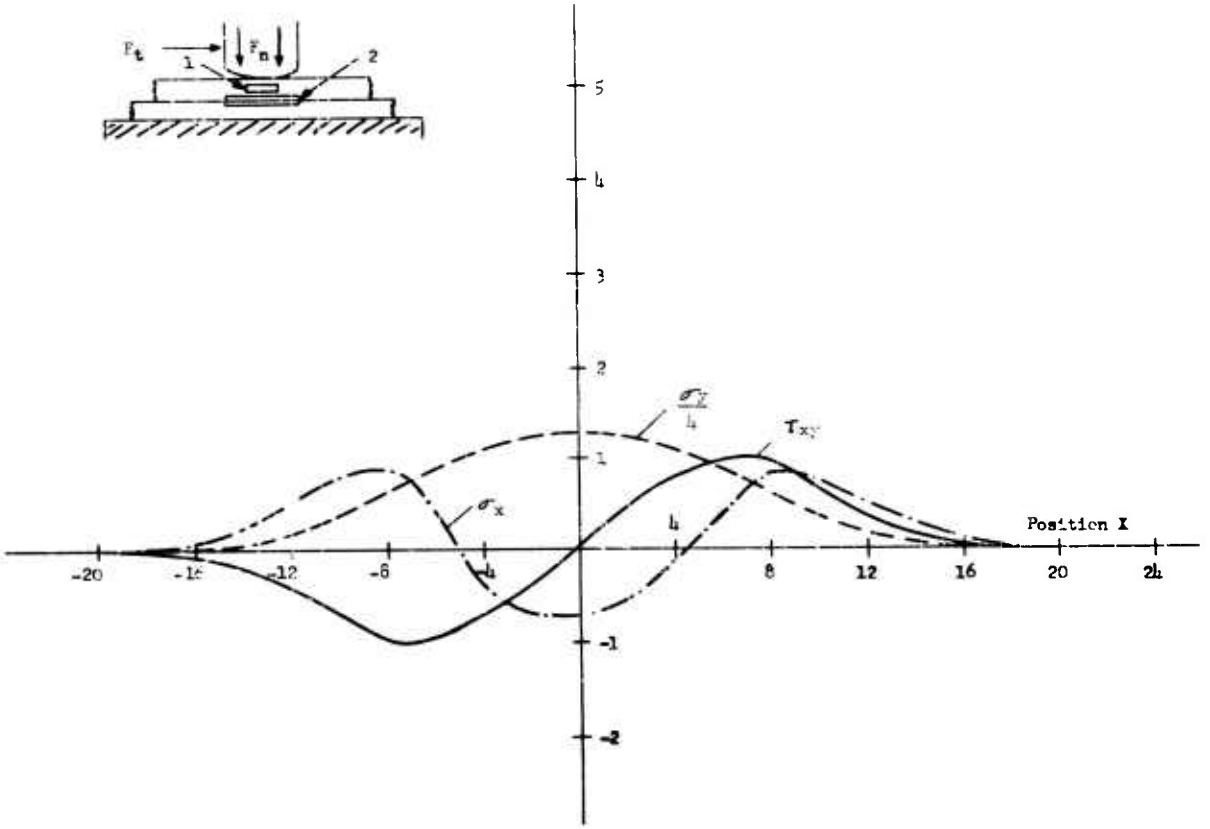


Fig. 5: STRESS DISTRIBUTIONS AT THE MODEL INTERFACE - NORMAL LOAD ONLY

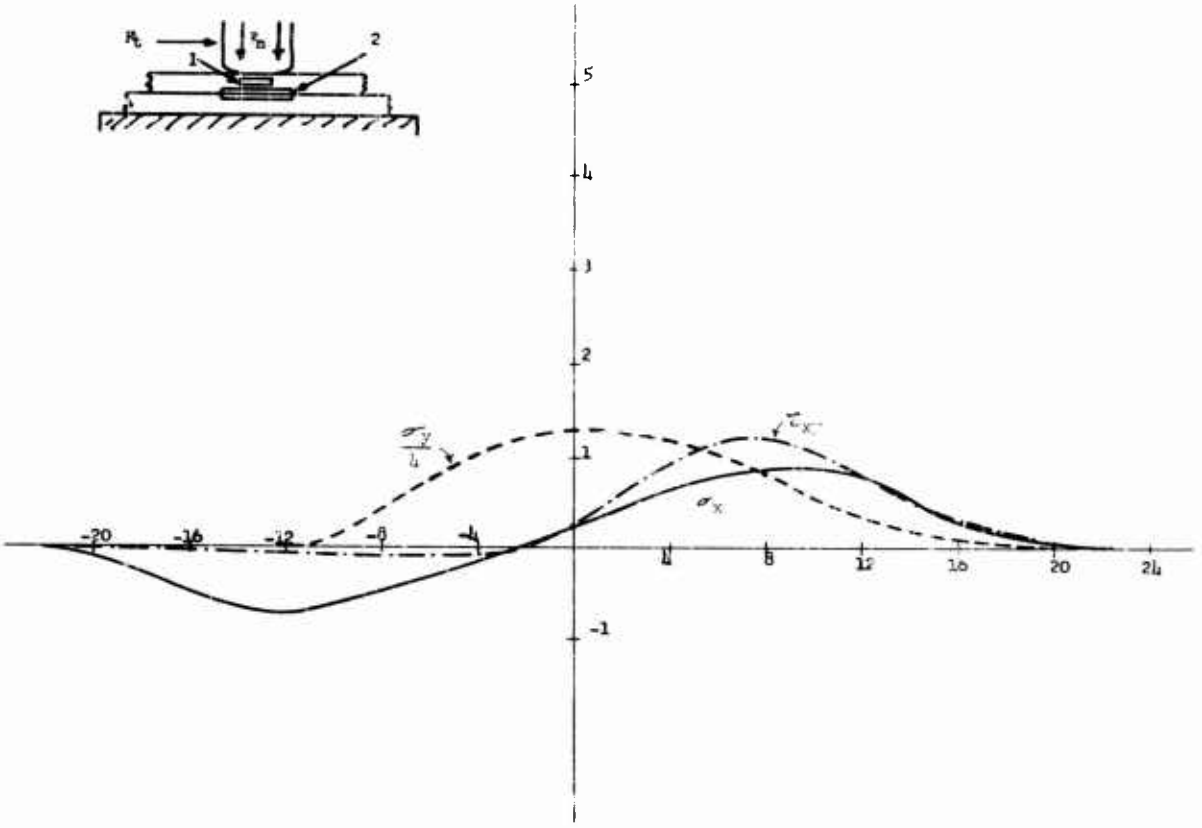


Fig. 6: STRESS DISTRIBUTIONS AT THE MODEL INTERFACE - NORMAL LOAD PLUS TRANSVERSE THRUST, NO SLIDING
Case II, Interface, of Table I

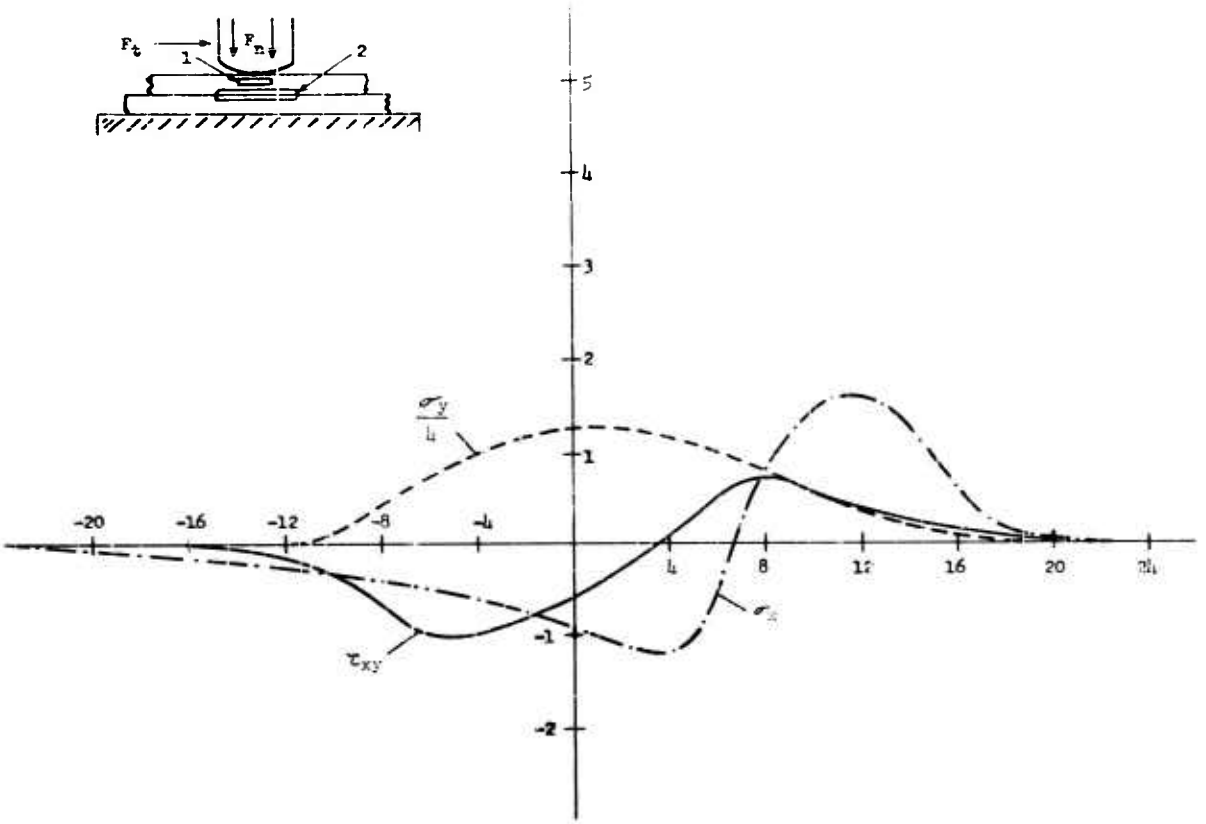


Fig. 7: STRESS DISTRIBUTION AT THE MODEL INTERFACE - NORMAL LOAD PLUS TRANSVERSE THRUST AFTER SLIDING
Case III, Interface, of Table I

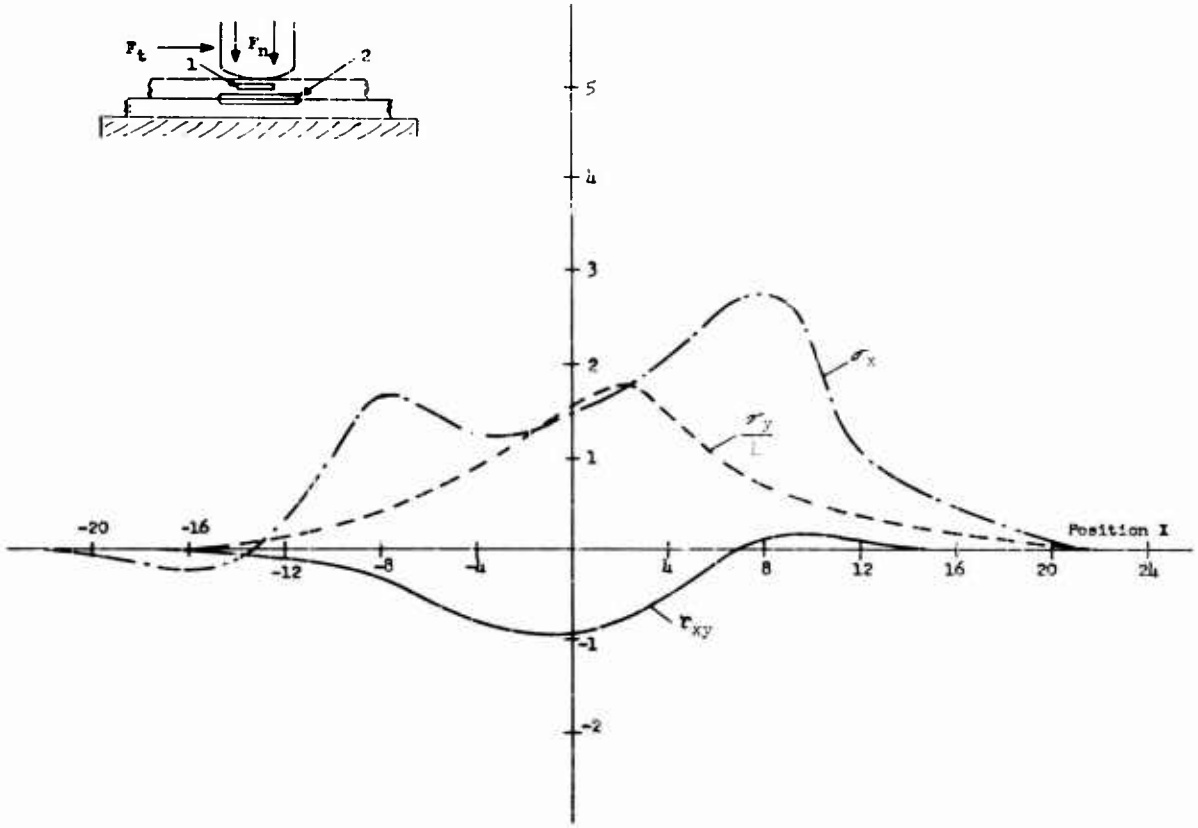


Fig. 8: STRESS DISTRIBUTION AT THE MODEL INTERFACE - TRANSVERSE FORCE REVERSED AFTER SLIDING

Case IV, Interface, Table I

the magnitude of shearing strain across the interface is relatively large. Slip seems to be clearly associated with welding while sliding is a gross movement between the loaded models utilized in the photoelastic stress analysis; however, these models also exhibit slip. Thus, the load in Fig. 6 has been supported largely by relief of stress in the left portion of the figure. No slip can have occurred in the region $-8 < x < +7$, and, from examination of the curve for τ_{xy} it might be inferred that considerable additional shearing stress could be supported. However, experimentally, Fig. 6 represents incipient gross sliding; the analysis by which this imminence is implied is not yet clear.

No attempt was made to reverse transverse thrust before gross sliding occurred. Qualitatively, a reversal of the pattern shown in Fig. 6 would be expected, except that τ_{xy} might be expected to vanish on the right of the axis at a smaller value of transverse load than was previously developed by the original thrust. Whether incipient sliding would occur at a smaller or larger load is not clear and remains to be investigated.

Conditions near the welding tip, as shown in Fig. 2, are pertinent. In this figure slip is first to be expected in the region $+6 < x < +12°$, however, $\tau_{xy}/\sigma_y \approx 0.4$ in this region. Now the values of τ_{xy} and σ_y occur within the material and not at the tip-work interface. Nevertheless, the low value of their ratio is deemed significant. If it is assumed that this low value (0.4) also obtains at the tip-work interface itself, it indicates clearly that slip is to be expected at the weld interface (where the observed ratio is 0.5) rather than at the sonotrode. However, the difference between these ratios is small (20%). Thus, a small variation in model conditions could result in slippage at the sonotrode work-contact zone.

For example, an increase in clamping pressure (normal load) would increase the radius of the sonotrode contact area, without changing appreciably the thickness of the model. If this increase serves to increase the difference between the ratios, a corresponding increase would raise the margin available for successful welding, and a decrease would lower it. Possibly an optimum clamping force, depending on specimen thickness, produces maximum tendency to slip at the weld interface. The weldability tests have already revealed an optimum clamping force for delivery of acoustic power (but practice does not indicate clamping force to be especially critical).

It remains to be seen whether or not the welder design can be adjusted to make these optima occur simultaneously. Thus, the observed difference in the ratios τ_{xy}/σ_y is small enough to suggest that it might be improved (or made worse) by varying the shape of the spherical tip. Some variation in tip efficacy has been observed in connection with continued use of the tip, as well as in connection with solid-state

"wetting" of the tip with the material of the weldment. It may be possible to vary the shape or the radius of the model tip with a view to discovering whether or not this variation can produce a more versatile sonotrode.

Figures 3 and 7 show the stress distributions after sliding has occurred and has been interrupted by a limit stop of the strain panels. Thus, the transverse thrust is supported chiefly by the stop and is nearly zero, as may be seen by cursory examination of the respective curves for τ_{xy}. It is reasonably clear that these curves do not represent the stress pattern while sliding was in process. They do suggest that impact with the limit stop has resulted in a partial reversal of the transverse thrust, and that they, therefore, represent conditions at the beginning of a thrust reversal. Since the arrest of motion was, however, rather violent, we might suppose that the impact resulted in a more or less complete relief of interfacial shearing stress, in which case we would anticipate a repetition of the curves of Fig. 1 and 5. This, however, is not what is found, and the assumption will be made that Fig. 3 and 7 represent a typical termination of sliding. In this case, Fig. 4 and 8 represent the beginning of a new sliding cycle.

From curves for τ_{xy} and for $\sigma_y/4$ of Fig. 8 it seems that a considerable increase in transverse load would be required to produce either slip or sliding since $\tau_{xy}/\sigma_y < 0.3$ at all points. This implication was confirmed by direct test; it was found that a model force of about 65 lb was required to cause sliding instead of the 52 lb that had caused the previous motion.

On the other hand, the curves showing stress near the welding tip suggest that slip is imminent, or much more nearly so than at the same part of the model in Fig. 2. Qualitatively, then, we infer that after gross sliding has occurred, slip at the tip-work interface is quite likely to follow with the next reversal of transverse thrust.

It is further to be noted in Fig. 8 that the values of σ_x are objectionably large and might be sufficient to cause cracking near the edge of the weldment. Such cracking can be produced by improper welding technique, such as excessive duration for the weld cycle at low power and/or a markedly improper clamping force. Whether or not sliding occurs in such cases is not clear; it is believed, however, that sliding is not ordinarily present.

Considered reflection of the foregoing, supplemented by other information available about ultrasonic welding phenomena, leads to the following hypotheses:

1. Local slip is determined by the local ratio of tangential stress to normal stress.

2. Welds can be successfully and efficiently produced only when slip at the weld interface exceeds sliding at the tip-work interface.

3. The existence of local slip causes local dissipation of energy, which in turn, due to local temperature rise, causes local plasticization of the material.

4. Conditions at the tip-work interface must not permit significant plastic flow or sliding at that point if a weld is to be achieved.

5. After local plasticization has begun, local slip will spread to neighboring regions of the weld interface. When a weld is attempted at marginal ultrasonic power, the welded area may fail to spread in this manner, perhaps giving an unbonded central island.

6. Initiation of the weld, and quite probably completion as well, occurs without gross sliding at the weld interface, but in the presence of local slip.

7. Energy dissipation per unit volume at the weld interface is larger than anywhere else, and results in plasticization (though probably not melting)* of the material.

Hypotheses 2 and 4 require considerable explanation. In the first place, the production of interfacial slip (which we associate with welding) implies a quasi-infinite power delivery per unit volume to elements at or near the slipping portions of the interface. From a molecular point of view, the interfacial atomic layers receive a violent relative displacement and absorb all the power computed in terms of force times relative velocity. From a macroscopic point of view, it might be asserted that power delivered per unit volume is equal to shear rate multiplied by shearing stress. When slip occurs, the process is irreversible; the shearing stress is not zero, and the shear rate is quasi-infinite. Thus, from either point of view, intense local energy dissipation is to be expected. Under certain conditions, other workers (16) have observed emission of light from an active interface, but, unfortunately, these observations were not related to generating ultrasonic monometal welds and were not sufficiently detailed to distinguish precisely when or where the light was first emitted.

It is to be noted that local slip without gross sliding requires minimal displacement of material near the weldment, that photoelastic stress analysis clearly indicates the existence of such slip, and that other considerations suggest that local slip could be expected

---

* Metallographic examination with optical and electron microscopy has consistently failed to reveal melting in monometallic welds.

to produce welding. In particular, local slip could be expected to occur rather close to a previously produced weld and, thus, to permit production of overlapping welds. Again, a weld produced near the center of a large sheet can be explained on the basis of local slip without assuming appreciable motion of material surrounding the weld. Both these points require further elucidation, for microsections of overlapping welds show little evidence of discontinuity near the boundary between the welds. If the new weld is to occur continuously up to this boundary, an extremely small slip must be responsible for welding in this region. As has been pointed out, local interfacial slip implies quasi-infinite interfacial shear, with resultant quasi-infinite local delivery of power per unit volume. But the photoelastic models do not specify the magnitude of the relative displacements that they imply. However, Fig. 6 permits a rough calculation of this.

The actual weld envelope may be somewhat elliptical. The abraded sonotrode contact area on the outside of the specimen is almost always somewhat elliptical with its minor axis in the direction of the applied vibratory forces (Fig. 9).

The foregoing discussion is associated discretely with a plane cross section in the center of the weld zone in the direction of vibration and normal to the plane of the sheets. It is clear that the stress system will be modified in the plane cross sections taken parallel to the weld zone but near the weld edges where the interfacial shearing stress induced by the normal force will be oriented 90° away from the direction of the interfacial shearing stress produced by the vibratory energy. The effects, however, should be and, apparently, are approximately the same.

Figures 1 through 4 refer to conditions immediately beneath the tip but not precisely at the tip-work interface. These figures provide a qualitative estimate of the stress distribution at the tip interface, itself; however, caution must be used in the interpretation of quantitative detail. The stress concentration in this region is so intense that photographic resolution is not altogether adequate; furthermore, distortions of the model surfaces and edge effects are particularly troublesome in this region. Integration of the stress equations, from the plane corresponding to these figures to the tip interface, would introduce very little change near the center of the pattern (where the stress trajectories are nearly straight), but would introduce considerable modification near the edges of the contact area.

Figures 5 through 8 refer to stress conditions at the weld interface at various phases of the model stress cycle. No curve has been obtained for stress distribution during the actual sliding process, which, in the models, lasted less than 0.01 sec. However, the various curves in Fig. 6 and 8 contain much relevant information since these figures correspond to conditions just before sliding occurs. In Fig. 6, the data were

obtained by continuous application of a transverse load in addition to the normal load that yielded the data plotted in Fig. 5. Figure 8 represents the result of a reverse transverse thrust applied after sliding had occurred and had been interrupted. The qualitative similarity, with due allowance for the reversal of thrust between Fig. 6 and 8, is obvious. It is clear, however, that the position of maximum shearing stress is much nearer the axis of symmetry in Fig. 8 than in Fig. 6.

These results do, in fact, contribute to a phenomenological theory of vibratory welding. In particular, imposition of the transverse load induces several significant changes in the shear stress distribution at the "weld" interface.

1. It shifts the point of maximum interfacial stress still further away from the axis of symmetry and in the direction along which the lateral load is applied.

2. It increases the maximum interfacial shear stress by 0.2 fringes in the locale toward which the lateral force acts.

3. It almost completely relieves the interfacial shearing stress in that locale of the "weld" interface opposite the direction of the lateral force.

From this it may be tentatively concluded that slip, presumably very local slip, and definitely not general sliding, may well occur first in a small locale on one side of the developing weld zone and then on the other side, and not in the center of the weld zone. This may also be an explanation for the fact that welds are readily formed in close proximity to, and even overlapping, other ultrasonic welds. If vibratory welding depended upon any gross displacement or general sliding of the abutting surfaces, this would not be possible. A highly local area of slip seems to provide a reasonable explanation.

This concept of alternating and spaced areas of local interfacial slip is interesting, because it apparently explains the characteristic physical (5) and metallographic (4) asymmetry which has been observed in vibratory welds.

When ultrasonic welds are produced between ordinary thicknesses of sheet metal, the welded area is observed to include a less completely bonded central island (Fig. 9).



Fig. 9: ULTRASONIC WELD PRODUCED BETWEEN TWO STRIPS OF 2014-T6 ALUMINUM SHEET

(Showing clearly the less completely bonded central island)

It is clear that Fig. 5 through 8 contain data for estimating the imminence of slip, but that a quantitative assertion can be made only when the ratio of supportable tangential stress to normal stress across the interface is known. Ordinary estimates of the coefficient of static friction, essential to the model analysis but not especially significant between weld pieces for reasons previously explained, are not sufficient for this purpose, for these are ordinarily expressed in terms of force ratio instead of stress ratio, a procedure that has led to much confusion and ambiguity. Accordingly, experiments were undertaken to determine the relevant ratio, designated "stress coefficient of static friction", as a function of normal stress. The procedure used is described in Appendix B; the results are plotted in Fig. 10. A detailed consideration of these data and of their application to photoelastic stress analysis follows.

C. Interpretation of Results

Section B describes the experimental results obtained with photoelastic study of a model subjected to static loading analogous to the dynamic loading in an actual weldment at several discrete times during a vibratory cycle. The quantitative data finally presented in Fig. 1 through 8 were obtained on thin plank specimens, in which the stresses had been shown to be qualitatively similar to those existing near the plane of symmetry in a triaxially restrained model. These data

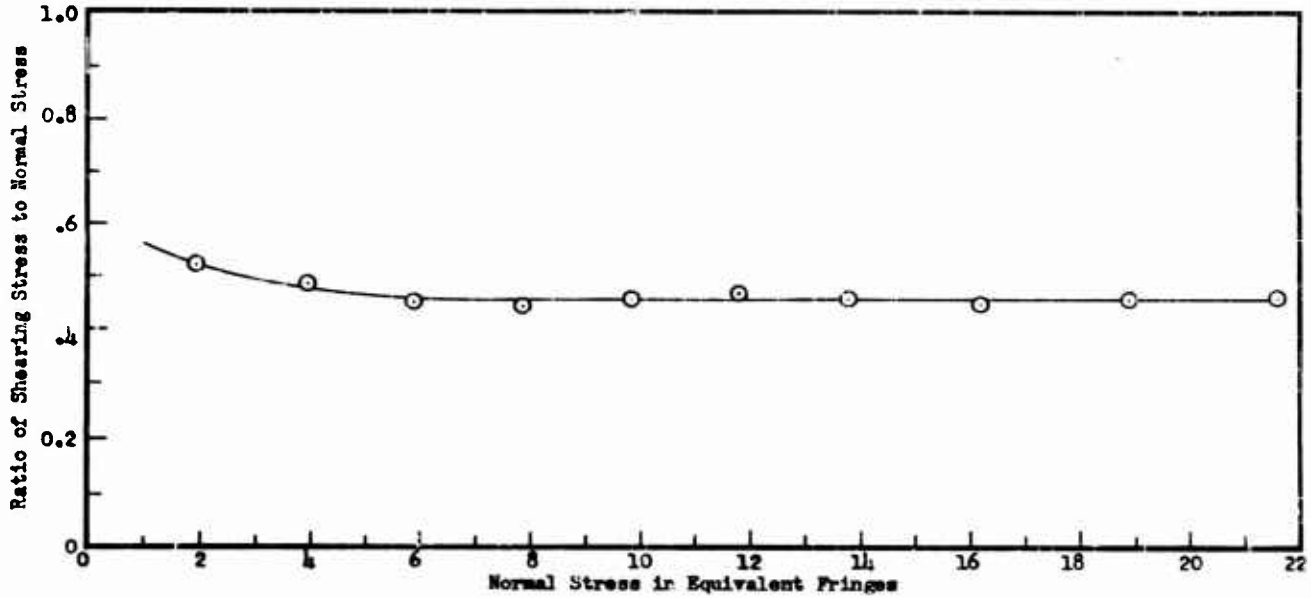


Fig. 10: RATIO OF SHEARING STRESS TO NORMAL STRESS AS A FUNCTION OF NORMAL STRESS FOR VARIOUS NORMAL LOADS

suffice to establish rather clearly the broad outlines of a detailed mechanistic theory of the ultrasonic welding phenomena existent between two sheets of material. Because, in particular, they suggest that the difference between the stress distribution that produces a weld and one that does not is rather small, weldability might be expected to depend critically on such operating variables as clamping force, tip radius, and available power. However, these variables are not particularly critical, so that an attempt must be made to explain why the permissible range of operating conditions is as large as it is.

A careful appraisal of the stress distributions delineated in Section B yields a great deal of information about details of the welding phenomena. An attempt is made in what follows, to isolate the more significant features and, where appropriate, to raise questions requiring further investigation.

The initial application of a normal load or clamping force creates at the weld interface the stress distribution shown in Fig. 5 in which the relationship between the curve for $\sigma_y/4$ and the curve for τ_{xy} is of primary significance. Thus, it will be observed that in the region $+8 < x < +20$, $\tau_{xy}/\sigma_y \approx 0.5$. Examination of Fig. 9 reveals that the stress coefficient of static friction for this material limits (τ_{xy}/σ_y) to the magnitude actually observed, and it hardly seems reasonable to suppose that this observed ratio has in fact occurred by chance. Hence, we can infer that local slip has already occurred in this region.

If we were to suppose that no slipping had occurred along the weld interface, we would expect approximately the stress distribution found in a solid block subjected to the same load for which, of course, a theoretical solution is available (40). However, in our case, no tension can exist across the weld interface for large values of X (Fig. 5), and such tensions are, of course, to be expected in the case of a solid block. Accordingly, it is not safe to assert that slippage or the lack thereof is the only difference between the case analyzed and that of the solid block. Nevertheless, it would be interesting to discover whether or not the ratio of τ_{xy} to σ_y in this case is markedly different from the corresponding ratio in the case for which a theoretical solution is available. An investigation of this point, either theoretically or experimentally, is clearly indicated for future work.

In any event, whether or not slip has already occurred in Fig. 5, it is clearly imminent. The effect of an added transverse thrust is shown in Fig. 6. The marked difference between these two figures definitely implies local slip. In Fig. 5 the curve for σ_x shows a region of tensile stress near the center. This region of tensile stress has migrated well to the left of center in Fig. 6, a change that would not be possible without slip in the critical region revealed in Fig. 5. Again, in Fig. 6, $\tau_{xy}/\sigma_y \approx 0.5$ in the region $+8 < x < +20$, from which it again can be inferred that slip must have occurred.

To the left of center in Fig. 6, τ_{xy} has almost vanished. The indicated negative values beyond $x = -12$ can be due only to experimental error. But, in any case, there is nothing in this region to suggest that local slip (to the right) has occurred, for this would be possible only if τ_{xy} were positive.

A small increase in transverse load beyond that required to produce Fig. 6 resulted in gross sliding of the whole specimen. It is of interest to inquire what evidence of incipient sliding can be discovered in this figure. Clearly, the laws of statics require the area beneath the curve for τ_{xy} to be always equal to the transverse thrust. The portion of this curve to the right of $x = +8$ is virtually the same as it is in Fig. 5, which is to be expected, since the curve for σ_y is substantially the same in both figures, and since the curve for σ_y sets an upper limit for the curve for τ_{xy}.

If it is assumed that in Fig. 6, there is no interfacial slip at $x = -12$, and that mean tensile stress σ_x of 1.0 fringe (72-psi strain $12 \cdot 10^{-5}$) is integrated from $x = -12$ to $x = +20$ (1.6 in. in the photoelastic model), there should be a maximum interfacial slip of $2 \cdot 10^{-4}$ in. in the model, or of $2 \cdot 10^{-5}$ in. in the weldment represented by the model. With allowance for the ratio between the moduli of aluminum and Catalin, the slip in the weldment would be further reduced by a factor of 1/16 to something less than 10^{-6} in. or of the order of 100 atomic diameters. Indeed, this figure represents something of an upper limit; for harder or thinner specimens, it would be even smaller.

Interfacial displacements of this magnitude, which would be expected in the early phases of the weld cycle, could scarcely be expected to produce melting on an observable scale, and none has been observed in monometallic welds. Instead, they suggest that the bonding is essentially interfacial in character, that, except for heat plus rapid small displacement effects not essential to the basic mechanism, little disruption of crystal structure need be expected, and that a spreading of the region of interfacial slip could be expected without appreciable distortion of previously affected regions. Plasticization and subsequent plastic flow would, on this hypothesis, occur rather late in the weld cycle.

It is of interest to investigate the extent to which a surface dissipation of energy might be expected to affect that surface. It might be expected that most of the energy serves to dissipate or pulverize surface films and, thus, to enhance true nascent surface contact on the atomic scale. To give a sense of the orders of magnitude involved, a useful parameter is the energy of melting per atom. For aluminum ($mp = 660°C$, specific heat = 0.25 cal/g, latent heat = 80 cal/g, atomic weight = 27), this figure is roughly $4 \cdot 10^{-13}$ ergs/atom. The mean volume available per atom of aluminum is $1.7 \cdot 10^{-23}$ cm^3, so that a

surface layer of 1 cm^2 will contain about $1.5 \cdot 10^{15}$ atoms. A surface stress of 200 psi or $1.4 \cdot 10^7$ dyne/cm^2 times a displacement of $2 \cdot 10^{-6}$ cm would result in a surface dissipation of 30 ergs cm^2, which, shared between two surfaces, would be about 10^{-14} ergs/atom. Thus, interfacial relative displacements of the magnitude suggested by the photoelastic analysis will produce significant disturbances at the atomic level but could scarcely produce melting on any observable scale.

It is further to be noted that energy dissipation produced in this way could be self limiting. Heating effects would result in local plasticization, and interfacial slip would be replaced by volume shear, which would still be large enough to be irreversible. However, once plasticization is achieved, it will be maintained for the duration of the weld cycle.

These assumptions lead to the fourth hypothesis listed. If plasticization occurs first at the tip, it should not be possible to develop interfacial slip elsewhere. If this interpretation of the photoelastic analysis is correct, certain assertions about weldability can be made.

Interfacial displacement for a given transverse thrust is inversely proportional to modulus. Weldability should decrease with increasing modulus so that materials in this category should require higher power.

The geometrical parameters associated with welding are three: tip radius, radius of contact area, and sheet thickness. Given the first and third of these, the force (F) required to maintain the second will be roughly inversely proportional to $(1/E_1 + 1/E_2)$ where E_1 and E_2 are moduli of tip and specimen, respectively. Thus, high-modulus materials might require greater clamping pressures; however, the relationship is not one of linear proportionality.

On the basis of this discussion, a number of points invite further investigation. The photoelastic analysis for Fig. 2 and 6 should be repeated at greater and smaller normal loads to discover whether the margin of available transverse thrust beneath the welding tip does or does not depend on clamping force. In making these analyses, the transverse thrust should be cyclically applied before the photographs are taken.

Local slip without sliding should be detectable without photoelastic analysis. An appropriately designed yoke on the plastic models should serve to detect and to measure this, not only on thin models but also in triaxially restrained models. A series of experiments with such a device should serve to define magnitude of slip producible without sliding as a function of specimen thickness. Such experiments should

serve to establish whether any limitation on weldability exists and whether it is associated with the stress system produced by the clamping force as thickness is increased.

Behavior of the photoelastic models falls nicely into the concept of stress coefficient of static friction, which turns out to be larger than the ordinary coefficient of friction. Experiments to discover whether or not this concept is applicable to metals are clearly indicated, especially since the data of Fig. 10 are so startingly consistent by comparison with the results of typical measurements of metallic friction.

The ultimate objective of the investigation is quite clear: given a material of a specified thickness and of known properties to discover the ranges of tip radius and of clamping force within which welding is possible and the optimum values of each. It is to be noted that this optimum is based entirely on criteria independent of power requirements and specifies only how the sonotrodes should be designed and loaded for maximum efficiency. This specification immediately implies a definite acoustic impedance presented by the weldment to the sonotrode, which must be discovered by independent investigation. Design of the acoustic coupling system for an effective impedance match will then be feasible, and establishing a range of power requirements for welding will be the last step in the investigation.

III. ENERGY DELIVERED TO THE WELD ZONE

The energy required to make a weld must be considered in developing any theory for vibratory welding. As an introduction to more detailed considerations, the flow of energy through the entire electro-acoustic system will be described first.

Electrical power at 60 cycles and standard-line voltage (110, 220, 440 volts) is delivered into the "ultrasonic generator" or power source, where it is converted by means of auxiliary electrical equipment, such as rotary alternators or electronic oscillators and power amplifiers, into electrical power at the frequency of operation of the welding machine, which is ordinarily in the range of 5000 to 75,000 cps. The output transformer of the electronic source is provided with suitable taps to permit making an electrical impedance match to either a magnetostrictive transducer or an electrostrictive ceramic transducer. The impedance is satisfactorily matched when the output impedance of the power source is approximately equal to the input impedance associated with the loaded transducer. For magnetostrictive transducers of the type used in the present program, this value is in the range of 16 to 32 ohms. For electrostrictive ceramic transducers, the impedance is determined by geometry and material and may be in the range of 50 to several hundred ohms. The first three blocks of Fig. 11 depict this portion of an ultrasonic welding system.

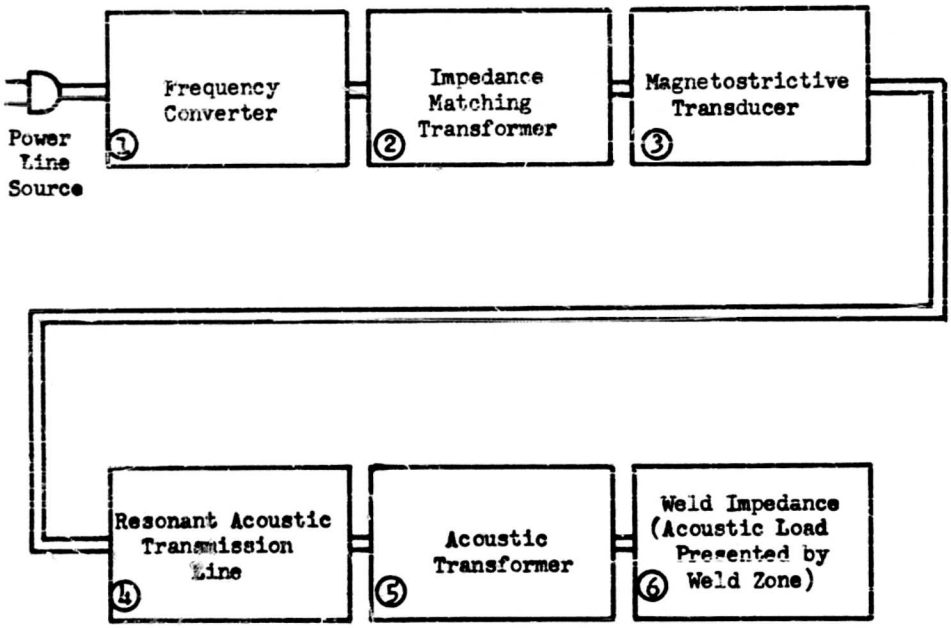


Fig. 11: BLOCK DIAGRAM OF ULTRASONIC WELDING SYSTEM

Electrical power at the proper frequency is thus delivered to the transducer where it is converted into elastic vibration either by the magnetostrictive effect transducer material (22) is nickel, nickel-cobalt, Permendur, Permalloy, or by the electrostrictive or piezoelectric effect if the transducer (32) is barium titanate, lead zirconate, quartz, tourmaline, etc. Usually the conversion efficiency is of the order of 28-38% for the magnetostrictive transducers and 40-80% for the electrostrictive materials. Ceramic transducers are fragile and difficult to install in coupling systems on a practical basis, especially for high-powered operation. The ruggedness and durability of magnetostrictive transducers seems to make them more practical, at the present time, for welding operations despite their somewhat lower efficiency.

The vibratory power output of the transducer should be conducted with maximum efficiency to the weld zone. The need for an electrical impedance match between the power source and the transducer has been discussed and is depicted by Blocks 2 and 3 of Fig. 11. Analogous acoustic impedance matching must be obtained between the transducer and the weld zone, except that instead of an impedance adjustment for obtaining a given complex ratio of voltage to amperage ($Z_e = E/I$), in the electrical case, the acoustic impedance is ($Z_a = F/V$); that is, the complex ratio of transmitted force to displacement velocity at the points of coupling must be matched by suitable selection of coupling materials and their cross-sectional areas. The acoustical analogy of the electrical transformer exists, for example, in suitable geometrically tapered coupling members. To accomplish welding under truly optimum conditions, the acoustical properties of the materials being welded should be considered, just as in resistance welding the conductivity of the materials being welded influences the design of resistance welding machines.

Block 4 of Fig. 11 represents a (preferably) resonant (integral number of one-half wavelengths) acoustic transmission line normally used to connect the transducer to the acoustic transformer. Block 5 represents a tapered (preferably) resonant section to increase the vibratory amplitude to the desired level. In practice, 4 and 5 may be the same member. Block 6 represents the weld zone of unknown acoustic impedance, whose value for various materials and gages is of interest in producing a more efficient welding machine.

In this section of the report, consideration is given to the factors which strongly influence the delivery of elastic vibratory power into a weld locale with maximum efficiency, that is, the efficient accomplishment of welds with minimum power input.

The problem is by no means as straightforward as simply doubling or tripling the efficiency of the transducer. Modest improvements in coupling design and suitable understanding of the factors controlling power transmission between the transducer and the weld locale can increase

welder performance at fixed power input several fold. For example, an incorrectly designed acoustical transformer may have a "limiting" amplification factor of about 4.5, whereas a properly designed acoustical transformer may increase amplitude by as much as 20 or 30 times when required. Such factors are brought into focus here to provide a basis for designing ultrasonic welding equipment of improved capabilities and to extend the usefulness of this new metal-joining process.

It is also necessary to consider the dissipation of vibratory energy after it reaches the weld zone. Part of this energy is transmitted through and beyond the weld zone and is dissipated elsewhere. Some of it is locked into the metals being joined as surface and internal stresses. A portion of the energy produces elastic and plastic deformation in the weld zone, generating heat and resulting in an associated temperature rise.

In the experimental results reported first, the minimum net acoustic energy needed to make a weld is correlated with the optimum power-clamping force for several thicknesses of each material (4). The minimum energy was determined by arbitrarily selecting a single clamping force and a fixed weld-time interval on the basis of previous experience, and producing welds with progressively decreasing power until the bond obtained no longer failed in peel by nugget tearout. The procedure was then repeated at a series of selected values of clamping force, but at the same fixed weld time, until sufficient data were obtained to plot a curve of clamping force against minimum power. This plot, therefore, exhibits the threshold power necessary for welding as defined by the nugget-pullout peel test (Fig. 12).

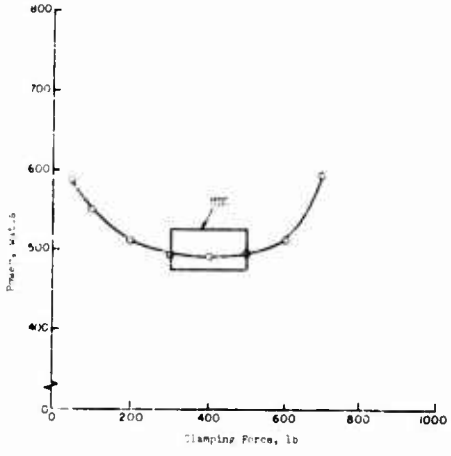


Fig. 12: THRESHOLD CURVE FOR WELDING 0.020-INCH 1100-H18 ALUMINUM ALLOY

Preliminary data were obtained at a weld time of 1 sec. The same procedure was reproduced for several material thicknesses with a time of 0.5 sec. It was noted in the second series that the power required to make a weld was about twice as high as in the first, indicating that, under the general conditions of the experiment, weld time can be reduced within limits if power is proportionately increased. It was, therefore, concluded that for the purpose of exploratory work, a weld time of 1 sec gives representative results.

All curves obtained in this manner have a characteristic shape for what appears to be maximum welding efficiency. Photoelastic investigations as well as a priori considerations suggest that the minimum-power or maximum-efficiency condition (MEC) quite probably involves the accomplishment of an impedance match between the welding tip and the workpiece, but this conclusion requires additional confirmation.

The optimum power-clamping force condition, which was established on the basis of the easily determinable electrical power to the transducer, was used to obtain data on the net acoustical energy delivered to the weld zone, by the standing-wave-ratio (SWR) technique developed under Phase I of the program. The significance of the threshold curve, however, was not completely clear, so carefully designed, comprehensive experiments were carried out to determine the relationship of this curve to the various weld characteristics.

A. Electrical Power to Transducer

The electrical power delivered from the power source to the transducer is routinely measured in welding operations, using a VAW meter.* The instrument used for these investigations was periodically calibrated and had a good frequency response to about 300 kc and an over-all time constant (including meter lag) of 1 sec, with over-all specification accuracy of ± 3%.

During the early stages of this work, the VAW measurements were checked by a technique involving the insertion of an accurate, low-value, non-reactive resistor in series with the transducer. With the aid of a dual trace oscilloscope, the voltage wave form at the input to the transducer and the current wave form obtained from the small resistor were simultaneously recorded. The electrical power values were then obtained by integration of the in-phase portions of these current and voltage forms. The accuracy of this system, which depends primarily upon the accuracy with which the resistance value is known and upon the oscillograph calibration, was estimated to be 2% or less in the work reported here. The data obtained by this technique were essentially the same as those obtained from VAW measurements. The simpler VAW method was considered satisfactory and was, therefore, used for the balance of the program.

* Model No. 102, John Fluke Mfg. Co.

B. Acoustical Power

As previously noted, only a portion of the electrical power delivered to the transducer reaches the weld zone as acoustic power, because of losses in conversion, transmission, and reflection at impedance discontinuities. Precise determination of the delivered acoustic power is not straightforward. Under Phase I of this program, theoretical and experimental studies indicated the feasibility of measuring the standing-wave ratio (SWR) in the coupler system to obtain data on acoustic power delivery.

The theoretical basis for the SWR technique was presented in Appendix A to the Phase I final report (4) and is further developed in Appendix C of this report. The results of these analyses may be summarized briefly as follows:

1. The power delivered by any ultrasonic power-transmitting member is proportional to the particle displacement and inversely proportional to the elastic standing-wave ratio. The pertinent relationships are given by the following equation:

$$P = \frac{1}{2} \frac{R_c}{S} \omega^2 \xi_{max}^2, \tag{5}$$

or

$$P = \frac{R_c}{2\omega^2} \left(\ddot{\xi}_+^2 - \ddot{\xi}_-^2 \right), \tag{6}$$

where

P = transmitted acoustical power,

R_c = characteristic impedance of the transmitting member,

S = elastic standing-wave ratio,

ξ = particle displacement,

ω = $2\pi f$, radians/sec

f = frequency, cps.

2. Particle displacements or accelerations which are proportional to stresses or strains associated with the actual power delivered can be detected easily with microphone elements.

3. The electrical outputs of these elements when applied after proper amplification to the deflection plates of an oscilloscope, produce an ellipse whose area (A) is proportional to the power being transmitted: Thus,

$$A = \pi \left(\xi_-^2 - \xi_+^2 \right), \tag{7}$$

or

$$A = \frac{\pi}{\omega^4} \left(\ddot{\xi}_-^2 - \ddot{\xi}_+^2 \right). \tag{8}$$

These equations provide the basis for developing instrumentation for acoustic power measurement. A small precision ultrasonic welding array was assembled (4), and the coupler was suitably equipped with two SWR-sensing elements (microphones). The response from these microphones was fed into an oscilloscope, and the elliptical oscilloscope trace was photographed and used for acoustic power determinations.

The individual microphone elements were calibrated against the set of elements used in the early calorimetric studies of Phase I. The latter elements served as primary calibrated standards. Relative calibration was accomplished by comparing the ellipses obtained during welding of identical materials and applying correction factors for signal equivalence at a given power level. The oscilloscope amplifiers were also calibrated, as was the photographic projection ratio. The 1-cm-spaced grid on the oscilloscope graticule was photographed along with the elliptical trace and used as a base for the projection ratio, which was maintained at a 1:1 correspondence between the projected image and the graticule.

The procedure used to determine the net acoustic energy delivered to the weld zone for a given material and material thickness was as follows:

1. With the minimum power condition selected from the threshold curve as previously described, a weld was made, and the microphone signals were portrayed on the oscilloscope.

2. The oscilloscope trace was cinematically photographed during the entire weld interval.

3. The area of the projected ellipse in each frame was integrated manually with a compensating polar planimeter, and appropriate computations were made to reduce this information to acoustic power delivery at any given instant during the weld interval.

4. The calculated values were plotted as a function of time and integrated by means of the planimeter to determine the total energy delivered during the weld interval.

The accuracy of these measurements is not known precisely, as it is dependent on microphone calibration, oscilloscope amplifier calibration, projection enlargement ratio, and planimeter area determinations, all of which involve a certain amount of operator skill. However, repetitive measurements with a given material under a given set of conditions indicate a reproducibility of ± 10% or better.

It is apparent from the preceding discussion that the procedure used in applying the SWR technique to find net acoustic energy is laborious and time-consuming, involving oscilloscope-trace photography, manual integration of ellipse areas, and subsequent integration of the curve of areas vs time. A method was, therefore, sought that would instantaneously give data in useful form.

The analysis presented in Appendix C of the present report indicates the essential components for an instrument that generates voltage signals proportional to the instantaneous acoustic power level in the coupler, and amplifies them for recording on a strip-chart recorder. The necessary equipment was assembled and preliminary measurements made. The acoustic power data obtained in this way compare favorably with that previously obtained from the photographed and integrated oscilloscope ellipse traces. This abbreviated technique not only provides a means for substantially increasing the rate of data output, but it also confirmed the validity of the SWR measuring technique.

During the course of studies to investigate the net energy delivered to the weld zone, consideration was given to the power that passed through and beyond the weld zone. An effort was made to eliminate this loss by using a mirror or dual transducer system. Two opposed identical systems were arranged to make welds between their respective welding tips, thus eliminating the anvil. Mechanical cross-coupling occurred under some operating conditions to such an extent that the power supplied to one transducer was delivered to the other.

C. Significance of Threshold Curves

Throughout the Phase I program, as well as the early part of this Phase II, reliance was placed on the threshold curve, as determined by the nugget-pullout peel test, for defining minimum power conditions for producing a weld in a given material. The results were highly reproducible and have been successfully used in establishing comparative weldability of various materials and correlating welding power requirements with material properties (Section IV). As stated previously, the significance of the threshold curve was not full understood. It appears that this curve probably expresses the power-force relationship for best impedance match into the weld zone, but it might also describe variations in weld quality or size. Accordingly, a comprehensive set of experiments was designed to investigate its significance further.

Weld quality may be described in part by tensile-shear strength, cross-tension strength, weld area, and thickness deformation. Other parameters that can be included in a comprehensive study of welding are temperature at the weld junction during welding and the microstructure in and around the weld zone. To ascertain the significance of the threshold curve, it is necessary to consider such parameters.

The materials selected for this study cover a wide range of physical and mechanical properties. They include 1100 H-18 aluminum 0.009 in. and 0.020-in. thick; Type 302 stainless steel, cold rolled 0.005 in. thick, and annealed 0.010-in. thick; and OFHC* copper in the half-hard condition, 0.020 in. thick.

With a constant sonotrode tip radius of 2 in. and a weld interval of 1 sec, a threshold curve was established for each material and gage. Weld specimens were then produced at operating conditions in the vicinity of the minimum energy locales of these threshold curves and were evaluated in terms of each of the selected parameters. The threshold curves for the various materials are presented in Fig. 12-16. In each case the outlined block embraces the MEC, power-force relationship based on the peel test.

1. Measurement Details

a. Tensile-Shear Strength

Weld specimens were 3/4 in. x 4 in. with the weld centrally located in a 3/4-in. overlap. These specimens were sheared with a model "D" Young Testing Machine, with the hydraulic line modified by the insertion of a Heise** gage to determine more precisely the resulting shear values.

b. Cross-Tension Strengths

Individual tabs (5/8 in. x 3 in.) were placed in a jig, which assured proper alignment and spot placement. The welded specimens were then tested in a special cross-tension testing fixture which was designed to fit into the Young machine so that the applied load would be essentially tension on the weld. The ultimate loads at failure were again read on the Heise gage.

---

* Oxygen-free high-conductivity copper.

** The pressure could be read to ±0.1 psig with the gage having an accuracy over the entire working range of ±0.2 psig.

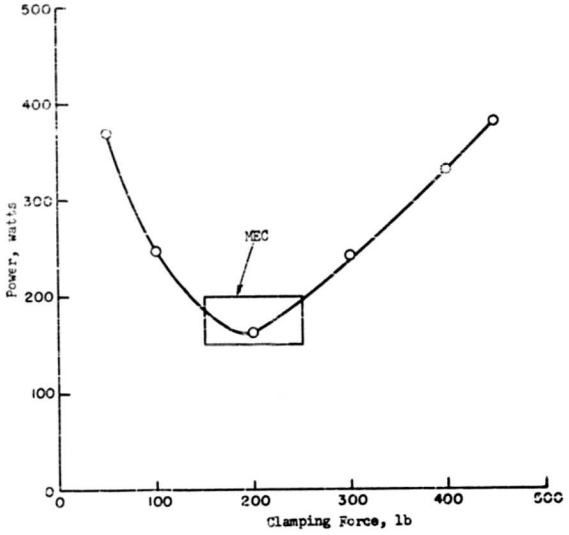


Fig. 13: THRESHOLD CURVE FOR WELDING 0.009-INCH 1100-H18 ALUMINUM ALLOY

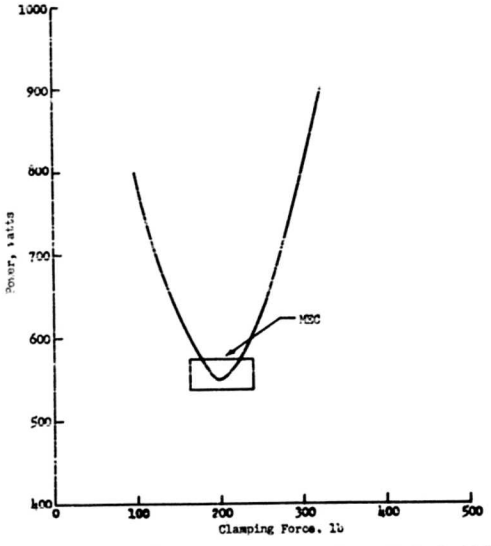


Fig. 14: THRESHOLD CURVE FOR WELDING 0.005-INCH COLD-ROLLED STAINLESS STEEL

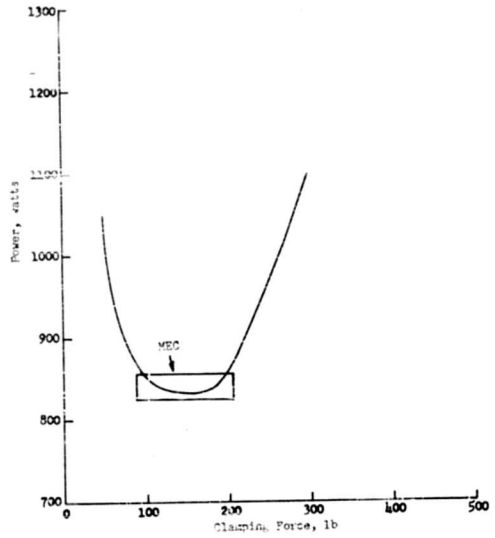


Fig. 15: THRESHOLD CURVE FOR WELDING 0.010-INCH ANNEALED 302 STAINLESS STEEL

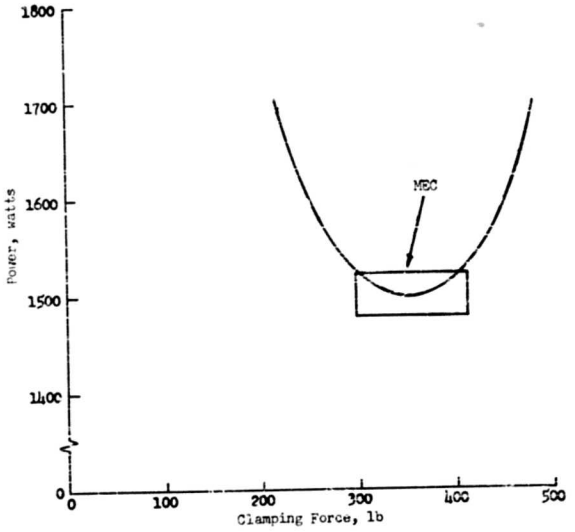


Fig. 16: THRESHOLD CURVE FOR WELDING 0.020-INCH HALF-HARD COPPER

c. Weld Area

Weld area measurements were obtained by peeling the weld whenever possible; when peeling proved impossible, all metal was trimmed from the torn out nugget. In either case, an optical image of the area was projected onto a ground glass screen so that a planimeter could be used to measure the areas.

d. Deformation

Deformation data were obtained by measuring (as indicated in Fig. 17) the thickness of the fabricated specimen by traversing it with a ball micrometer in the weld region along central lines first in the direction of vibratory motion and again at right angles to this motion.

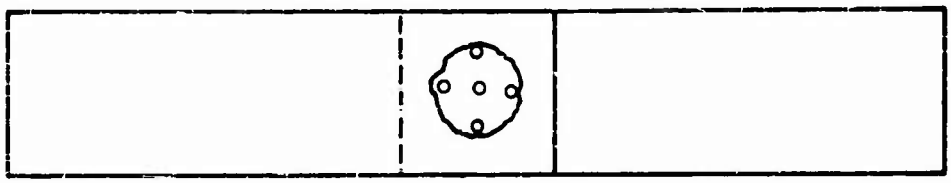


Fig. 17: METHOD FOR MEASURING DEFORMATION DATA

e. Temperature

The temperature in the weld zone was obtained at each of the operating conditions in accordance with techniques developed under Phase I. Temperature data were obtained at only six points for the copper because of time limitations. No temperature data were obtained for the stainless steel because of the difficulty of getting consistently good temperature records with the very thin material.

2. Description and Discussion of Data

The data plotted in terms of the significant variables produced the surface or contour plots of Fig. 18-38. In each case the MEC, taken from the pertinent threshold curve of Fig. 12-16, is solidly outlined to permit evaluation of its significance in the over-all pattern.

Figures 18-22 are surface plots showing the tensile shear strength associated with the various levels of power and clamping force. It is apparent in all cases that the highest tensile-shear strength occurs at somewhat higher power and clamping force than are indicated by the MEC. Figure 19 for the 0.005-in. stainless steel shows a complete foldover in the surface plot. Metallographic examination of specimens obtained in the power range of this foldover indicated that excess power was used even at these reasonably short welding times, resulting in a damaged weld due to either cracking or surface damage. Thus, the best shear strength was obtained at a power level only slightly greater than the MEC. Figure 21 for the 0.010-in. stainless steel, shows that the tensile-shear strength falls rapidly as the clamping force is increased somewhat beyond the range of the MEC (about 350 lb). The falloff was tentatively ascribed to a large increase in area, with corresponding reduction in available power per unit weld area (as in the weld area surface plot in Fig. 29). Figures 18, 19, and 22 for aluminum and copper show a similar reduction in strength at clamping forces outside the established threshold curve and compare with the area plots in Fig. 28 and 31.

Figures 23-27 present data for the cross-tension strength of the various materials as a function of power and clamping force. Again it is apparent that maximum strength is developed at somewhat higher powers than those of the MEC, but not necessarily at higher clamping forces. These curves do not show the marked decrease in strength with increased clamping force that was characteristic of the tensile-shear curves. Figures 28-31 show the effect of power and clamping force on weld area. For aluminum, annealed stainless steel, and copper, the weld area becomes larger with the increase in power and clamping force. The Hertz relationship (28) shows that the contact area between a spherical indentor and a semi-infinite plate (i.e. a plate bounded by only one plane) varies as $F^{2/3}$ power, where F = force. Neglecting the influence of the hard anvil behind the weldment, it could be expected that the resulting area would be further enlarged by the action of the vibrating sonotrode. These data indicate that the increasing area partially accounts for the higher values of tensile-shear and cross-tension strengths associated with higher power and clamping force. This appears true when these powers and clamping forces do not greatly exceed the MEC values.

The deformation data are plotted in Fig. 32-35. Deformation generally increases with increased clamping force except at the low-power levels; increasing power increases deformation except at the highest clamping forces. Deformation is limited in the region of low-power and high clamping force.

Consideration of the graphical data indicate that tensile-shear strength, cross-tension strength, weld area, and thickness deformation are related to the MEC in only a general way; that is, the maximum for each of these occurs at powers and clamping forces somewhat greater than those of the MEC. However, metallographic examination of specimens produced at conditions surrounding the threshold curve indicates that the data provided by this curve are generally valid for producing good welds.

Low-quality welds (having surface damage, cracks, poor bonds, etc) were obtained in regions far removed from the threshold curve. High clamping forces and low power resulted in poor bonds; low clamping force usually resulted in cracks in and around the weld zone. On the basis of the data presented, there appears to be no close correlation between the MEC and the weld quality parameters of tensile-shear and cross-tension strength, weld area, and deformation.

The temperature surface plots of Fig. 36-38 present more significant results. In each case, maximum temperature at any fixed power level occurs at a clamping force which approximates the clamping force associated with the MEC. It is significant that temperature seems to be the only major variable that can be associated with this condition. It was noted at the beginning of this section that the most significant part of the energy delivered to the weld zone creates elastic and plastic deformation and is apparent as a temperature rise. The temperature achieved in the weld zone must, therefore, be related to the energy delivered, since the clamping force affects the coupling of the transducer-coupler system and sonotrode tip to the weldment and thus, has a substantial influence on the impedance match between the coupler and the materials to be welded. It is concluded that the threshold curve, particularly the MEC, is related to the efficiency of the energy delivery into the weld and is not critically related to the mechanical properties of the resulting weld.

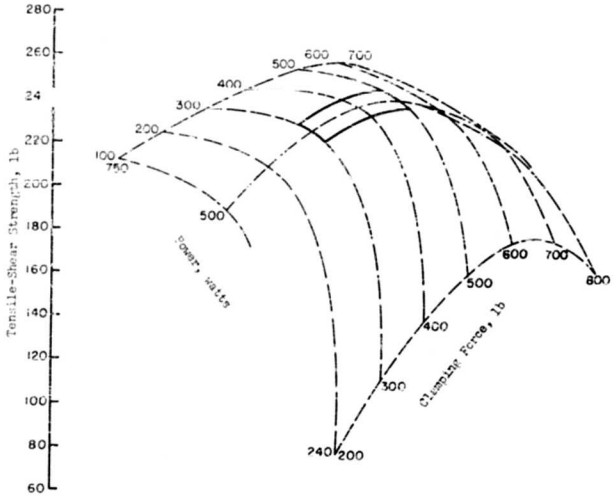


Fig. 18: EFFECT OF CLAMPING FORCE AND POWER ON TENSILE-SHEAR STRENGTH OF A WELD IN 0.020-INCH 1100-H18 ALUMINUM ALLOY

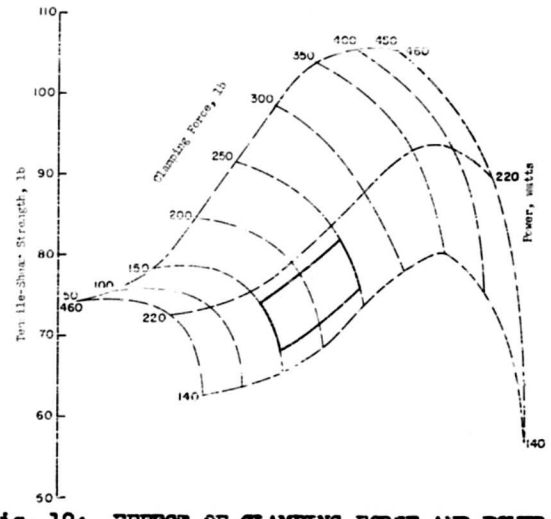


Fig. 19: EFFECT OF CLAMPING FORCE AND POWER ON TENSILE-SHEAR STRENGTH OF A WELD IN 0.009-INCH 1100-H18 ALUMINUM ALLOY

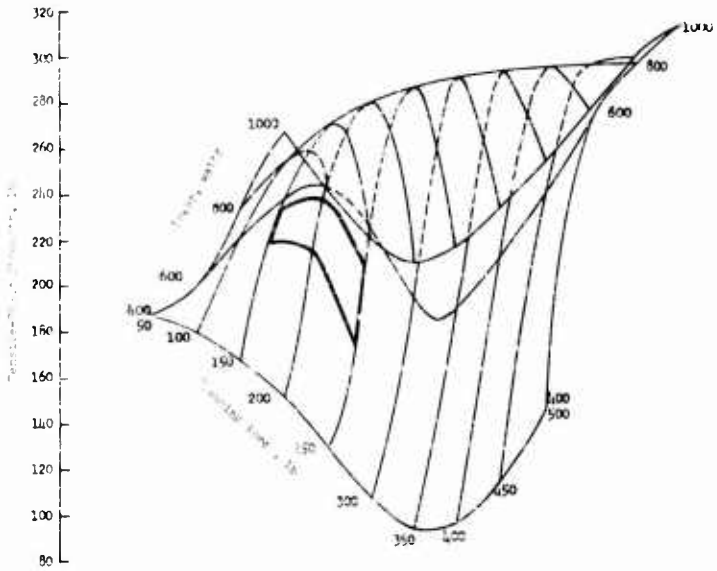


Fig. 20: EFFECT OF CLAMPING FORCE AND POWER ON TENSILE-SHEAR STRENGTH OF A WELD IN 0.005-INCH 302 COLD-ROLLED STAINLESS STEEL

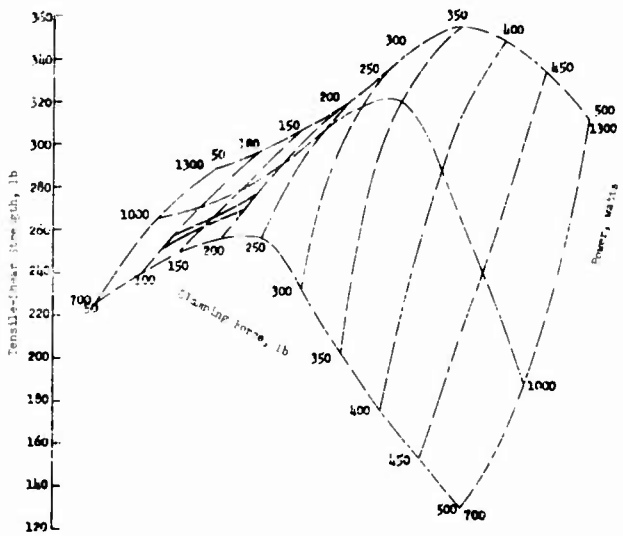


Fig. 21: EFFECT OF CLAMPING FORCE AND POWER ON TENSILE-SHEAR STRENGTH OF A WELD IN 0.010-INCH ANNEALED STAINLESS STEEL

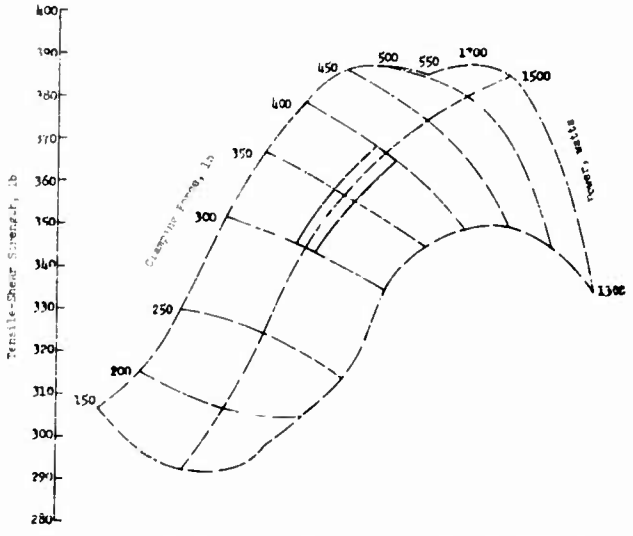


Fig. 22: EFFECT OF CLAMPING FORCE AND POWER ON TENSILE-SHEAR STRENGTH OF A WELD IN 0.020-INCH HALF-HARD COPPER

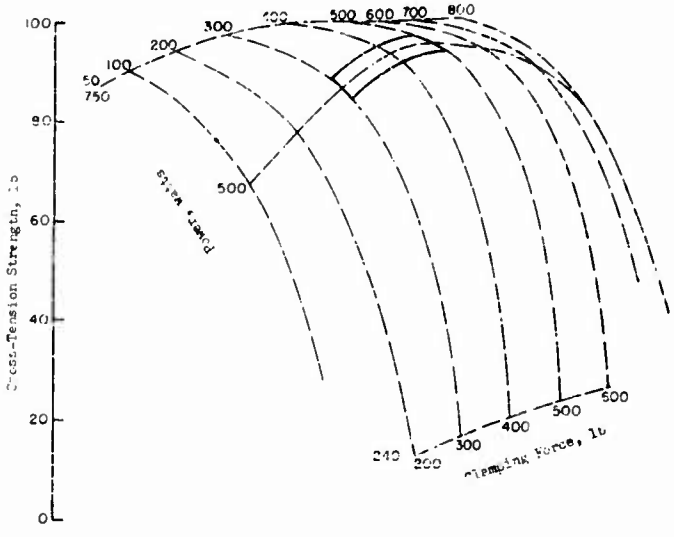


Fig. 23: EFFECT OF CLAMPING FORCE AND POWER ON CROSS-TENSION STRENGTH OF A WELD IN 0.020-INCH 1100-H18 ALUMINUM ALLOY

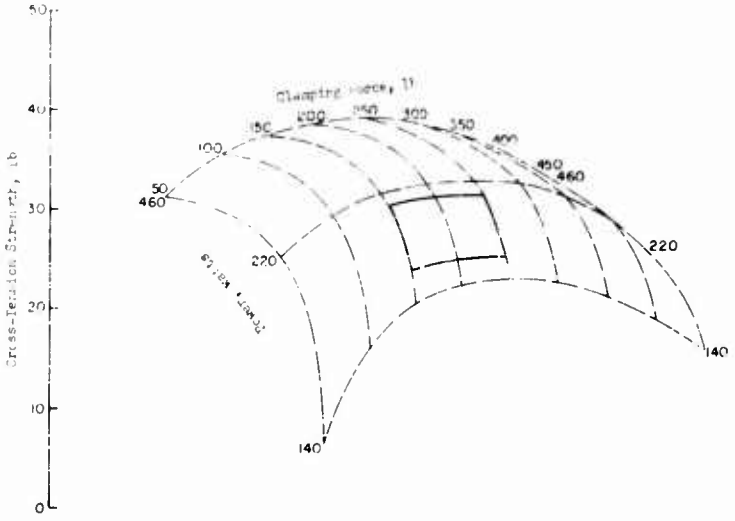


Fig. 24: EFFECT OF CLAMPING FORCE AND POWER ON CROSS-TENSION STRENGTH OF A WELD IN 0.009-INCH 1100-H18 ALUMINUM ALLOY

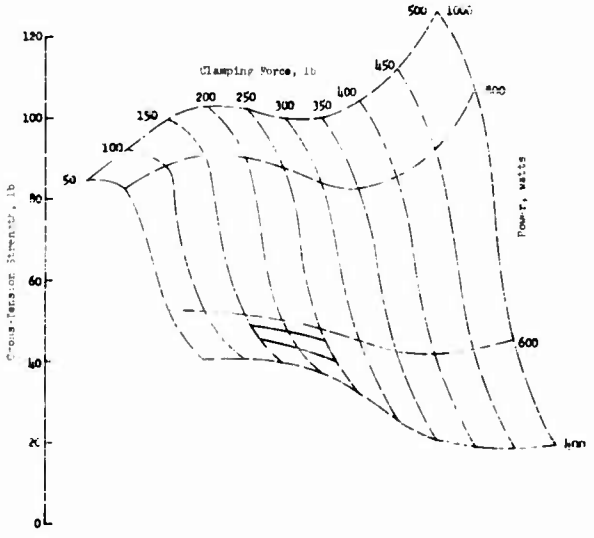


Fig. 25: EFFECT OF CLAMPING FORCE AND POWER ON CROSS-TENSION STRENGTH OF A WELD IN 0.005-INCH 302 STAINLESS STEEL

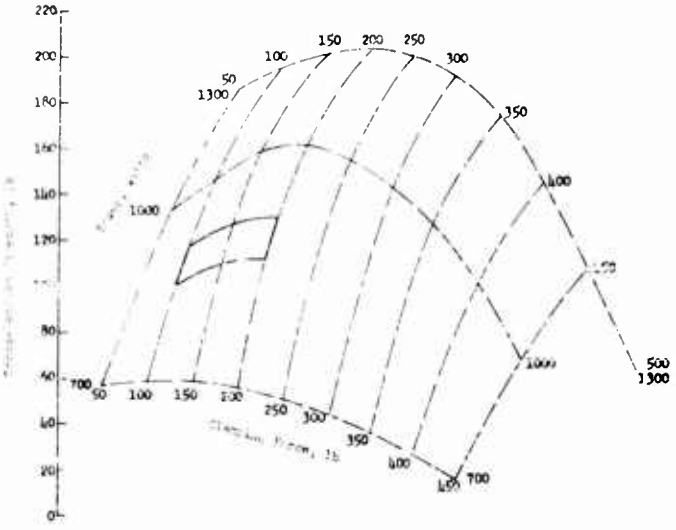


Fig. 26: EFFECT OF CLAMPING FORCE AND POWER ON CROSS-TENSION STRENGTH OF A WELD IN 0.010-INCH 302 STAINLESS STEEL

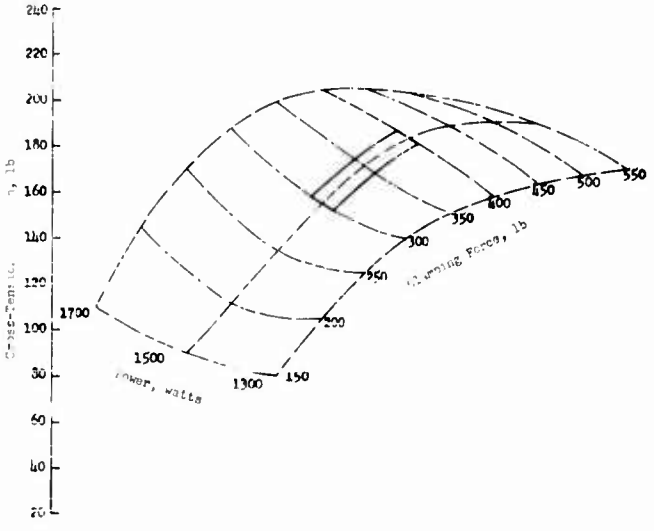


Fig. 27: EFFECT OF CLAMPING FORCE AND POWER ON CROSS-TENSION STRENGTH OF A WELD IN 0.020-INCH HALF-HARD COPPER

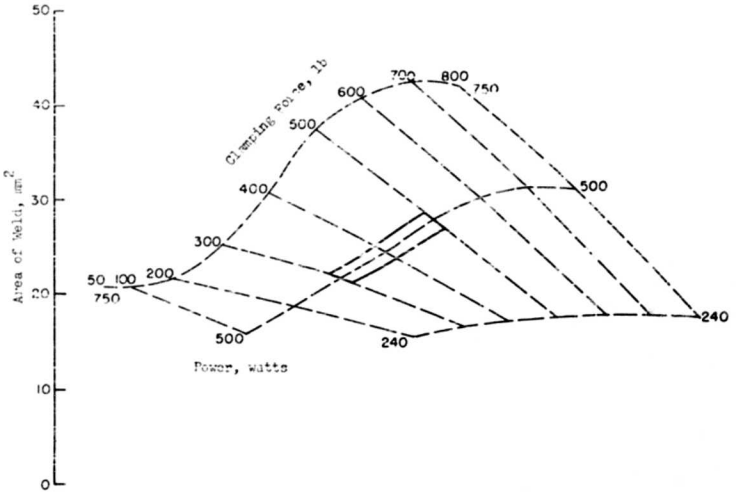


Fig. 28: EFFECT OF CLAMPING FORCE AND POWER ON WELD AREA IN 0.020-INCH 1100-H18 ALUMINUM ALLOY

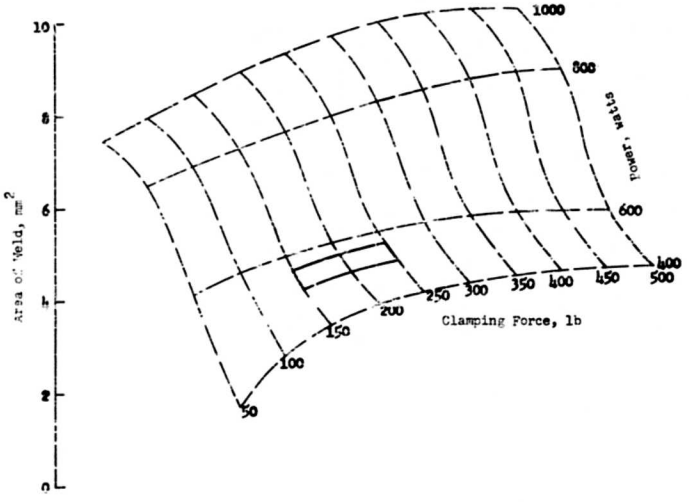


Fig. 29: EFFECT OF CLAMPING FORCE AND POWER ON WELD AREA IN 0.005-INCH COLD-ROLLED 302 STAINLESS STEEL

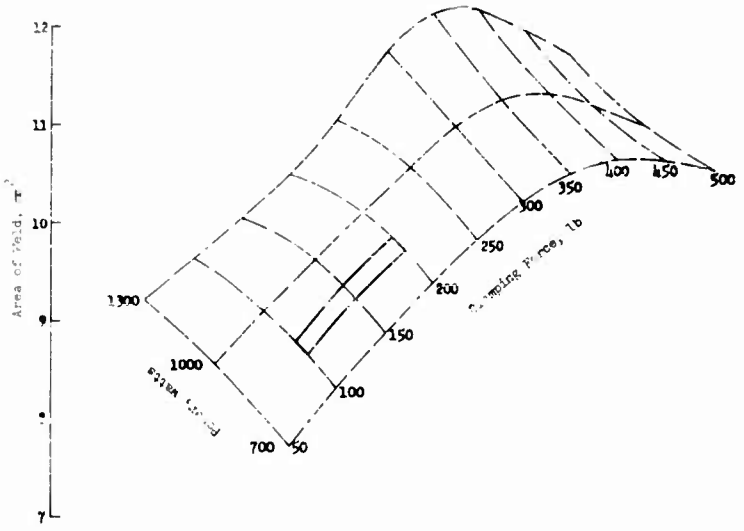


Fig. 30: EFFECT OF CLAMPING FORCE AND POWER ON WELD AREAS IN 0.010-INCH 302 STAINLESS STEEL

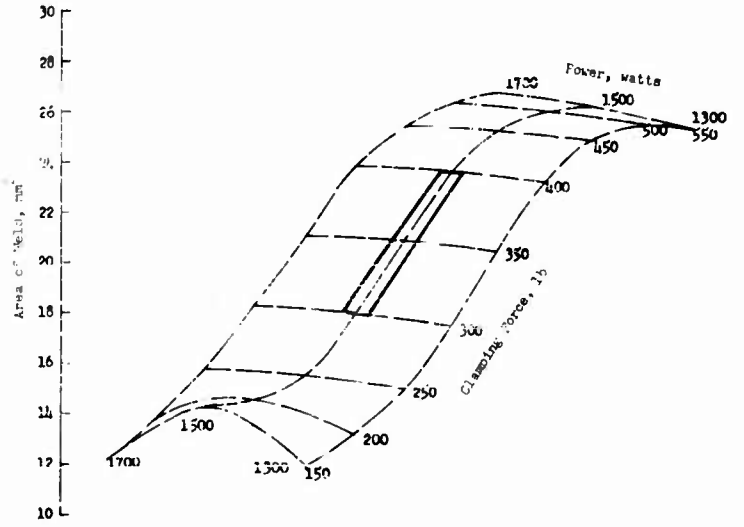


Fig. 31: EFFECT OF CLAMPING FORCE AND POWER ON WELD AREA IN 0.020-INCH HALF-HARD COPPER

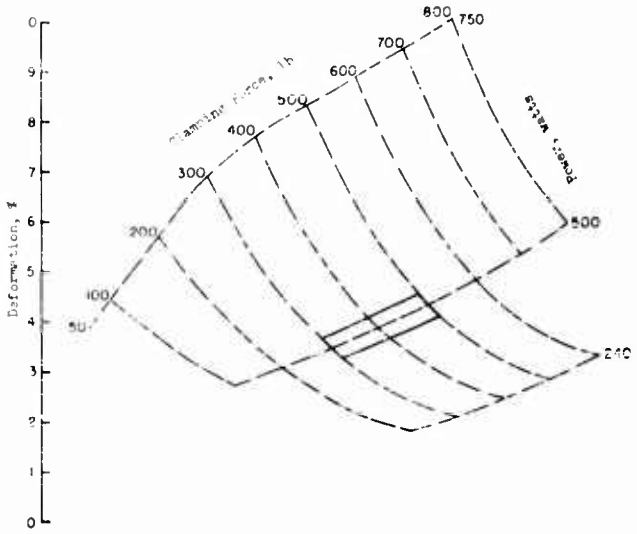


Fig. 32: EFFECT OF CLAMPING FORCE AND POWER ON THICKNESS DEFORMATION OF A WELD IN 0.020-INCH 1100-H18 ALUMINUM ALLOY

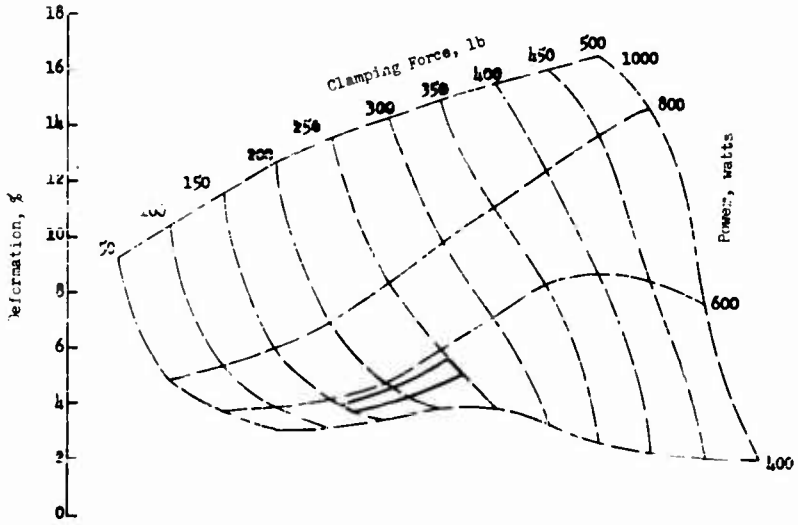


Fig. 33: EFFECT OF CLAMPING FORCE AND POWER ON THICKNESS DEFORMATION OF A WELD IN 0.005-INCH STAINLESS STEEL

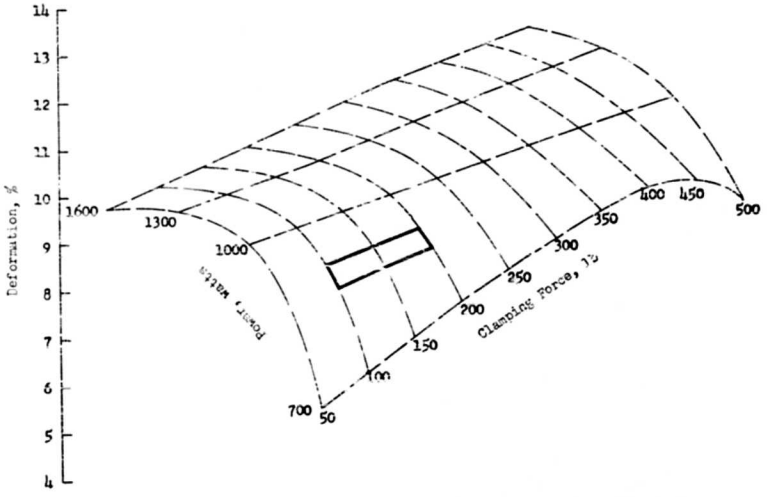


Fig. 34: EFFECTS OF CLAMPING FORCE AND POWER ON THICKNESS DEFORMATION OF A WELD IN 0.010-INCH ANNEALED 302 STAINLESS STEEL

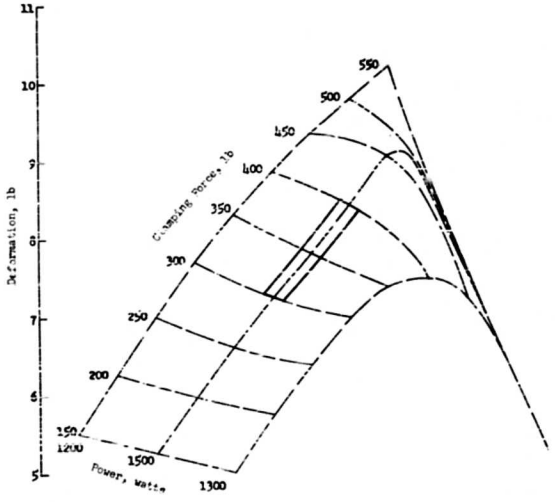


Fig. 35: EFFECT OF CLAMPING FORCE AND POWER ON THICKNESS DEFORMATION OF A WELD IN 0.020-INCH HALF-HARD COPPER

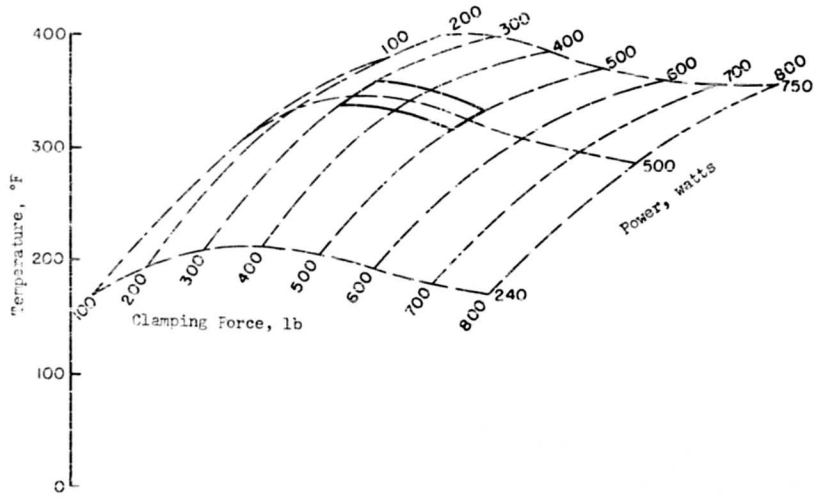


Fig. 36: EFFECT OF CLAMPING FORCE AND POWER ON TEMPERATURE IN THE WELD AREA IN 0.020-INCH 1100-H18 ALUMINUM ALLOY

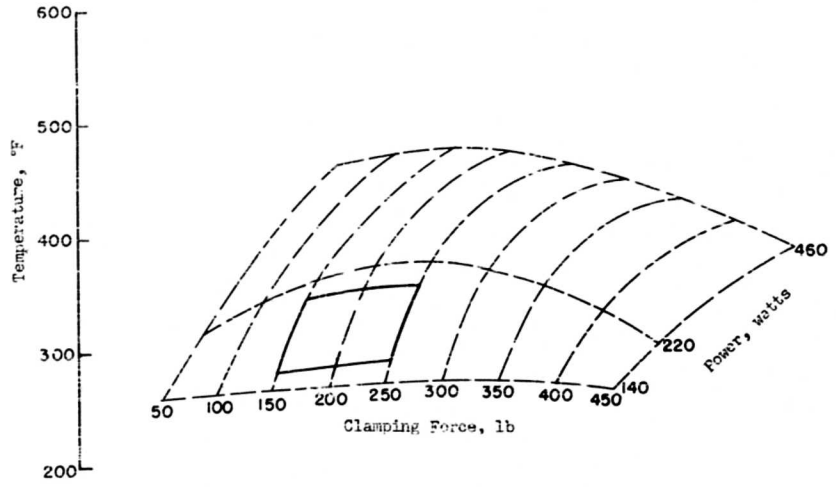


Fig. 37: EFFECT OF CLAMPING FORCE AND POWER ON TEMPERATURE IN THE WELD AREA IN 0.009-INCH 1100-H18 ALUMINUM ALLOY

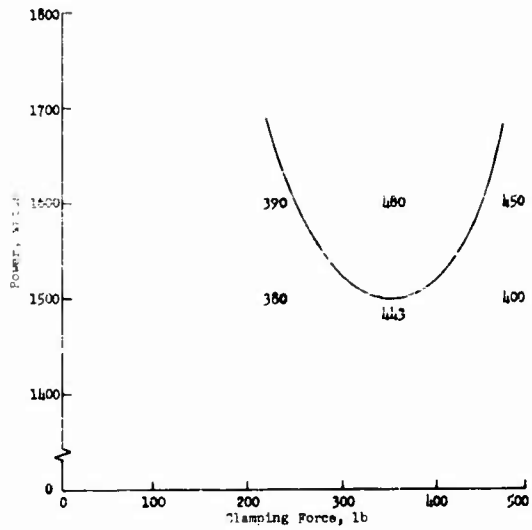


Fig. 38: THRESHOLD CURVE, WITH TYPICAL TEMPERATURES NOTED AT INTERFACE, FOR VARIOUS POWER AND CLAMPING FORCE LEVELS FOR WELDING 0.020-INCH HALF-HARD OFHC COPPER

D. Weld Zone Impedance

One of the fundamental factors to be considered with the efficiency of energy delivery into the weld zone is the impedance presented by the weldment members to the welding coupler tip assembly. This weld zone impedance must depend not only on the welding conditions of power and clamping force but also on the material and material thickness being welded. Preliminary theoretical and experimental studies were undertaken to gain an understanding of the phenomenon.

The equation developed in Appendix D to this report provides a means for calculating the terminal impedance of a coupler rod as a function of the characteristic impedance of the rod itself:

$$\frac{Z_t}{Z_c} = \frac{\xi_{min} \cos \frac{2\pi}{\lambda} X_o - j\, \xi_{max} \sin \frac{2\pi}{\lambda} X_o}{\xi_{max} \cos \frac{2\pi}{\lambda} X_o - j\, \xi_{min} \sin \frac{2\pi}{\lambda} X_o}, \qquad (9)$$

where ξ_{max} and ξ_{min} are the maximum and minimum particle displacement amplitudes in the direction of the vibratory motion, X_o is the

distance from the coupler termination to the nearest maximum particle displacement amplitude, and Z_t and Z_c are the terminal impedance and coupler impedance, respectively. The required information can be obtained with the instrumentation developed for the SWR technique.

Any variation in the SWR as determined from the oscillogram ellipse indicates variation in the acoustic impedance in the weld zone. Furthermore, if one of the SWR-sensing elements is located precisely at an integral number of quarter wave lengths from the terminal end of the coupler ($X_\ell = (N\lambda)/4$), the resulting ellipse will have its major axis parallel to the corresponding deflection axis of the cathode ray tube. Any deviation from these conditions will result in a shift in the node and a concomitant rotation of the ellipse axis relative to the cathode ray tube face. These effects then permit computing impedance, in particular, the reactive component of the terminal impedance.

Instrumentation was assembled and experiments carried out first to obtain an indication of the variation in mechanical reactance at the weld zone at different times during weld formation. A standard 15-kc lateral-drive welding transducer was mounted on the research welder, coupled by a force-insensitive mounting system, and the coupler instrumented with 21 dynamic strain gages covering a half wavelength, each individually attached to a contact on a rotary switch, as illustrated in Fig. 39. With this arrangement, the complete set of sensing elements was swept at a pre-established rate, and single-sweep oscillograms were obtained when the synchronizing voltage was applied to one set of contacts on the rotary switch. Thus it was possible to observe any shift in SWR pattern (shift of the node).

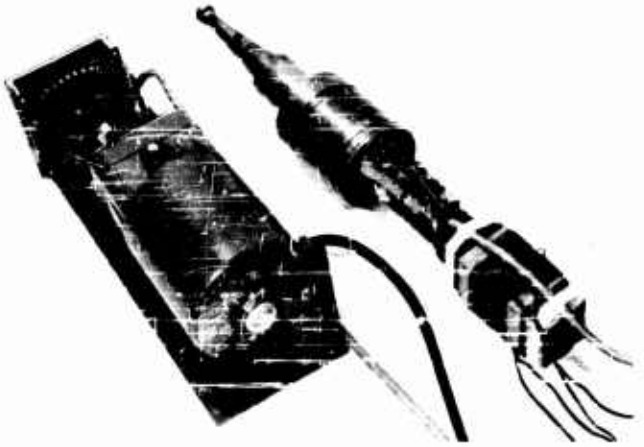


Fig. 39: THE TRANSDUCER INSTRUMENTED WITH 21 DYNAMIC STRAIN GAGES AND ROTARY SWITCH

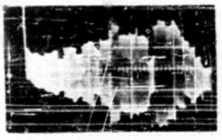
The experiments were carried out by producing welds in each of three materials: 0.050-in. 1100-H14 aluminum, 0.032-in. 2024-T3 aluminum alloy, and 0.032-in. OP copper. The welds in each material were made with a 2-in. spherical radius welding tip and a flat anvil, at 250- and 500-lb clamping force, 800- and 1600-watt electrical power, and a 1.5-sec weld interval. Three welds were made under each condition; Polaroid oscillograms were taken of the first weld at 0.2 sec, during the middle of the second weld at 0.75 sec, and near the end of the third weld at 1.3 sec.

The oscillograms are presented in Fig. 40-42, and Table II summarizes the approximate standing-wave ratios for each condition; the SWR varies from 1.4 to 2.5 during a single weld interval; for efficient utilization of power, the SWR should be close to unity, and minimum variation should occur during the weld interval. The data of Table II reveal the regions of maximum coupling (minimum SWR) and indicate that, within the sensitivity of the present measuring technique, only minor changes occur in the reactive component of weld impedance during the weld interval, as indicated by the change in the location of the nodal region, that is, the longitudinal shift of the area designated "X" on Fig. 40-42.

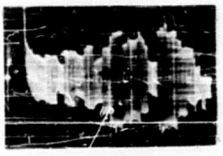
Direct comparison between these and previously obtained data was not possible because different types of transducer-coupling systems were utilized. However, preliminary experiments were carried out with a few selected materials using the cinematic technique for recording variations in the ellipse during the period of weld formation. Calculations from the individual motion picture frames, in conjunction with "Smith Chart", (38) provided data on both the reactive and resistive components of weld zone impedance, as well as the ratio of terminal impedance to the coupler impedance (Z_t/Z_c). Such data for 0.020-in. 1100-H18 aluminum and for 0.032-inch copper are presented in Fig. 43-45. It will be noted that the reactive component for aluminum is essentially constant during weld formation and that the impedance variation is associated primarily with the resistive component. In the case of copper, an increase in impedance, and concomitantly in power delivery, is associated with reduction in the reactive component and an increase in the resistive component during the weld interval.

From this information it may be inferred that for these particular materials the tip displacement associated with the given welding system should be increased somewhat in order to provide a closer acoustic impedance match between the coupler and the weld zone. Furthermore, the shapes of these impedance curves show that the observed variations can be minimized and controlled by force power programming during welding. Further experimentation with this technique with other materials and gages most likely will provide a quantitative basis for improvements in equipment design.

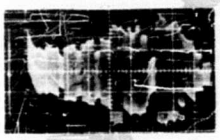
800 Watts Power



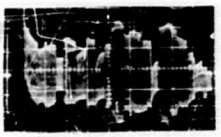
Time: 0.2 sec
Force: 250 lb
SWR: 2.22



Time: 0.2 sec
Force: 500 lb
SWR: 1.95



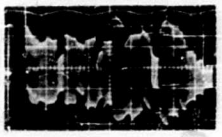
Time: 0.75 sec
Force: 250 lb
SWR: 2.02



Time: 0.75 sec
Force: 500 lb
SWR: 1.48

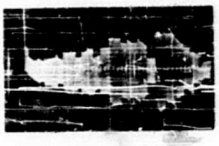


Time: 1.3 sec
Force: 250 lb
SWR: 1.92

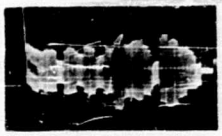


Time: 1.3 sec
Force: 500 lb
SWR: 1.53

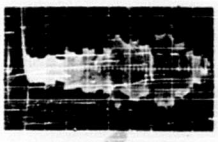
1600 Watts Power



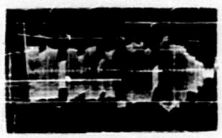
Time: 0.2 sec
Force: 250 lb
SWR: 2.11



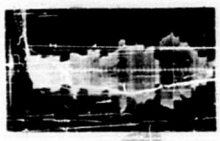
Time: 0.2 sec
Force: 500 lb
SWR: 1.63



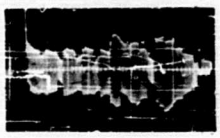
Time: 0.75 sec
Force: 250 lb
SWR: 1.90



Time: 0.75 sec
Force: 500 lb
SWR: 1.38



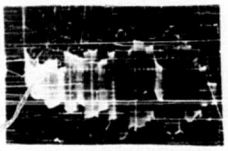
Time: 1.3 sec
Force: 250 lb
SWR: 1.62



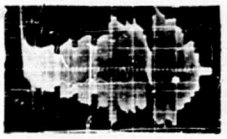
Time: 1.3 sec
Force: 500 lb
SWR: 1.52

Fig. 40: APPROXIMATE STANDING-WAVE RATIO DATA OBTAINED FOR 0.050-INCH 1100-H14 ALUMINUM

800 Watts Power



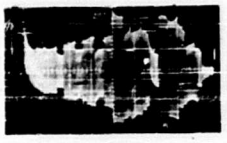
Time: 0.2 sec
Force: 250 lb
SWR: 1.85



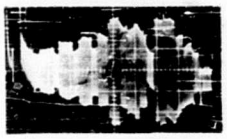
Time: 0.2 sec
Force: 500 lb
SWR: 2.20



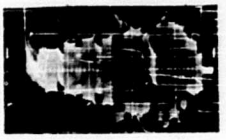
Time: 0.75 sec
Force: 250 lb
SWR: 1.82



Time: 0.75 sec
Force: 500 lb
SWR: 2.04

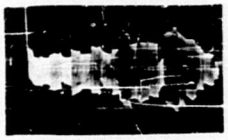


Time: 1.3 sec
Force: 250 lb
SWR: 1.92

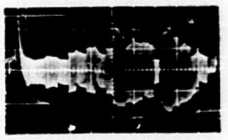


Time: 1.3 sec
Force: 500 lb
SWR: 2.10

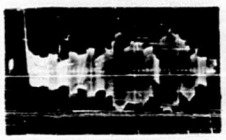
1600 Watts Power



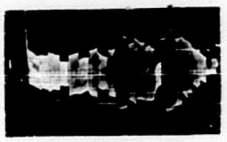
Time: 0.2 sec
Force: 250 lb
SWR: 1.64



Time: 0.2 sec
Force: 500 lb
SWR: 1.95



Time: 0.75 sec
Force: 250 lb
SWR: 1.64



Time: 0.75 sec
Force: 500 lb
SWR: 1.85



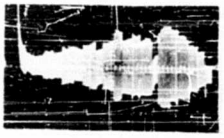
Time: 1.3 sec
Force: 250 lb
SWR: 1.59



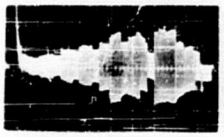
Time: 1.3 sec
Force: 500 lb
SWR: 1.73

Fig. 41: APPROXIMATE STANDING-WAVE RATIO DATA OBTAINED FOR 0.032-INCH 2024-T3 ALCLAD

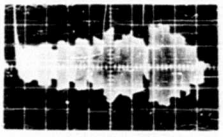
800 Watts Power



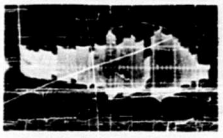
Time: 0.2 sec
Force: 250 lb
SWR: 2.11



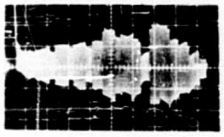
Time: 0.2 sec
Force: 500 lb
SWR: 2.51



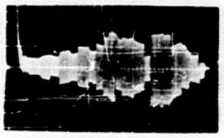
Time: 0.75 sec
Force: 250 lb
SWR: 1.57



Time: 0.75 sec
Force: 500 lb
SWR: 2.0

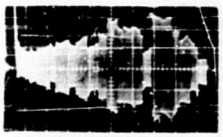


Time: 1.3 sec
Force: 250 lb
SWR: 1.66

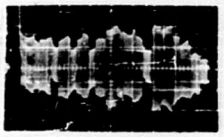


Time: 1.3 sec
Force: 500 lb
SWR: 2.25

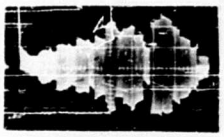
1600 Watts Power



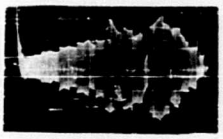
Time: 0.2 sec
Force: 250 lb
SWR: 2.07



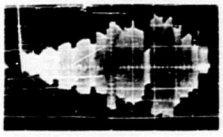
Time: 0.2 sec
Force: 500 lb
SWR: 1.48



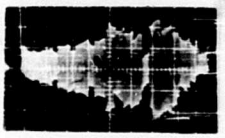
Time: 0.75 sec
Force: 250 lb
SWR: 2.16



Time: 0.75 sec
Force: 500 lb
SWR: 2.08



Time: 1.3 sec
Force: 250 lb
SWR: 2.4



Time: 1.3 sec
Force: 500 lb
SWR: 2.25

Fig. 42: APPROXIMATE STANDING-WAVE RATIO DATA OBTAINED FOR 0.032-INCH COPPER

Table II

SUMMARY OF STANDING-WAVE-RATIO (SWR) DATA FROM OSCILLOGRAMS
(Fig. 40, 41, and 42)

Material	Gage, in.	Power, watts	Clamping Force, lb	Time After Start, sec	SWR	Approximate Variation in SWR
1100 H14 Aluminum	0.050	800	250	0.20	2.22	13.5
				0.75	2.02	
				1.30	1.92	
			500	0.20	1.95	24.1
				0.75	1.48	
				1.30	1.53	
		1600	250	0.20	2.11	23.3
				0.75	1.90	
				1.30	1.62	
			500	0.20	1.63	15.3
				0.75	1.38	
				1.30	1.52	
2024-T3 Alclad Aluminum Alloy	0.032	800	250	0.20	1.85	5.2
				0.75	1.82	
				1.30	1.92	
		500	500	0.20	2.20	7.3
				0.75	2.04	
				1.30	2.10	
		1600	250	0.20	1.64	3.1
				0.75	1.64	
				1.30	1.59	
			500	0.20	1.95	11.6
				0.75	1.85	
				1.30	1.73	
Copper	0.032	800	250	0.20	2.11	25.6
				0.75	1.57	
				1.30	1.66	
			500	0.20	2.51	20.3
				0.75	2.00	
				1.30	2.25	
		1600	250	0.20	2.07	13.8
				0.75	2.16	
				1.30	2.40	
			500	0.20	1.48	34.2
				0.75	2.08	
				1.30	2.25	

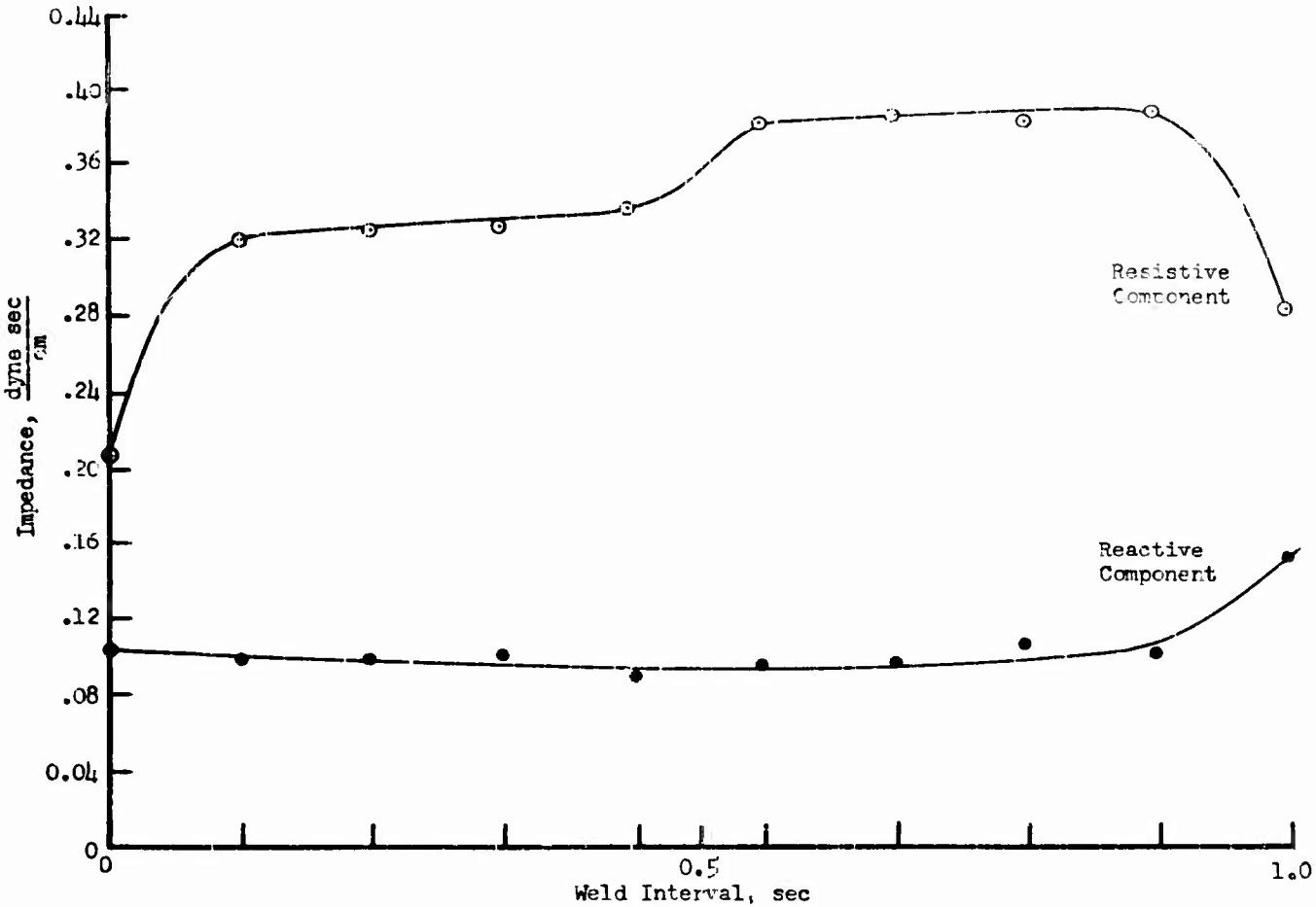


Fig. 43: RESISTIVE AND REACTIVE COMPONENTS OF WELD IMPEDANCE IN 0.020-INCH 1100-H18 ALUMINUM

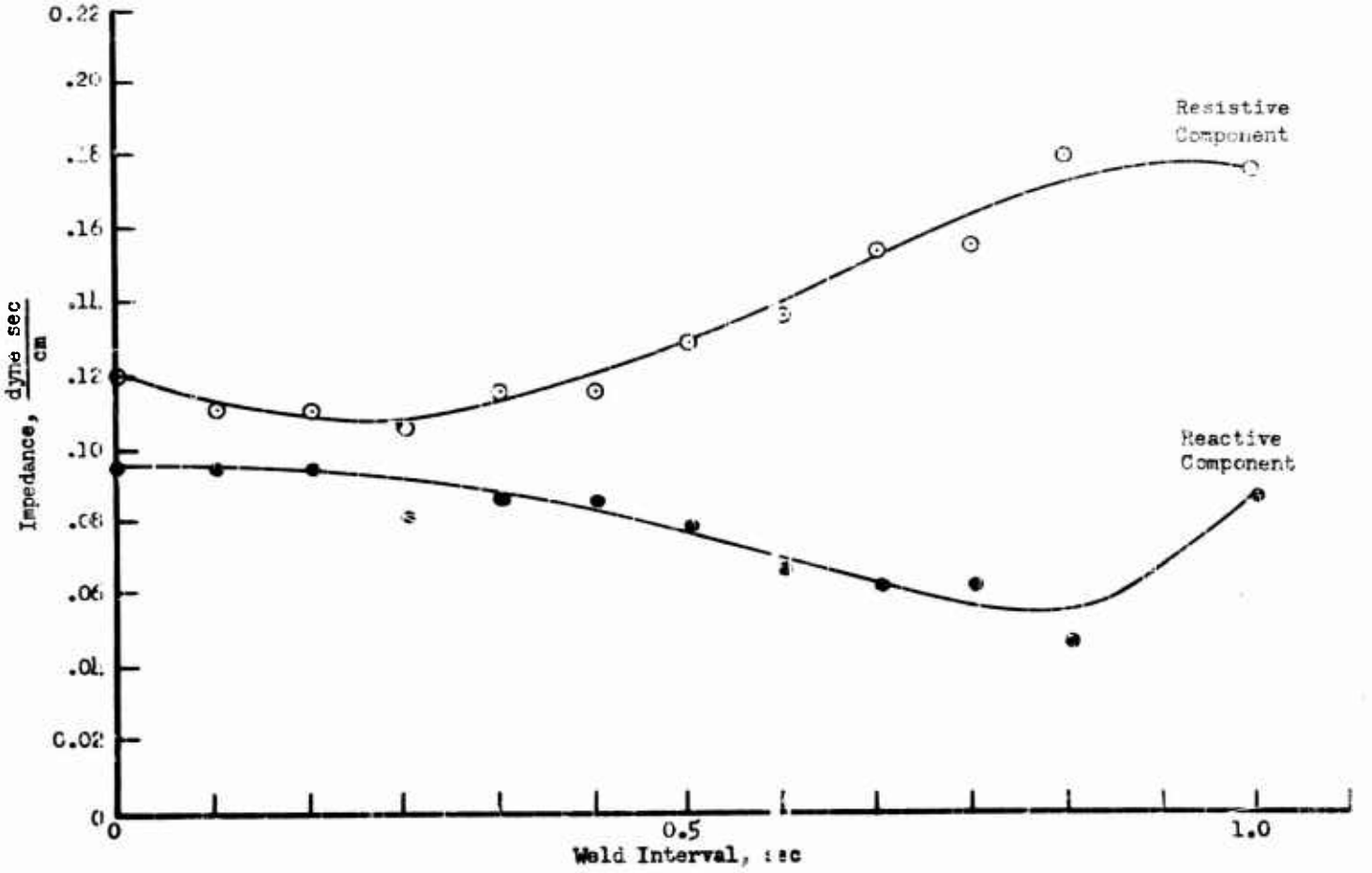


Fig. 44: RESISTIVE AND REACTIVE COMPONENTS OF WELD IMPEDANCE IN 0.032-INCH COPPER

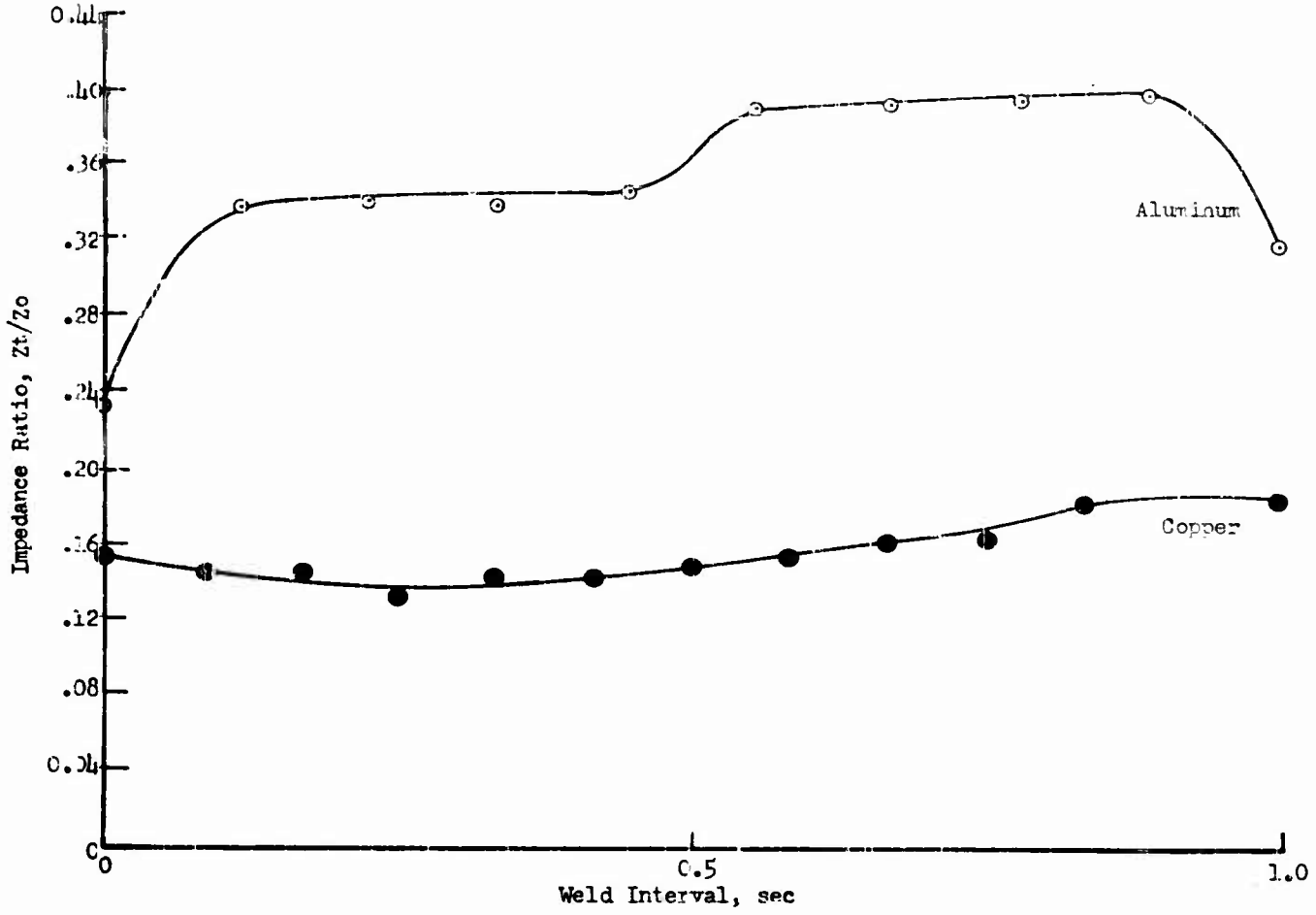


Fig. 45: RATIO OF WELD ZONE IMPEDANCE TO COUPLER IMPEDANCE FOR 0.020-INCH 1100-H18 ALUMINUM AND 0.032-INCH COPPER

IV. MATERIAL PROPERTIES AND WELDABILITY

It is important to be able to predict values for the welding variables of clamping force, power, and weld time that will be required to join metallic materials in terms of their thicknesses and their properties. Of these factors, power is by far the most difficult to produce, to deliver, and to measure.

At least within the modest limits presently associated with the process, it has been shown that vibratory energy (power x time) is significant (4) so that we need not be greatly concerned here with time if it is not overlong. Extended weld intervals, especially when associated with insufficient delivered power and/or improper clamping force, produce tip sticking, cracking of the weldment, and other difficulties. It has also been shown that clamping force is actually a means to control the efficiency and to effect delivery of vibratory power into the weld locale (4). Clamping force is easily provided and is a relatively static factor.

Thus, the energy required to produce a weld and the clamping force requisite to the delivery of that power are significant, with the former being of greatest importance.

Development of the SWR technique for measuring the vibratory power traversing a coupling member overcomes the inaccuracies, difficulties, and complexities of integrated frequency, amplitude, and vibratory (shear) force measurements at the welding tips that have been associated with unsuccessful attempts to evolve some kind of yardstick for vibratory power.

It has been previously shown that the MEC required to produce an ultrasonic spot-type weld between sheets of specific material is significant and that it provides a reproducible correlation of machine settings. The MEC can be considered in any of three frames of reference: (a) the electrical energy input to the transducers, (b) the acoustical or vibratory energy transmitted toward the weld zone by the transducers, and (c) the latter divided by the area of the weld that is generated. These perspectives and the limitations of each have been considered in Phase I of this program (4).

Consideration must be given to the factors associated with the materials being joined.

Vibratory welding involves a complex stressing of the metal in the weld zone and a transient elevated temperature therein of some magnitude. Unusual deformations of the metal at the weld interface occur in some relation with the transient elevated temperature. Clearly the properties of interest may include thermal conductivity, thermal diffusivity,

and melting point, as well as such elastic constants as density and rate of work hardening. Most of these material properties, apparently related to elasto-plastic behavior and, by inference, to ultrasonic weldability, are significantly affected by temperature; and it has been shown previously that the temperature rise during ultrasonic welding is different in different materials (4).

Thus, difficulties are encountered in trying to relate room-temperature material properties to ultrasonic weldability, so that serious attention must be given to considerations of the temperature rise and its relation to material properties and weldability. Therefore, it might seem curious that more energy is required to weld hard 1100 alloy aluminum than soft-annealed aluminum. If greatly elevated temperature properties or melting played a predominant role in welding, this would not be expected. Preliminary experiments show that the foregoing holds also for 302 stainless steel and for nickel as well. Melting, so far as is known, has not been detected in any monometal weld with read-out devices or with an optical or electron microscope. Quick-time properties at quick temperature, concerning which little information could be excavated, seemed to provide an interesting avenue for investigation; but the notion that room-temperature property relationships maintain significance in connection with the power required to generate an ultrasonic weld at elevated temperature has assumed increasing significance in relation to the process. It appears either that (a) the temperature achieved is not particularly significant or (b) that many, and perhaps most, metals and alloys execute a more or less parallel decline in the relevant properties, or both (a) and (b), so that the room-temperature relationships do maintain some proportional relationship to the power required.

Surface film present on the weld metal becomes dispersed in the region of the weld interface and could be expected to influence the weldability of a material. Surface coatings, however, have wide ranges of thicknesses as well as properties and the latter vary with ambient conditions of temperature and humidity. Cursory attention has been directed to this aspect of ultrasonic weldability in the past (2,8,9,13,29) usually toward its effect on the quality of some end item. It is also known that foreign material can be generated during the ultrasonic welding process (1), but this presents no difficulty. This situation is briefly reviewed here and limited attention is given to the influence of a surface film on weldability.

Thus, to associate material properties with ultrasonic weldability the following must be considered: surface conditions, temperature achieved, material properties at temperature, and the energy required to produce a weld.

A. Experimental Equipment, Materials, and Procedures

1. Equipment

The equipment used for this investigation consisted of the small experimental 28-kc welder previously utilized for preliminary studies of net energy delivered to the weld zone at low levels. The electrical power delivered to its transducer was maximum at around 250 watts. A larger, 15-kc machine, also used during Phase I, was utilized for obtaining information on heavier materials. The small unit incorporated the lateral drive system (Fig. 46), and the larger machine incorporated the reed-wedge system (Fig. 47). The coupling system of each was fully instrumented for SWR measurements.

At the outset it seemed that data obtained with these two systems would not be directly comparable due to the differing designs and probably differing efficiencies.

Such a trend did, in fact, exist but the general level of welding energy is in the same range; the data and the results can be coordinated for a reasonable breadth of power, material properties, and material thicknesses.

Weld intervals were 1.0 sec for all gages of all materials, and the welding tip radius was maintained at 2 in. on both machines. The measuring instruments were calibrated periodically, and their accuracy was maintained, within limits, as described in Section III. Welding was carried out at ambient temperature in the range of 68-80°F.

2. Material Properties

Metallographic examination of cross sections of ultrasonic welds in a variety of materials has shown that the zone affected by the ultrasonic process varies from a relatively thin layer immediately adjacent to the weld interface to a grossly disturbed zone encompassing much of the thickness of the sheets being welded. Moreover, the bond envelope area varies for different types of materials of the same thickness. Under these conditions, one would expect to find one or two properties that exert a controlling influence on weldability.

Observations made during the investigation suggested several properties that might have first-order significance. An influence of material hardness on weldability was noted during early ultrasonic welding experimentation. Because of the temperature rise that occurs during welding and the associated heat dissipation, thermal diffusivity is a potentially important factor. In addition, an ultrasonic effect on metal plasticity and reduction in yield strength, which seems to have been demonstrated in metal extrusion (6,17,33) suggested that yield

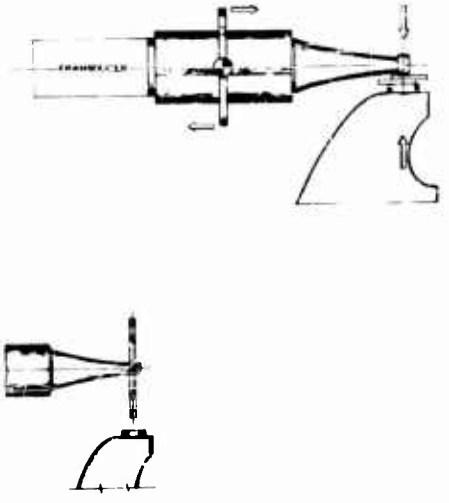


Fig. 46: SCHEMATIC OF LATERAL-DRIVE WELDING SYSTEM

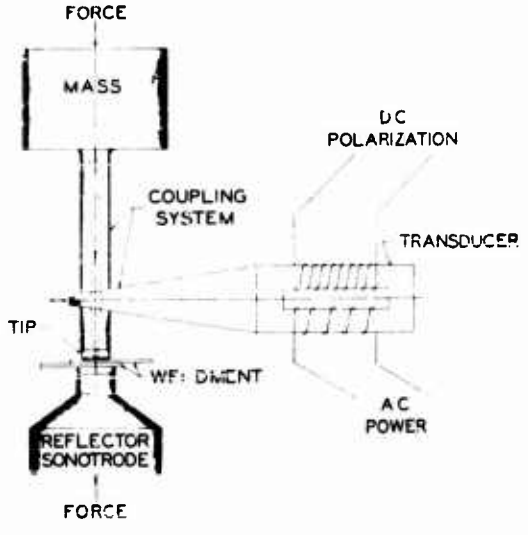


Fig. 47: SCHEMATIC OF REED-WEDGE WELDING SYSTEM

strength might be an important mechanical property. In this connection, it has been observed that, during the ultrasonic welding time interval, the weld interface becomes so plastic that the weldment may be swiveled about the weld axis as long as the ultrasonic energy is applied.

Before undertaking detailed study of the various factors influencing the weldability of a material, brief effort was directed toward obtaining perspective on the problem, particularly to determine that no obvious relationship existed that would eliminate the need for extended effort. To identify any properties which might affect weldability, consideration was given to such physical properties as crystal structure, melting point, density, modulus of elasticity, specific heat, thermal conductivity, thermal diffusivity; to several room-temperature mechanical properties including ultimate tensile strength, yield strength, and shear strength; and to the acoustical properties of sound velocity, specific acoustic impedance, and, for a given material and thickness, the product of weld area and acoustic impedance. Individual values for various materials used in this investigation, where available, are presented in Tables III and IV.

During the ultrasonic bonding process, the weld metal undergoes complex deformation in some degree involving both yielding and work hardening. This deformation is associated with the influence of the transient elevated temperature produced by the ultrasonic energy in and near the weld zone. Plasticity relationships must be related to the fundamental properties. However, the available knowledge concerning plastic deformation is not sufficiently detailed to permit its application to such a complex process. This is apparent when one realizes that the rate of work hardening in such a simple system as single crystal cubic metals is not understood in the second stage of the stress-strain behavior (20). Thus, there appears to be little hope of immediately relating such fundamental properties to the ultrasonic bonding process.

There is, however, an almost obvious way in which this apparent stalemate may be overcome. The use of a composite test parameter which embraces various fundamental properties in a manner approximating the ultrasonic elasto-plastic bonding process should be significant and correlatable.

Appropriate hardness measurements provide a composite of yielding behavior, crystal structure, elastic constants, and work hardening rate. Hardness measurements are determined via a complex deformation mode, and appear to offer a reasonable approximation and a measure of resistance to plastic deformation not unlike the resistance of plastic deformation offered by the material undergoing the ultrasonic bonding. Thus, this apparent analogy of hardness determination to ultrasonic welding has been considered at length.

Table III

ROOM-TEMPERATURE PHYSICAL AND MECHANICAL PROPERTIES
OF MATERIALS USED IN THE WELDABILITY STUDY

	Physical Properties							Mechanical Properties			
								Strength, 10^8 dyne/cm^2			
Material	Crystal Structure	Melting Point, °C	Density, g/cm^3	Elastic Modulus, 10^{11} dyne/cm^2	Specific Heat, cal/g/°C	Thermal Conductivity, cal/cm/sec/°C	Thermal Diffusivity, cm^2/sec	Ultimate Tensile	Tensile Yield	Shear	Hardness, VHN*
Aluminum	f.c.c.	660	2.71	6.89	0.216	0.53	0.360	4.7-11.2	1.2-10.6	--	15-30
Beryllium-Copper	f.c.c.	864	8.23	11.7	0.1	0.20	--	49.6	17.2	--	192
Coin Silver (90Ag-10Cu)	f.c.c.	779	10.3	~8	--	--	--	~42	--	--	--
Copper	f.c.c.	1083	8.96	12.7	0.092	0.94	1.14	23	6.9	--	47
Gold-0.6 Antimony** and Gold-0.6 Gallium**	f.c.c.	1060	19.3	--	0.031	0.71	1.209	13	--	--	27-32
Molybdenum	b.c.c.	2520	10.2	34	0.062	0.32	0.618	69	--	--	180
Molybdenum-Permalloy		1450	8.72	--	--	--	--	--	--	--	--
Nickel—Permalloy	f.c.c.	1455 1450	8.9 8.6	21 --	0.105 --	0.22 --	0.155 --	41.3 --	10.3 --	36 --	90 --
302 Stainless Steel	f.c.c.	1530	7.8	20	0.104	0.11	0.135	40	28	33	117
Tantalum	b.c.c.	3020	16.6	18.6	0.036	0.13	0.238	34-76	--	--	57-118
Zirconium	h.c.p.	1330	6.47	9.99	0.069	0.057	0.093	61	46.8	--	170

* VHN - Vickers Microindentation Hardness No.

** Properties listed are those of gold.

Table IV

ACOUSTIC PROPERTIES OF SELECTED MATERIALS

Material	Thickness, in.	A Weld Area, cm^2	ρ, Density, g/cm^3	c, Velocity, 10^5 cm/sec	ρc, Specific Impedance, $10^6 g/cm^2/sec$	Apc
Aluminum 1100-O	0.001	0.00094	2.71	5.2	1.41	1,320
	.0017	.00340				4,790
	.004	.00444				6,260
Aluminum 1100-H18	.0007	.00110	2.71	5.2	1.41	1,550
	.001	.00139				1,960
	.0017	.00204				2,330
	.004	.01020				14,380
	.009	.02190				31,980
Beryllium-Copper	.0005	.00312	8.23	3.9	3.20	9,980
Copper-OFHC	.0002	.00083	8.96	3.6	3.21	2,660
	.001	.00174				5,590
	.0014	.00264				8,470
	.002	.00419				13,450
Nickel "A"	.0003	.00110	8.9	4.9	4.36	4,800
Nickel-Full Hard	.0005	.00221	8.9	4.9	4.36	9,640
302 Stainless Steel Annealed	.0003	.00054	7.8	5.1	3.98	2,150
	.0015	.00322				12,820
302 Stainless Steel (Half Hard)	.0003	.00046	7.8	5.1	3.98	1,830
	.001	.00078				3,100
Tantalum	.001	.00396	16.6	3.4	5.64	22,330
Zirconium	.00046	.00168	6.47	3.4	2.20	3,700
	0.001	0.00168				3,700

3. Procedures

The metals and alloys used for investigations with the 250-watt and 2-kw ultrasonic welders described, bracket a range of material properties in thicknesses up to about 0.032-in. The materials and gages welded in the 250-watt machine are listed in Table V. The materials and their gages welded with the 2-kw welder are given in Table VI.

All samples were subjected to a standard surface preparation before welding. Each sample was cleaned on the day it was welded by degreasing with a standard commercial detergent solution*. This procedure obviously did not eliminate the potential effect on weldability of surface oxides and other films that may have existed on the materials. The effect of oxide coatings on the weldability of high-purity aluminum was studied, but, clearly, a truly definitive study should be more comprehensive.

Two parameters were used to delineate material weldability: the total acoustic energy delivered to the weld zone and the net acoustic energy per unit weld area. These values were determined for each gage of each material investigated.

The procedure followed was to construct the characteristic threshold curve of clamping force versus the electrical energy required to produce good welds (as defined by the nugget pull-out peel test). With the minimum power and clamping force conditions selected from this curve, several welds were made; in each case, the total acoustic energy delivered to the weld zone was measured by means of the SWR technique described in Section III. The bond envelopes of the individual welds were measured, and the average of these values was used to compute the net acoustic energy per unit weld area. In developing the threshold curve, a minimum of six consecutive nugget pullouts determined each point on the curve. The acoustical value for the MEC was obtained singly in each case; selected materials were later rerun to establish the range of variability. Reproducibility was found to be within 5% for the soft materials, such as aluminum and copper, and within 10% for the harder materials, such as stainless steel.

B. Energy Required to Produce Welds

The data obtained with the two equipment arrays are summarized respectively in Tables V and VI. In addition to identification of the materials and the thickness, the tables include information as to the

* Diversey Chemical Co.

Table V

MINIMUM POWER TRANSMISSION DATA
FOR WELDING VARIOUS MATERIALS AT 28 KILOCYCLES

Material	Thickness, in.	Minimum Electrical Power, watts	Clamping Force, lb	Acoustic Energy, joules	Weld Area, mm^2	Acoustic Energy per Unit Area, joules/mm^2	Hardness,* VHN
1100-O Aluminum	0.001	0.8	1	0.21	0.094	2.2	20-25
	.0017	2	1	0.59	0.340	1.8	20-25
	.004	30	8	9.7	0.444	22	20-25
1100-H18 Aluminum	.0007	0.3	1.3	0.09	0.110	0.8	--
	.001	0.6	2.7	0.14	0.139	1.0	--
	.0017	1.3	4	0.7	0.204	3.3	--
	.004	50	5	6.7	1.02	6.6	45-50
	.009	160	22	65.5	2.19	30	46
Beryllium-Copper	.0005	20	4	5	0.312	16	250
Coin Silver	.00025	5	3	0.78	0.228	3.4	138
Copper	.0002	0.9	12	0.32	0.083	3.9	--
	.001	6	12	0.64	0.174	3.7	80
	.0014	25	27	7.6	0.264	29	98
	.002	30	35	3.6	0.419	8.5	74
Gold-0.6 Gallium	.001	10	12	2.6	0.132	20	103
Gold-0.6 Antimony	.001	50	11	13	0.359	35	64
4-79 Molybdenum-Permalloy	.000125	0.8	0.5	0.25	0.123	2.0	--
Nickel "A"	.0003	6	5	0.74	0.110	6.7	--
Nickel	.0005	9	8	3.7	0.221	17	226
Permalloy	.00049	10	4	3.4	0.330	10	442
302 Stainless Steel, Annealed	.0003	11	2.5	1.8	0.054	34	--
	.0015	100	10	44.8	0.322	138	250
302 Stainless Steel, Half-Hard	.0003	15	2.5	2.3	0.046	49	401
	.001	55	8	16.9	0.078	217	603
	.0015	120	10	33.3	0.145	232	514
Tantalum	.001	75	12	10	0.396	27	239
Zirconium	.00046	28	4	5.8	0.168	35	147
Zirconium, Full-Hard	0.001	45	4	13	0.168	76	286

* Measured Vickers Microindentation Hardness No.

Table VI

MINIMUM POWER TRANSMISSION DATA
FOR WELDING VARIOUS MATERIALS AT 15 KILOCYCLES

Material	Thickness, in.	Minimum Electrical Power, watts	Clamping Force, lb	Acoustic Energy, joules	Weld Area, mm^2	Acoustic Energy per Unit Area, joules/mm^2	Hardness,* VHN
1100-H18 Aluminum	0.006	60	175	8.7	4.92	1.8	37
	.009	95	210	28	7.92	3.6	46
	.016	250	200	79	16.9	4.7	61
	.020	400	400	137	22.2	6.2	64
Copper	.020	1300	350	318	20.0	16	58
	.032	1700	600	302	32.2	9.4	85
Molybdenum	.010	1600	350	173	8.9	19	255
Molybdenum, Annealed	.005	1200	300	135	9.3	15	414
Nickel "A"	.003	100	75	28	1.36	20	133
Nickel	.020	1650	500	291	13.9	21	207
Tantalum	.010	1400	350	174	11.8	15	234
	.005	1200	200	132	9.1	15	171
302 Stainless Steel, Annealed	.025	1800	450	435	15.4	28	130
302 Stainless Steel, Full-Hard	.004	510	150	105	3.66	29	322
	.010	825	325	173	7.6	23	498
	0.020	1600	500	362	12.8	28	292

* Measured Vickers Microindentation Hardness No.

associated clamping force required to make a weld (as determined from the minimum point on threshold curves), the total acoustic energy delivered to the weld zone (as determined by the SWR technique), the average measured weld area, and the acoustic energy per unit weld area. Measured Vickers hardness data are also included except in the few instances in which the materials were too thin to permit accurate determinations of hardness.

It should be noted that the acoustic energy values represent the total energy delivered to the weld zone and include any energy which passes through and beyond the weld zone and is dissipated elsewhere. Further experimental effort is required to determine precisely that fraction of the vibratory energy that may be thus lost and which should, therefore, be deducted from the data presented and discussed. However, it appears that the energy that is lost is small and that this will be true in welding machines designed to take account of this problem.

The same relationship between electrical energy and temper is shown by the stainless steel data. There appeared to be no significant difference in acoustic energy in the very thin gages. However, in this case, the weld area in the annealed material was greater, so that in terms of acoustic energy per unit weld area, the half-hard and annealed curves fall in the same relationship as the electrical energy required.

Tantalum required more electrical energy than any of the other materials investigated, but the efficiency of energy conversion and impedance match into the weld locale was poor, so that in terms of acoustical energy this material is roughly in the middle of the order of weldability for those materials studied.

Table VII gives the order of weldability of some of the materials investigated.

C. Temperature in the Weld Zone

A localized and transient temperature rise of some magnitude in the weld zone during the formation of an ultrasonic weld has long been recognized. Because of the effect of elevated temperature on material properties, it is pertinent to examine more closely this facet of ultrasonic welding.

In Phase I, effort was expended to develop techniques for measuring weld-zone temperatures to determine the actual temperatures achieved in the welding of aluminum, copper, and iron. Two different measuring techniques were used. One consisted of a thin wire thermocouple of a dissimilar metal imbedded in the weld interface as close as possible to the region of maximum temperature (not at the center) of the

Table VII

ORDER OF WELDABILITY OF SEVERAL MATERIALS

Based on Minimum Electrical Power	Based on Acoustic Energy	Based on Acoustic Energy per Unit Weld Area
	A. 28-kc Data	
1100-O Aluminum	1100-H18 Aluminum	1100-H18 Aluminum
1100-H18 Aluminum	1100-O Aluminum	1100-O Aluminum
Molybdenum Permalloy	Molybdenum Permalloy	Copper
Gold-0.6% Gallium	Copper	Coin Silver
Nickel-Annealed	Gold-0.6% Gallium	Molybdenum Permalloy
Copper	Coin Silver	Gold-0.6% Gallium
Nickel, Full-Hard	Permalloy	Permalloy
Coin Silver	Nickel, Full-Hard	Tantalum
Permalloy	Beryllium-Copper	Beryllium-Copper
Beryllium-Copper	Tantalum	Gold-0.6% Antimony
Zirconium	Zirconium	Nickel, Full-Hard
Gold-0.6% Antimony	Gold-0.6% Antimony	Zirconium
302 Stainless Steel, Annealed	302 Stainless Steel, Half-Hard	302 Stainless Steel, Annealed
302 Stainless Steel, Half-Hard	302 Stainless Steel, Annealed	302 Stainless Steel, Half-Hard
Tantalum		
	B. 15-kc Data	
1100-H18 Aluminum	1100-H18 Aluminum	Aluminum
Nickel, Half-Hard	Nickel, Half-Hard	Copper
Copper	Copper	Nickel, Full-Hard
302 Stainless Steel, Full-Hard	Nickel, Full-Hard	302 Stainless Steel, Full-Hard
Nickel, Full-Hard	302 Stainless Steel, Full-Hard	Tantalum
Tantalum	Tantalum	Molybdenum
Molybdenum	Molybdenum	Nickel, Half-Hard

weld locale. The thermal-emf values recorded by this means were representative of interface temperatures in the vicinity of the wire end. The second technique consisted of the insertion in the weld zone of meltable inserts of materials with melting points in the range indicated by the thermal-emf values so that actual interfacial temperatures were bracketed by metallographic examination of melting or nonmelting of these inserts. The results obtained with these three metals indicated that the maximum weld-zone temperature varies as a function of applied power and clamping force. Review of all thermal-emf and meltable-insert data for each of the three materials indicated a variation of approximately ±15% from the average of all power levels investigated at constant clamping force.

It was found that increased power increases the maximum temperature achieved at the interface, and that increased clamping force increases the initial rate of temperature rise but suppresses the maximum temperature achieved. Furthermore, the temperature appears to be related to the thermal conductivity of the material, as the highest temperature was obtained with the material of the lowest conductivity. From the temperature surface plots in Section III of this report, it is concluded that at any fixed power level in the region of the MEC the maximum temperature occurs at the clamping force approximating that associated with the MEC, which is as expected.

It is emphasized that none of the measurements made to date in a monometallic weldment has indicated a temperature approaching the melting point of the metal. Thermal-emf measurements which were recorded on a fast response oscilloscope showed no clearly defined spikes indicative of extraordinarily high temperatures, although such spikes could have occurred locally. However, in no instance of either electron or optical metallographic examination of a monometallic ultrasonic weld is there any evidence of melting at the weld interface.

Recent studies in high temperature metals (24,44) have evaluated elevated-temperature material properties in terms of the homologous temperature, that is, the ratio of the absolute test temperature to the absolute melting temperature. This relationship appears to have significance in associating material properties to welding. In Table VIII the maximum and minimum temperatures recorded in the weld zone during ultrasonic welding of representative metals are listed along with temperatures recorded at the MEC and with the percentage of the absolute melting temperature. It was not possible to obtain interface temperatures for some of the very thin gages of materials where thinness made the studies impractically meticulous and produced excessive scatter in the data.

When it had been determined from the foregoing that the maximum and minimum temperatures ranged between 22 and 63% of the absolute

Table VIII

WELD-ZONE TEMPERATURES ACHIEVED IN REPRESENTATIVE METALS

Material	Recorded Temperature	Melting Point °C	Melting Point °K	Weld-Zone Temperature °C	Weld-Zone Temperature °K	% of Absolute Melting Point	
Aluminum	Minimum	660	933	39	312	40	
	Maximum			316	589	63	
	At MEC			177	450		48
Copper	Minimum	1083	1356	121	394	29	
	Maximum			293	566	42	
	At MEC			227	500		37
Iron	Minimum	1539	1812	121	394	22	
	Maximum			640	913	50	
	At MEC			538	811		45

Table IX

SCOUTING INVESTIGATION OF WELD-ZONE TEMPERATURES ACHIEVED IN METALS OF SPECIAL INTEREST

Material	No. of Temperatures Averaged	Melting Point °C	Melting Point °K	Weld-Zone Temperature °C	Weld-Zone Temperature °K	% of Absolute Melting Point
Nickel	(n=2)	1453	1726	354	627	36.3
Zircaloy-2	(n=2)	1830	2103	733	1006	47.8
Molybdenum-0.5% Titanium	(n=2)	2610	2883	777	1050	36.3
Tantalum	(n=2)	2996	3269	1075	1348	41.2

melting point and that the temperatures measured at the MEC fell between 35-50% thereof, consideration was given to measurements during welding of more materials. Additional scouting tests produced the information summarized in Table IX.

It does appear, therefore, that the temperatures achieved during ultrasonic welding of sheets of like metal, under proper conditions of power and clamping force, near the MEC, do in fact fall between 35 and 50% of the absolute melting temperature.

Additional experimentation is necessary to confirm this concept, but its reliability is clearly indicated.

D. Effect of Surface Condition on Weldability

The interaction between two metal surfaces and the intimacy of their contact depend to a great extent on their surface condition. The characteristics of metal surfaces are altered by the presence of adsorbed gas or oxide films and especially by contaminating films of grease or oil, both of which can affect the weldability of such material.

The metal surfaces normally encountered can be categorized as those existent in the as-fabricated condition; those prepared by liquid chemical treatment, temperature, and atmosphere exposure; and those generated by mechanical treatment. Surfaces may have a mill finish as a result of rolling; an oxide film as a result of air oxidation; or a scaly, extremely tenacious oxide surface as a result of heat treatment. Liquid chemical treatment may consist of etching with a chemical that yields a mat-type finish, polishing with a chemical polish that produces a microscopically smooth surface, or replacing a particular surface with a surface or coating more passive to a given reaction, such as oxidation or resistance to electric potentials. Mechanical treatment of the surface involves abrading, sandblasting, or mechanical polishing.

Successful ultrasonic welding has been achieved with all of these surface conditions. Past investigations have shown that nonscaly mill-finish surfaces and air-oxidized surfaces respond to ultrasonic welding after the surfaces are degreased. Metals containing a heavy heat-treatment scale have caused the most difficulty, and substantially higher powers are usually required to weld them.

It has been found, in general, that welding of difficult and of thick metal surfaces can often be facilitated by the insertion of a thin foil interleaf of the same or of a dissimilar metal between the members to be joined.

Early comparative studies (7) on the welding of 1100 aluminum surfaces cleaned with an alkaline degrease, as well as surfaces etched with various chemical agents, such as solutions of sodium hydroxide, hydrofluoric acid, and nitrogen triacetic acid, showed reproducibly higher strengths than the strengths of specimens that were degreased only. Experiments with 5052-H32 aluminum alloy specimens (10) revealed no significant differences in weld strength when precleaning consisted of degreasing, immersion in caustic etching solution, or Bright-Dip treatment. Similar results were obtained with 5086-H34 aluminum (8).

In the weldcladding of X-8001-H14 aluminum alloy plate with a thin sheet of the same material (3), by ultrasonic seam-welding techniques, best results were obtained with materials that had been given a nonetching alkaline wash. The weld seams were wider; the outside surfaces, cleaner and smoother; the bonds, stronger; and the oxide coatings at the interface, more effectively dispersed.

Some of the bare structural aluminum alloys contain a more refractory oxide coating, which must be removed to effect welds of maximum strength with minimum power. For example (11), specimens of 2024-T3 bare aluminum alloy deoxidized with a caustic etchant developed higher weld strengths at the same power level than did similar specimens that were merely degreased. However, shelf life of the materials after cleaning appears not to affect weld quality. Weldments in this alloy, 2024-T3, showed no decrease in weld strength even when 6 months were allowed to elapse between cleaning and welding. In contrast to its effect on resistance welding, reoxidation after cleaning apparently is not detrimental to ultrasonic weld quality.

With certain materials, scraping has been used to remove the oxide coating. Weld specimens of 2014-T6 bare aluminum alloy (2) showed higher strengths and less strength variability when the surfaces had been scraped before welding than those obtained with surfaces treated with a caustic etchant or with a mild alkaline wash.

Other metals have been treated according to the nature and thickness of surface films. Tantalum, for example, is effectively welded after alkaline degreasing. Molybdenum surfaces require a light etching treatment for most effective welding. Materials such as the J-1500 nickel alloy are ordinarily welded after slight abrasion of the surface. In very early comparative studies with Inconel-X containing heavy oxide scales resulting from solution heat-treatment, good welds were produced both with and without prior deoxidation in an etching solution. Weld strengths were approximately the same, although there was less scatter of strength data for the specimens which had been deoxidized.

Quality welds have also been made through artificially introduced protective or replacement coatings on metals. Several years ago, anodized 1100-H18 aluminum was welded through film coatings up to 2500 Å thick. No strength tests were made on these specimens, but metallographic examination indicated that the extent of oxide film disruption at the interface decreased with increase in anodic coating thickness.

Low-carbon steel with both organic and inorganic coatings has been bonded (12). With organic coatings, the vibration introduced through the welding tip initially expels or breaks up the film at the weld interface, leaving bare surfaces in the weld area where metallurgical bonding can occur. Steel specimens coated with zinc or aluminum exhibited bonding in the clad layer.

An independent study (29) on the attachment of leads to ribbon coil transformers demonstrated the ultrasonic weldability of aluminum to aluminum and aluminum to copper through insulation coatings, including anodized and polyvinyl plastic coatings. It was concluded that ultrasonic welding provides sound electrical connections involving these materials, producing joints at least equivalent to those produced by electrical discharge welding and markedly superior to soldered joints.

With this background concerning the effect of surface condition on weldability, consideration was given to further experiments ranging from simple industrial degreasing to complete stripping of the surfaces to be joined, with subsequent storage and use under very exacting vacuum or inert atmosphere conditions. The extensive amount of work that would be required for even a cursory examination of the effects of surface condition on a broad basis probably is not justified and that the magnitude of the effect is probably not of the first order. It was recognized that stripping materials and rigid atmosphere control, although of academic and fundamental interest, are not representative of conditions under which practical ultrasonic welds are made.

A modest study to confirm the effect of oxide coating thickness on the weldability of a given material was considered to be of general interest. High-purity aluminum, 0.034-in. thick, containing oxide coatings ranging from 500 to 3000 Å thick, was studied.

A Latin square experiment (45) involving parameters of oxide thickness, clamping force, and power level was carried out. Subsequent statistical analysis, summarized in Table X, showed no significant effect of surface oxide thickness on weld strength at the 99% probability level (Table XI). The standard deviation of tensile-shear strengths for the entire experiment is 10.75 lb, which indicates the consistency of ultrasonic welds produced within the limitations of the experiment.

Table X

TENSILE-SHEAR STRENGTH DATA
FROM LATIN SQUARE DESIGN EXPERIMENT
ON ALUMINUM OXIDE FILM IMPREGNATED
0.0335-INCH HIGH-PURITY ALUMINUM

Mean ± 90% Confidence Interval
Time: 1-1/2 sec, constant

	Oxide Thickness Level, Å					
	500		1000		3000	
Power, watts	CF,* lb	T-S,** lb/spot	CF,* lb	T-S,** lb/spot	CF,* lb	T-S,** lb/spot
1000	600	420 ± 30	400	410 ± 20	500	440 ± 30
1300	500	455 ± 20	600	450 ± 20	400	440 ± 10
1600	400	450 ± 20	500	455 ± 10	600	480 ± 10

* Clamping Force.
** Tensile-Shear Strength.

Table XI

ANALYSIS OF VARIANCE FOR THE EXPERIMENTAL DATA
PRESENTED IN TABLE I

Source of Variation	df	Sum of Squares	Mean Squares	F	Level of Significance
Power, watts	2	6548.032	3274.016	28.32	P 99.9%
Oxide Coating, Å	2	1003.328	501.664	4.34	P 95%
Clamping Force, lb	2	1706.453	853.226	7.38	P 97%
Replicates	2	228.588	114.294	0.99	
Experimental Error	18	2078.993	115.4996		
Total	26	11,565.394			

This work was later extended in a cursory examination of oxide thicknesses of 0.001 and 0.003 in. anodically applied to 0.020-in. 1100-H18 aluminum. With the 0.001-in. coating, welding occurred over only part of the normal weld area, while the material with the 0.003-in. coating could not be welded at all, even at the maximum power available. Inspection of the weld interface in both cases revealed that, although the surface film was broken up and fragmented, the oxide fragments remained within the weld area, apparently preventing contact and welding of the base metal.

Thus, moderately thick oxide surfaces (up to about 3000 Å thick) apparently do not influence the welding of aluminum. However, as the surface oxide is increased beyond about 0.001 in., welding could not be accomplished under the experimental conditions used. In this regard, it is believed that the absolute value of the oxide thickness, rather than the fractional value of the total weld material thickness, is significant if the coating is thick. Further experiments with a wider range of material thicknesses would be of interest.

E. Welding Energy as a Function of Hardness and Thickness

Sufficient information was developed to permit a more detailed review of material properties and their significance in the ultrasonic welding process and, in particular, the order of this significance. Evidence of a correlation between room-temperature hardness and weldability was noted throughout this work, although a rationale for it was not at first clear.

For further confirmation samples from sheets of nickel and Type 302 stainless steel were welded in the as-received condition, and samples from the same sheets after annealing were also welded. The power required to weld the samples is plotted (Fig. 48) as a function of thickness with hardness as a parameter. Data on aluminum of H18 and O temper are similarly plotted in Fig. 49.

The lowest power value for the 0.004-in. aluminum in Fig. 49 is actually two points which were obtained by welding specimens of both 1100-H18 and 1100-O after complete annealing to a dead-soft condition. As expected, the hardnesses so achieved were equally weldable. Subsequently all data were reviewed in the light of this information.

The data obtained with the small machine (Table V) were plotted as a function of the sheet thickness for each material and, although in a number of instances only one gage of a given material was available for experimentation, those materials on which multiple thicknesses were available provided sufficient data for plotting.

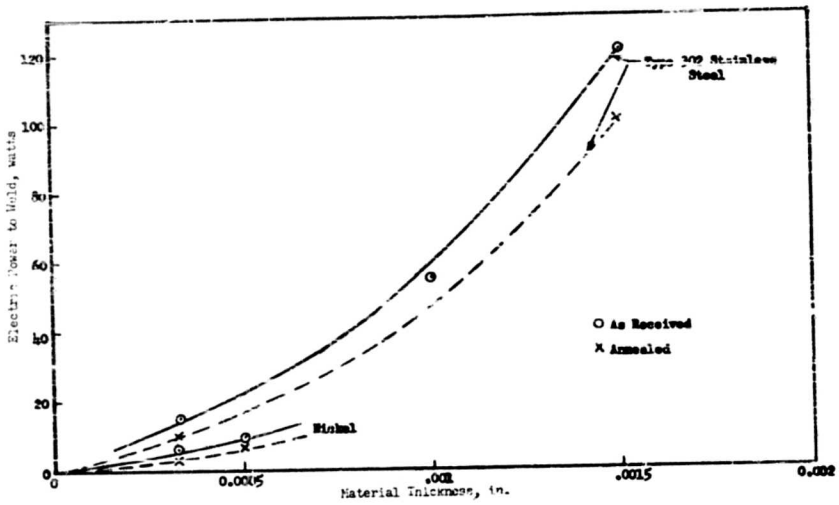


Fig. 48: COMPARISON OF POWER REQUIRED TO WELD TYPE 302 STAINLESS STEEL AND NICKEL

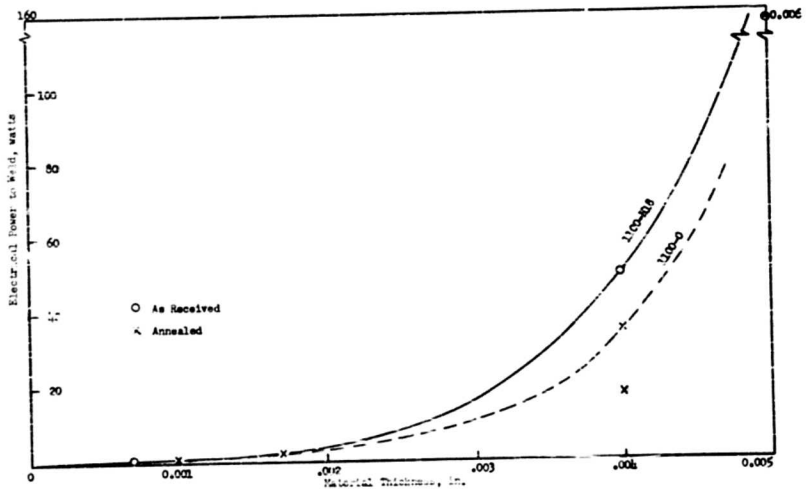


Fig. 49: COMPARISON OF POWER REQUIRED TO WELD 1100-H18 AND 1100-0 ALUMINUM ALLOYS

The data at 15 kc generally confirmed the 20-kc data, although some anomalies are evident. These probably can be explained on the basis of impedance matching between the transducer coupling system and the weld zone, but it does seem desirable to mention the possible role of frequency in the vibratory welding process. It appears that within the range normally considered for vibratory welding, frequency, per se, has no significance in weld formation.

However, it also appears that the limitations imposed by available engineering materials and practical dimensions on transducer-coupling systems, result in an apparent frequency effect that is quite independent of the principles which make the vibratory or ultrasonic welding process operative (Appendix E).

Figure 50 shows the minimum acoustic energy required to weld the various materials with the small welding machine, as a function of thickness, while Fig. 51 shows the same data after they were normalized to account for the area (energy per unit weld area). Joining the various thicknesses of each material clearly indicates the order of weldability shown in Table VII. Specific materials in this group were selected for closer examination and indication of trends. Figure 49 shows the curves of electrical power versus sheet thickness for 1100 aluminum in the H18 and mill-annealed conditions. As previously noted, more energy was required to weld the harder material. Additional specimens were from the 0.004-in.-thick sheets of both materials from which nal data had been obtained; these were fully annealed to the condition to eliminate any hardness effect. Threshold curve o tained after annealing of both H18 and O condition aluminum show precisely the same minimum energy requirements as indicated by the low point on Fig. 49. The mill-annealed material was not in dead-soft condition when received.

The hardness effect on weldability was confirmed by data obtained with 302 stainless steel and nickel (Fig. 48), which were first evaluated in the "as-received" condition (half-hard stainless steel and full-hard nickel) and then evaluated after full annealing.

1. Hardness

The hardness of a material is its resistance to plastic deformation of various types, including cutting, scratching, abrasion, and indentation. "Hardness, probably the first characteristic used to distinguish different kinds of matter, is recognized as one of the fundamental properties of matter" (18). Unfortunately, it is closely associated with other material properties and is not based on rigorous theory.

The methods used to determine this property fall into two distinct categories (18) as follows:

a. Indentation tests in which the surface of the material under test is permanently distorted by the normal pressure of a hard steel ball, cone or knife edge

b. Abrasion or scratch test in which the particles of the material under test are torn away from its surface by sliding contact with some other substance with a surface resistance high enough to remain unimpaired.

The microindentation test used to determine hardness appears closely akin to the internal deformation associated with vibratory welding. The Vickers microindentation test perhaps best embraces a wide range of material properties. It is based upon microindentation measurements and empirical correlation of Vickers numbers with several material properties. The Vickers microindentation hardness numbers were obtained for each of the materials in the spectrum of its vibratory weldability.

As indicated, initial efforts on the basis of the data obtained with the small 250-watt experimental welder produced the curves of Fig. 52 to 54 connecting the effects of hardness and sheet thickness irrespective of material. Figure 52 is a plot of the minimum total acoustic energy required to make a weld in the thin gages of material as a function of a Vickers hardness number with parameters of sheet thickness. Figure 53 shows the same data with acoustic energy plotted against sheet thickness with parameters of hardness. Both of these plots indicate that more energy is required to make a weld as both thickness and hardness increase. However, the influence of hardness appears to diminish and possibly to reach a limiting value. In Fig. 54 in which acoustic energy per unit weld area is plotted as a function of the hardness with parameters of material thickness the limiting effect of hardness is not apparent.

Subsequently, these data were combined with data obtained with the 2-kw welding array, which involved thicker materials. All these results were plotted in terms of the acoustic energy as a function of material hardness, and smooth curves providing a best fit with the data were drawn for each of several arbitrarily selected sheet thickness ranges. The best correlation was found in terms of total acoustic energy, although in some of the thicker gages the effect is somewhat obscured by the scale used in making the plot. The correlation obtained with acoustic energy per unit weld area was not quite as satisfactory over the entire range of thickness covered, although some correlation appeared to hold over limited regions. Additional work will be required with considerably greater precision in weld area measurement to determine whether the normalized acoustic energy likewise relates primarily to hardness and thickness.

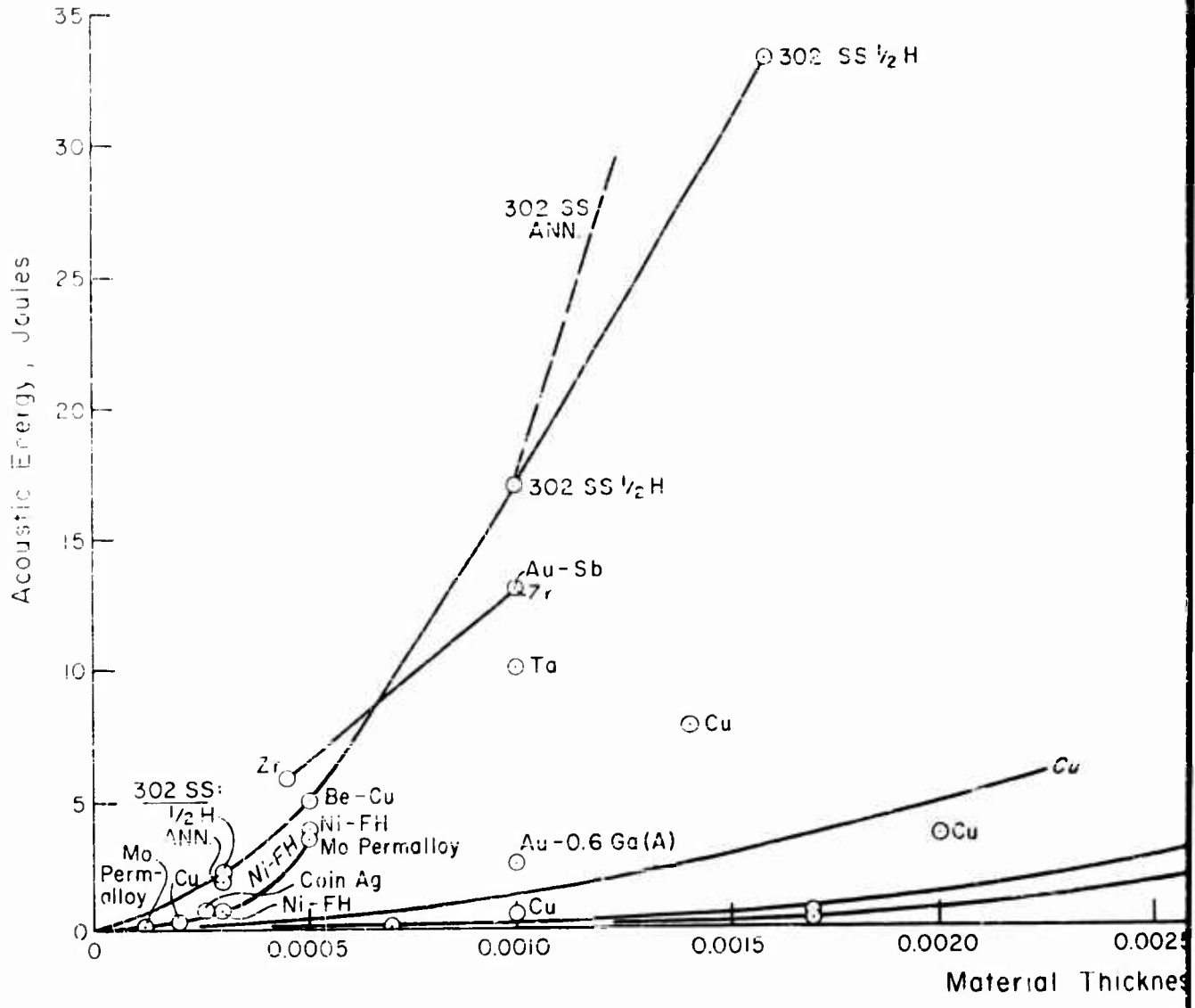
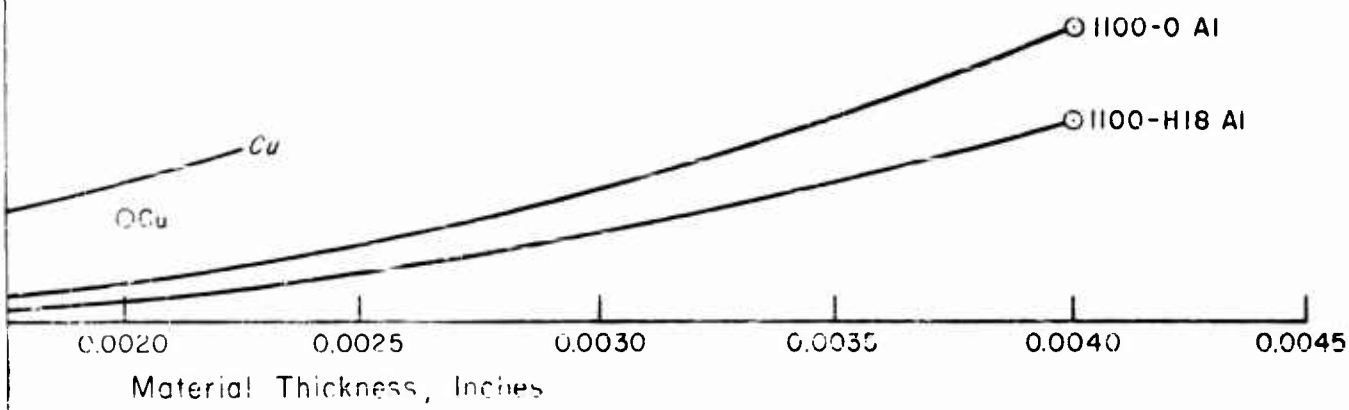


Fig. 50: TOTAL ACOUSTIC ENERGY REQUIRED TO WELD WITH 28-KILOCYCLE EXPERIMENTAL WELDING

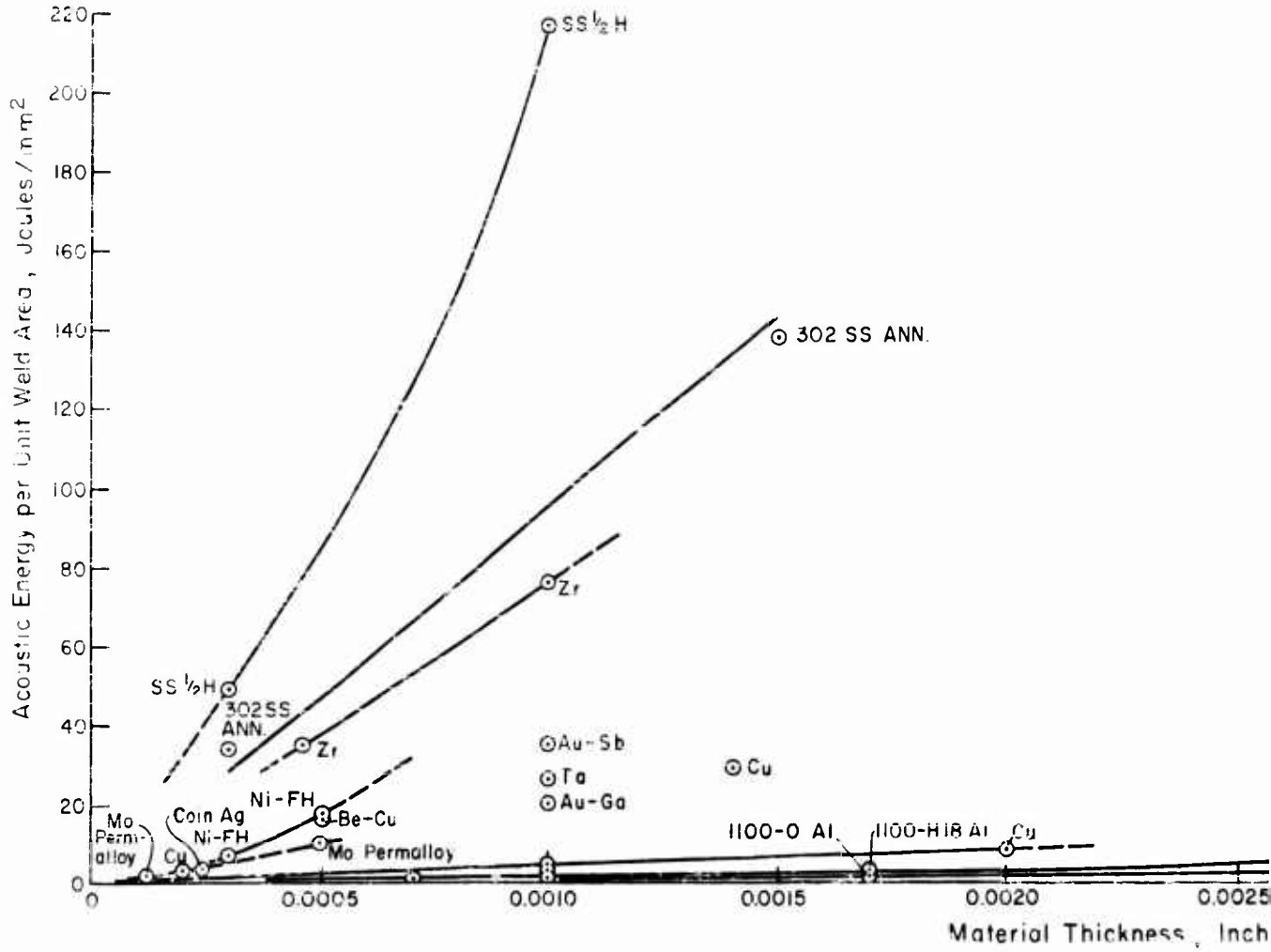
1

SS ½ H



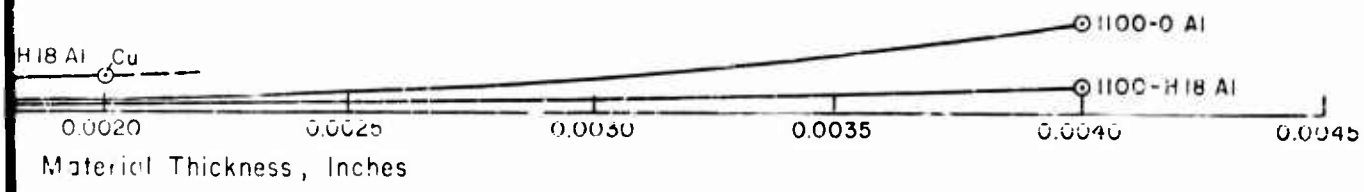
USTIC ENERGY REQUIRED TO WELD SEVERAL MATERIALS
ILOCYCLE EXPERIMENTAL WELDING ARRAY

Fig. 50



1

Fig. 51: ACOUSTIC ENERGY PER UNIT WELD AREA REQUIR
MATERIALS WITH 28-KILOCYCLE EXPERIMENTAL



GY PER UNIT WELD AREA REQUIRED TO WELD SEVERAL
H 28-MILLICYCLE EXPERIMENTAL WELDING ARRAY

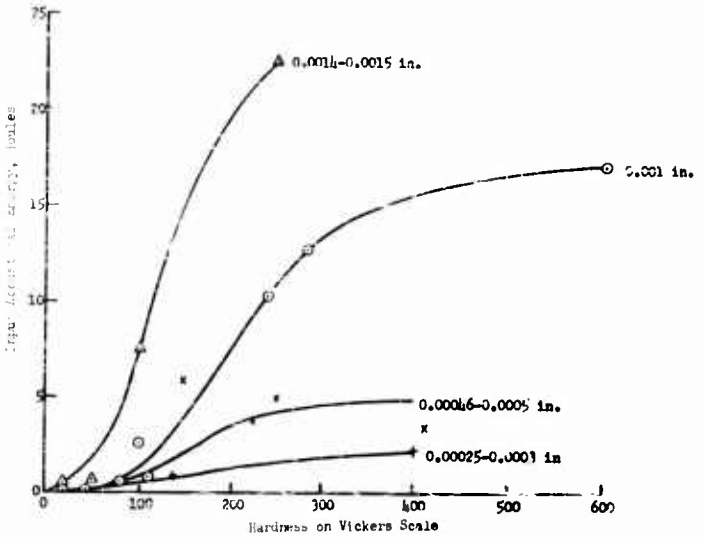


Fig. 52: ACOUSTICAL ENERGY REQUIRED TO GENERATE A WELD AS A FUNCTION OF HARDNESS WITH PARAMETER OF MATERIAL THICKNESS

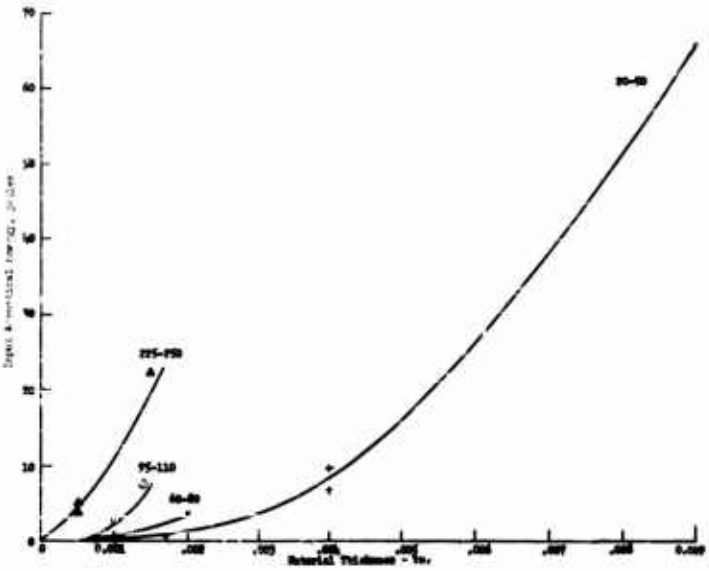


Fig. 53: ACOUSTICAL ENERGY REQUIRED TO GENERATE A WELD AS A FUNCTION OF MATERIAL THICKNESS WITH PARAMETER OF VICKERS HARDNESS

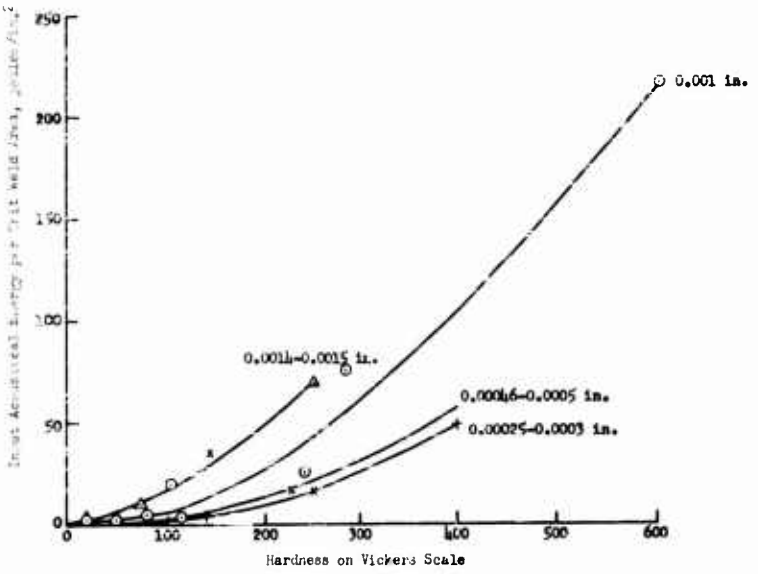


Fig. 54: ACOUSTICAL ENERGY REQUIRED TO GENERATE A WELD AS A FUNCTION OF HARDNESS WITH PARAMETER OF MATERIAL THICKNESS

The curves provided by these data suggested that a mathematical representation of these parameters has the form:

$$E = Kf(H)f(t), \tag{11}$$

where E represents the appropriate minimum acoustic energy required to make the weld in watt-seconds or joules, K represents a linear fitting constant, and f(H) and f(t) represent unknown functions of hardness and thickness, respectively. Computations were made for the acoustic energy, and a good fit with the empirical curves was obtained when both the hardness and the thickness varied as the 3/2 power. Thus, the equation has the form:

$$E = K H^{3/2} t^{3/2}. \tag{12}$$

Although K is considered a constant, it is probably a complex function incorporating several material properties, none of which appear to contribute in the first order. Furthermore, the equation representing these data should be basically the same for both the electrical and acoustical cases, and the constant should include a factor representative of the transduction efficiency of the transducer. The value of the constant K as it applies to the acoustic energy delivered was found to be 63. Therefore, within the limits of a 2-kw welding

machine, and up to about 0.032-in. material thickness, the acoustic equation is:

$$E_a = 63\, H^{3/2}\, t^{3/2}, \qquad (13)$$

where E_a is the acoustic energy in joules (watt-seconds), H is the Vickers microindentation hardness number, and t is the material thickness in inches.

Equation (13) is reasonably fundamental because it relates the acoustic energy actually utilized to make a weld to the Vickers microindentation hardness number and thickness.

A family of curves based on this equation is shown in Fig. 55, and the experimental points, taken from the data of Tables III and IV, are included. It will be noted that several of the points fall outside the area bracketed by a given sheet thickness range according to the theoretical equation. As noted, it is probable that the assumed constant K includes the effect of other material properties as second-order variables; in particular, this constant would be expected to account for the thermal diffusivity of the materials being welded. Further investigation, however, will be required to determine the composition of this factor.

These equations provide a first approximate criterion for determining the weldability of a given material and material thickness in terms of vibratory power. Perhaps it is best to confine its use to the materials and thickness ranges investigated here, since the equation is not founded upon rigorous theoretical parameters but rather on a curve-fitting process. Closer consideration of the equation, however, indicates that there may well be substantial theoretical grounds for its use.

As already mentioned, hardness is a composite parameter determined by crystal structure, yield strength, and rate of work-hardening of the material for which the hardness is determined. These same material properties affect the ease of complex deformation involved in producing an ultrasonic weld. It is not an unreasonable assumption that hardness can be used as a first approximation to gage the way the metal should behave during vibratory welding.

One is hesitant, however, to use the room-temperature hardness determination as indicative of the higher-transient-temperature, complex deformation behavior involved in ultrasonic welding. In the foregoing acoustic equation there is apparently no basis to support relations between room-temperature hardness and the elevated-temperature elastoplastic conditions of ultrasonic welding.

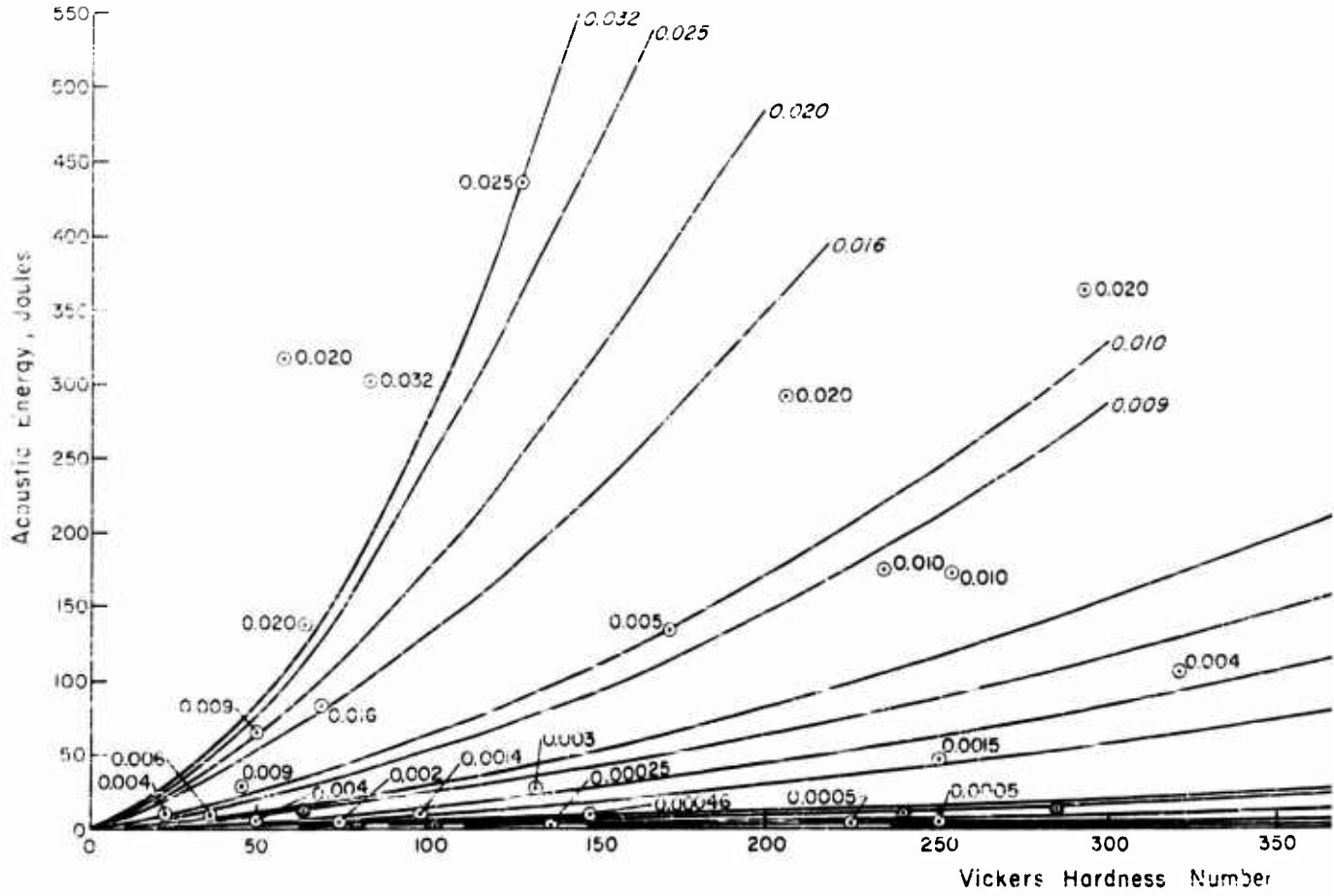
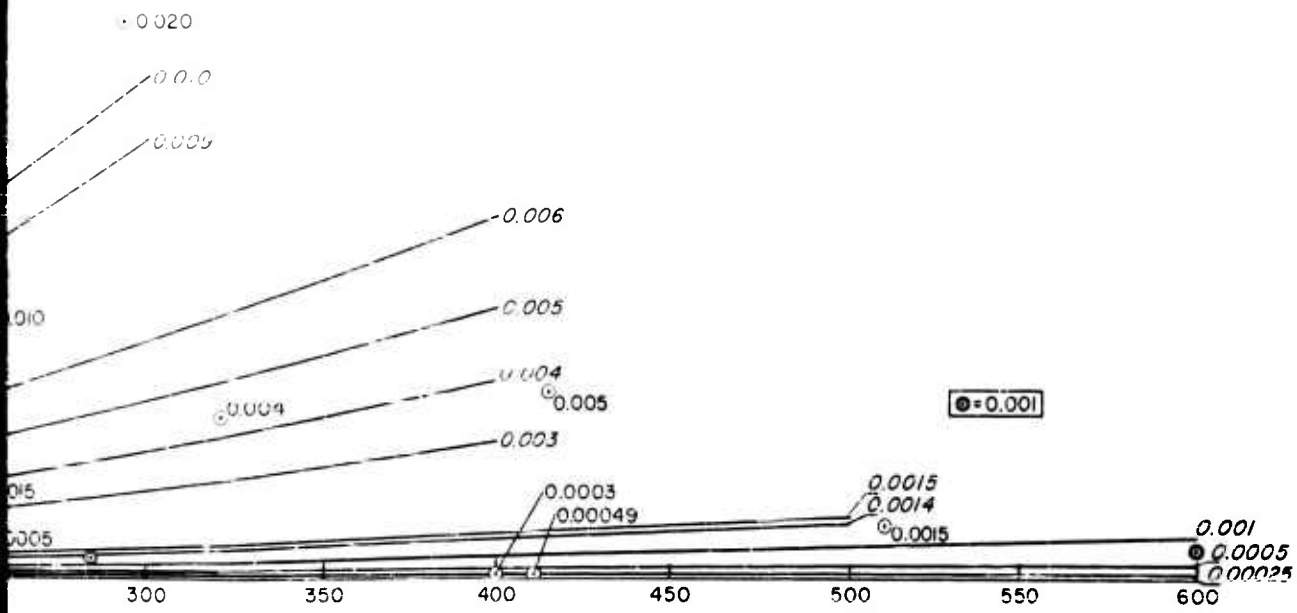


Fig. 55

Fig. 55: ACOUSTIC ENERGY REQUIRED TO WELD AS A FU
VICKERS HARDNESS WITH PARAMETERS OF MATE

Curves represent calculated data; points were experi

2



ickers Hardness Number

ERGY REQUIRED TO WELD AS A FUNCTION OF
DNESS WITH PARAMETERS OF MATERIAL THICKNESS

ted data; points were experimentally determined.

However, previously under approximated MEC conditions it was noted that each of the several materials investigated was transiently heated to between 35 and 50% of its absolute melting temperature. It is well known that during high-temperature deformation the processes of yielding, work hardening, and recovery are related to the fraction of the absolute melting temperature at which they occur.

Thus, one can normalize high-temperature deformation between various materials by comparing their properties at similar fractions of their absolute melting point.

For example, when one compares the rates of recovery of copper and aluminum as evidenced by steady-state creep behavior at temperatures approximately one-half of their absolute melting temperatures (41,42,43) their steady state creep rates are due to the absorption of vacancies by dislocation climb at dislocation lines.

In the ultrasonic welding process where the deformation accompanying the ultrasonic weldment apparently occurs in all materials investigated at similar fractions of their absolute melting temperatures, the deformation in each material should be closely akin.

Implicit in the acoustic energy equation is the assumption that a room-temperature measurement of the Vickers microindentation hardness is indicative of the material's resistance to high-temperature deformation.

This hardness parameter should be comparable, since the ultrasonic deformation occurs at similar fractions of the absolute melting temperature, and the usefulness of the equation is that it shows that such a room-temperature measurement is a good indication of the behavior of material at the welding temperature which is 30 to 50% of the absolute melting temperature.

Thus, Eq (13) might, on theoretical grounds, be multiplied by the actual transient temperature achieved during welding divided by the absolute melting temperature of the material.

Since this ratio of transient temperature to melting temperature is approximately a constant for all the materials investigated, it, too, is probably incorporated in the constant K in Eq (13). The use of the hardness parameters, therefore, appears to be justified on a reasonably fundamental basis.

2. Thickness

The significance of the parameter "t" in Eq (13) should be considered. As noted previously, as the weld material thickness increases, so does the weld bond area increase. The relation between material

thickness and weld-bond area is approximately linear, especially in the heavy materials. Thus, weld-bond area could be just as correctly used as material thickness for the variable in this energy equation. If area is considered, therefore, it is obvious that as the energy over the weld area is distributed across increasingly large weld areas, the total energy must, therefore, increase as some function of the bond area. Here, again, the parameter used in the equation is reasonable.

If great fractions of the energy were absorbed in the bulk metal rather than at the interface, the application of ultrasonic welding to thicker materials could become increasingly impractical due to the large amount of ultrasonic energy required. An interesting conclusion that may be reached from such an interpretation of material thickness, however, is that, for the heavier gages, as the weldment sheet thickness is increased, a major portion of the ultrasonic energy delivered to the work pieces is absorbed at the weld interface and not in the bulk material being welded. This conclusion becomes important in the application of ultrasonic welding to considerably thicker sheet materials.

If the weld bond area may be reduced or even restrained as material thickness increases, it will be possible to weld very thick sheet material ultrasonically. The absorption of ultrasonic energy discretely at the interface is apparently dictated by the transient increase in temperature produced at the weld interface with the resulting relaxation of the elastic constants of the material at the interface and the decreasing resistance to plastic deformation at the interface.

For further confirmation of the validity of the equation and the sheet thickness range over which it might be expected to apply, the predicted maximum thickness for any material of a given hardness as determined from the acoustical power equation, was satisfactorily compared with the thickness that has been consistently welded at a given power level.

In view of these theoretical and experimental studies, hardness and thickness may be used as reasonable parameters to consider the weldability of materials. As a first approximation, the level of their influence varies as a 3/2 power in determining the approximate energy required to produce an ultrasonic weldment. Since other material properties not included in these two parameters almost certainly have an influence on weldability, they are probably second-order effects. A follow-up program to investigate other materials in a wider range of thickness on a higher powered but equivalent welding system should serve to extend these conclusions. It should be possible to discover how the value of the proportionality constant K varies, if it does, with other parameters of the material. However, the present results constitute a significant step toward increasing the usefulness and practicability of ultrasonic welding.

3. Conclusions

The empirical relationship shown in the preceding section, is justified on a reasonably fundamental basis. It provides the first useful guide to the relation between the energy required to produce an ultrasonic weld and an easily determined set of material properties and thickness. The use of such an equation now provides a good starting point for the design of ultrasonic welding equipment as well as for the selection of machine settings to produce welds in materials without previous knowledge of ultrasonic weldability of these materials. At the present time, the use of such a parameter must be tempered by some reasonable factors to cover possibly unidentified inaccuracies (probably 15-35% of the indicated energy) until further investigation provides more precise information for its use.

V. METALLURGY AND INTERFACIAL DISTURBANCE

Microstructural observations of ultrasonic welds have been useful for the determinations of bond quality and interfacial integrity. A more general purpose of these observations is related to the understanding of the bonding mechanism. Examination of welds in various materials and material combinations helps to distinguish the interaction of events which result in the specific microstructure developed in the weld zone. It is now evident that ultrasonic bonding is associated with mutual irreversible displacements across the faying plane of the weld components. The material is usually deformed plastically in local regions of seizure which increase in size and number during the cyclic stresses accompanying ultrasonic welding. The formation and growth of these local seizures ("knots") probably is accompanied by work hardening during the early stages of seizure; however, energy dissipation during each stress reversal leads to a temperature rise, annealing, or softening of the knots, lowering the stress required for further plastic deformation.

Since only a small part of the total energy input results in motional energy at the faying surfaces, energy lost as heat may become appreciable. In situations where heat energy generation into the weld zone is rapid and conduction away from the faying surfaces is, perhaps, sluggish, the interfacial temperature increase can lead to rapid softening of the material in the weld region. In this case, the local point contact must yield to produce essentially total interface contact across the bond area. This softening, combined with the stresses imposed by the vibratory action, not uncommonly produces some expulsion of metal at the edges of the weld interface. This metal expulsion may form a narrow sheet or sliver extending in the direction of the vibratory excursions.

This extrusion of the weld metal may be associated with ultrasonically induced plasticity. This phenomenon has been demonstrated in connection with classified research (6) concerning ultrasonic extrusion of metals and with various observations associated with ultrasonic welding. These indications have recently been confirmed, at least partially, by independent foreign research (17, 25, 26, 37, and 39). There is little doubt that this phenomenon occurs during ultrasonic welding and, when associated with it, may be a significant factor in bond formation.

The behavior of surface films during the bonding process is complex and, as yet, incompletely understood. All metals and alloys (with the exception of gold) are unstable at room temperature and tend to form surface films, commonly oxides. Rupture and dispersion of surface films must occur during the bonding process to establish at least local metal-to-metal contact in the junction. Although the surface topography of the metals to be joined is uncertain, the effects of surface films and topography should be of importance in initiating the bond.

In Section III it has been shown that the minimum energy requirements for welding may be correlated with some of the mechanical properties of the metals to be ultrasonically welded. This indicates that the welding conditions at this MEC are determined by a combination of factors: the metals to be bonded, their surface topography, the type and character of surface films which may be present, the heat generated at the weldment interface, and the rate of heat dissipation away from that interface. Study of the energetics of the response of the faying surfaces to the weld conditions, however, yields little insight into the manner in which the bonding is achieved.

The characteristic microstructure developed during ultrasonic welding depends upon the response of the material properties of both the metals to be bonded and their surface films to the combination of stress and temperature imposed by the welding conditions. A study of these microstructures, therefore, may indicate the role of the welding conditions in the production of ultrasonic welds.

A. Optical Studies

1. Bond Formation

Evidence has been presented which indicates that the zone of maximum interfacial disturbance in an ultrasonic weld consists of an annulus within which there is a less completely bonded central island. It is also indicated that this annular bond zone corresponds to the ring-like area shown by photoelastic analysis to be the zone of maximum interfacial shear, wherein local slip is postulated to produce bonding.

Further consideration has been given to the shape and time-rate of growth of this annular bond zone. Two materials -- 2014-T6 aluminum and 302 stainless steel -- were studied; a series of facing coupons were placed in a standard welding array under the clamping force normally associated with the material and gage.

In order to note the marking under a very few vibratory cycles well below the lower limit of the welding machine timer, a few specimens were prepared with the aluminum alloy by tapping the sonotrode lightly with a hammer. Figure 56 illustrates the effects obtained with the aluminum wherein Fig. 56A is the pattern obtained with two hammer taps and Fig. 56B with five hammer taps. It is apparent from the specimens in Fig. 56C-G, including the ultrasonic specimen made at 0.03 sec (Fig. 56C), during initiation and formation up to 1.0 sec (the point of reasonable weld strength), that a weld does not grow very much in size, but rather the quality of the bond is increased within the approximate area of the initial bond envelope. The bond envelope area in aluminum does not grow extensively until excessive deformation occurs, and that this is associated with excessive welding time, or excessive power, or both.

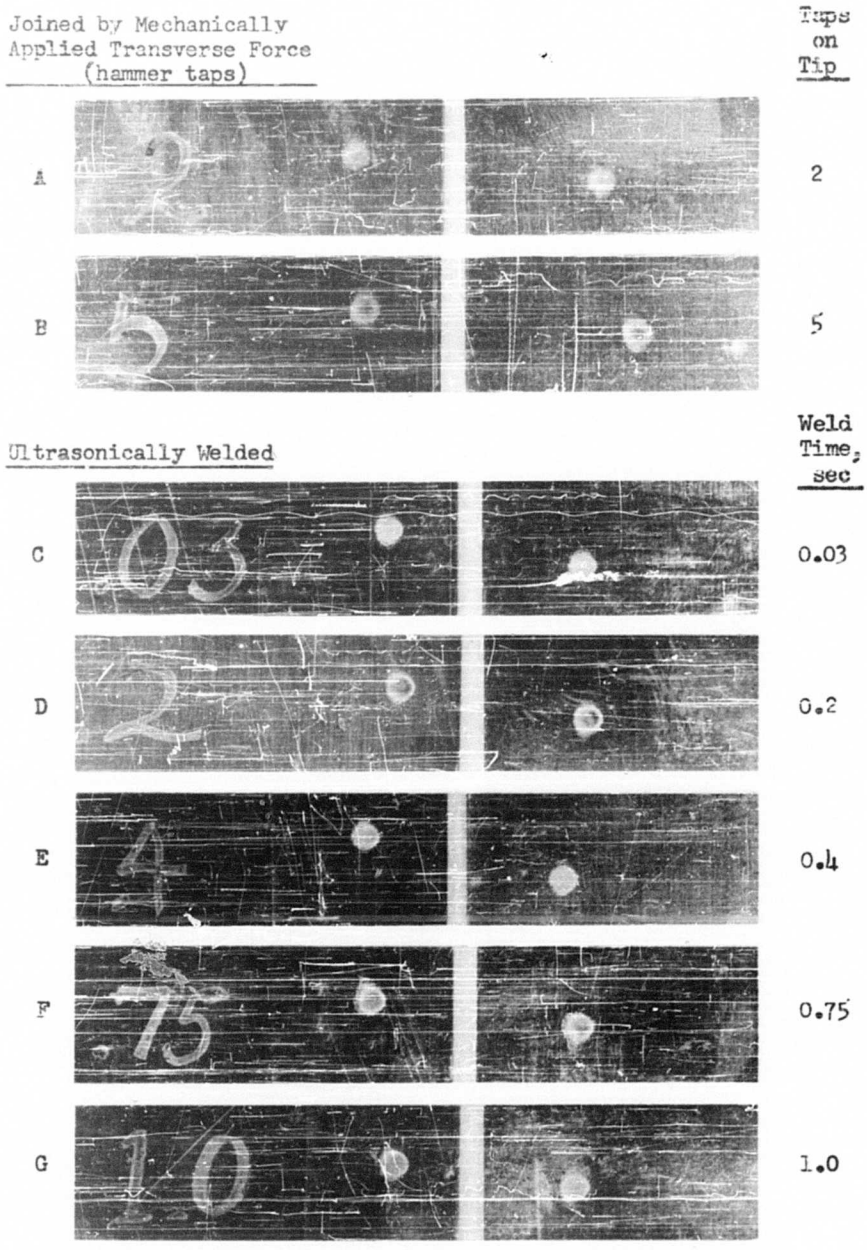
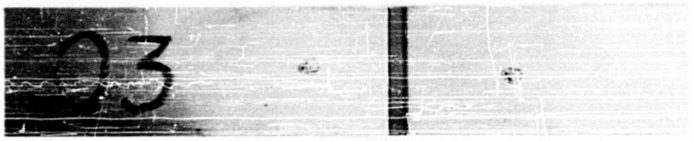


Fig. 56: SAMPLE WELDS BETWEEN STRIPS OF 2014-T6 ALUMINUM ALLOY

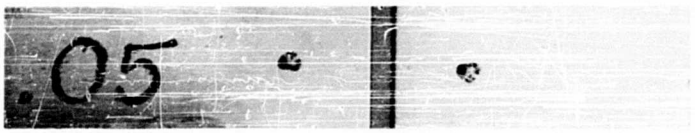
A-B: Welds resulting from simple hand-applied force (hammer taps)
C-G: Welds resulting from application of ultrasonic energy

The sequence of illustrations of Fig. 56, starting with a few taps of a hammer to obtain an initial mark and proceeding upwards in ultrasonic excitation to a time of 1.0 sec when the weld strength approaches 500 lb, demonstrates graphically that the actual bond area does not increase greatly, and that, therefore, the weld must proceed by improving the bond quality.

In order to further confirm the observation of annular formation, several coupons of a harder material, Type 302 stainless steel, were similarly exposed. In Fig. 57, a less sharply defined, but clearly evident annular zone of fretting, and a less well-bonded central island are evident. It, therefore, appears that, in two different materials, which exemplify a broad range of weldability, the weld zone is initiated as an annulus that corresponds to the zones of maximum interfacial shear observed by photoelastic analysis.



A: 0.03-sec Weld Time



B: 0.05-sec Weld Time

Fig. 57: SAMPLE WELDS BETWEEN STRIPS OF TYPE 302 STAINLESS STEEL

2. Weld Microstructures in Materials of High Thermal Conductivity

During the ultrasonic welding of materials with high-thermal conductivity, the heat generated at the faying surfaces is rapidly conducted away from this interface. This type of material, of which copper and aluminum have been investigated most thoroughly, is characterized by a bond interface which displays local regions of surface film dispersion and metal contact. When the interfacial temperature during welding is high, extensive deformation and recrystallization occur. Surface films may become dispersed within the metal or remain in fragments along the interface. The degree of interfacial deformation and seizing is variable and depends upon welding machine settings, tip geometry, and material properties.

Spot-type bonds generally display greatest deformation around the periphery of the spot; in some cases the center of the contact zone may remain unbonded. These microstructural configurations are illustrated in the series of photomicrographs of welds in 0.020-in. 1100-H18 aluminum shown in Fig. 58. The specimens were made at welding conditions along the threshold welding curve for this material and temper (Section III). The specimen (in Fig. 58A) exhibits a bond line with intermittent dispersion of the interface oxide film accompanied by negligible deformation or interpenetration of the oxide on each side of the interface. More extensive regions of oxide dispersion accompanied by interpenetration of the faying surfaces are shown by the specimen in Fig. 58B. The specimen illustrated in Fig. 58C, shows how deformation has permitted large areas of structural continuity to be established between the weld members.

3. Welds in Materials of Low Thermal Conductivity

When rapid heat conduction away from the interface cannot occur, the weld-zone temperature and the volume of heat-affected metal increases. In various instances the complete volume of material between the welding sonotrodes may achieve a uniformly high temperature, with no indication that local melting has occurred. This resultant temperature may initiate reactions such as recrystallization, phase transformation, precipitation, and diffusion, all of which are readily identified by microscopic examination. Figure 59 is the microstructure of an ultrasonic weld in 0.020-in. "A" nickel. Here extensive recrystallization and grain growth have occurred at the weld interface. The surface films previously present along the interface have been effectively dispersed.

Figure 60 shows the microstructure of the weld interface of another typical low-conductivity metal, 0.008-in. PH 15-7 Mo stainless steel. The temperature generated in the weld zone during ultrasonic welding was sufficient to begin transformation to the high-temperature, austenitic phase. In addition, some of the metal has been extruded from the periphery of the contact zone. The boundary between the metal, which has been transformed in the center of the weld region, and the surrounding untransformed metal, delineated by the compositional response to the etching solution, indicates the thermal gradient produced during ultrasonic welding.

4. Weld Between Dissimilar Materials

The microstructure of ultrasonic weldments produced between dissimilar metals not only are affected by the temperature generated at the weld interface and the high degree of plastic deformation but also may exhibit microstructural changes resulting from interaction between the dissimilar metals. A typical example is shown in Fig. 61, a photomicrograph of the area near the ultrasonic weld zone between Type 430 stainless steel and A-110-AT titanium alloy. The temperature generated at the

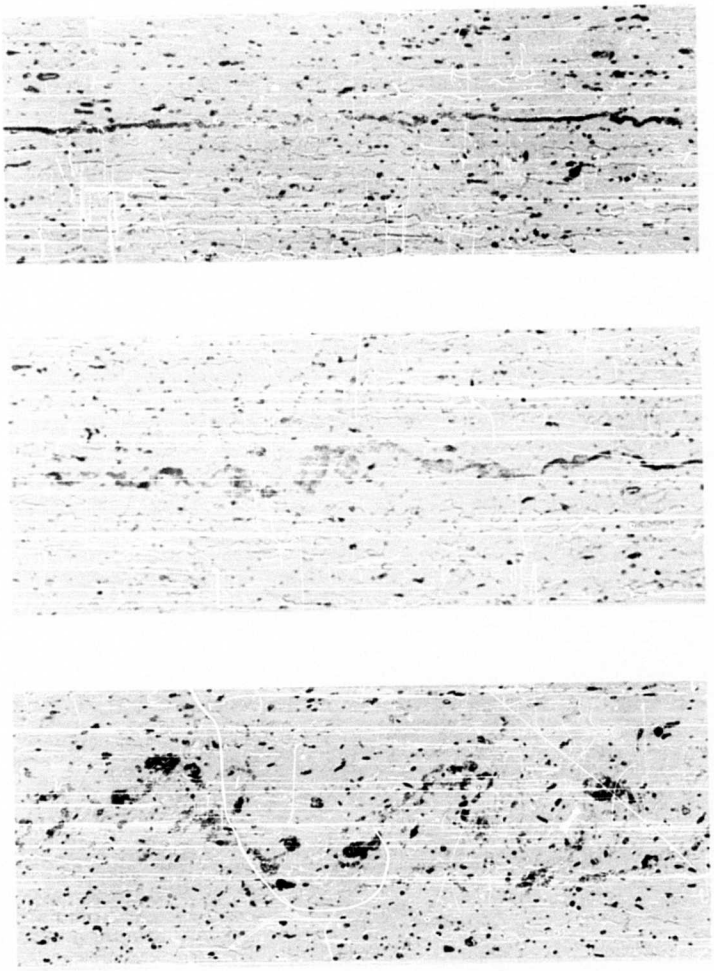


Fig. 58: ULTRASONIC WELDS IN 0.020-INCH 1100-H18 ALUMINUM ALONG THE THRESHOLD CURVE
Etchant: 0.5% HF
Magnification: 500X



Fig. 59: ULTRASONIC WELD IN 0.020-INCH "A" NICKEL
Machine Settings: 1750 w/400 lb/1.0 sec
Etchant: KCN + $NH_4S_2O_8$
Magnification: 100X



Fig. 60: ULTRASONIC WELD IN 0.008-INCH PH 15-7 MOLYBDENUM STAINLESS STEEL
Machine Settings: 1000 w/450 lb/0.15 sec
Etchant: Oxalic acid (electrolytic)
Magnification: 150X

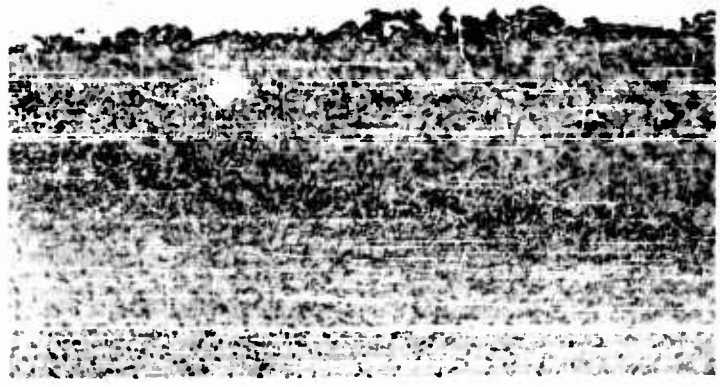


Fig. 61: PHOTOMICROGRAPH OF INTERPENETRATION OF MATING SURFACES OF 0.024-INCH 430 STAINLESS STEEL AND 0.028-INCH A-100 AT TITANIUM ALLOY--SHOWING STRUCTURAL CHANGES IN THE TITANIUM ALLOY RESULTING FROM HEAT GENERATED DURING ULTRASONIC WELDING

Etchant: HF + HNO_3
Magnification: 150X

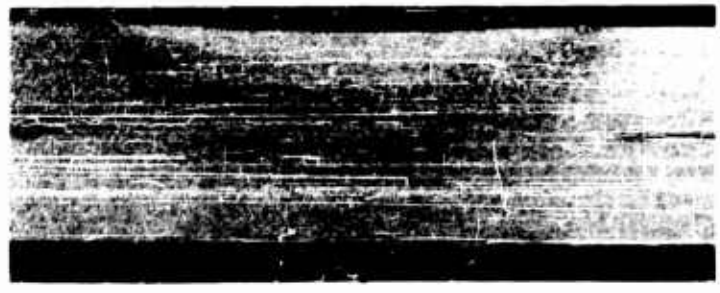


Fig. 62: ULTRASONIC WELD IN 0.060-INCH 2024-T6 ALUMINUM WITH 0.001-INCH 1100 ALUMINUM FOIL INSERT

Etchant: Keller
Magnification: 8.5X

weld interface exceeded the transformation temperature of the titanium alloy producing the acicular structure in the titanium of the weld zone. The temperature gradient away from the weld interface in the titanium alloy is again clearly delineated by the boundary between the transformed and untransformed regions in the titanium sheet. There is curvature of the transformed zone as it approaches the edge of the spot. In addition, a filmlike structure is present at the weld interface; this structure may be an intermetallic compound formed between iron and titanium.

Figure 62 shows the microstructure of an ultrasonic weld between 0.080-in. 2014-T6 aluminum sheet with a 0.01-in. 1100 aluminum foil insert. Here, the 1100 aluminum foil insert affected the rate of heat generation at the weld interface during ultrasonic welding, so that there was only a small temperature rise at the weld interface. In contrast, however, the maximum temperature increase was at the tip contact surface so that the weld interface possibly was heated by conduction through the weldment. Thus the source of heat generation through the weld zone may not be restricted to the interface, but rather heat generation at the outer surface can sometimes arise by local displacements between the work and the sonotrodes.

During the ultrasonic welding of dissimilar metals, when one or more components of the pieces to be welded is soluble in the other, diffusion of these components across the weld interface may occur. Diffusion of this type during ultrasonic welding has been observed between copper and zinc (4). A photomicrograph of an ultrasonic weld between 0.030-in. Type O-2 tool steel* and 0.030-in. Armco iron is shown in Fig. 63. Carbon is soluble in both of the alloys, but is present in higher concentration in the tool steel than in the Armco iron. The welding conditions were 4200 watts/600 lb/1.5 sec. Because of the large power input coupled with the relatively low thermal-conductivity of each of these materials, a high temperature rise might be expected at the weld interface. The concentration gradient of carbon between these two alloys in conjunction with the high temperature apparently resulted in the diffusion of carbon across the interface, as shown in Fig. 63. The question of diffusion reactions during the ultrasonic weld cycle is difficult to resolve. Since static diffusion coefficients are small, diffusion may be difficult to observe microscopically in view of the short welding intervals used. However, the influence of ultrasonics on diffusion phenomena must be considered (14). Although the literature is relatively barren on this subject a possibly accelerating effect cannot be ignored.

---

* Simmonds oil-hardening die steel.

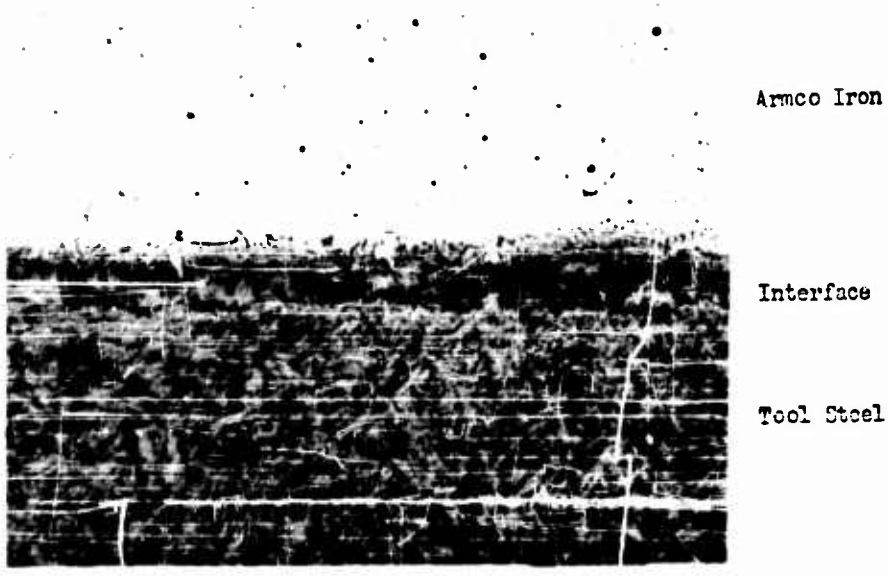


Fig. 63: PHOTOMICROGRAPH OF ULTRASONIC WELD BETWEEN 0.030-INCH AISI-TYPE 0.2 TOOL STEEL (0.90% CARBON) AND 0.030-INCH ARMCO IRON--ILLUSTRATING THE DIFFUSION OF CARBON INTO THE IRON

Etchant: Picral
Magnification: 1000X

A. Ultrasonically Developed Texture

Among the metallographic changes attributed to ultrasonic welding is a unique structure developed by the vibratory stress acting on the heated metal during ultrasonic welding. The grain morphology of the material is such as to present a block-like appearance.

Sections of welds in a Ti-8 Mn alloy and Type 302 stainless steel were examined to determine whether the block structure is dependent upon orientation, that is, whether the structure is dependent upon the vibratory motion of the welding tip and/or the rolling direction of the sheet. Figures 64 and 65 show this orientation effect. It appears that the rolling direction of the sheet has no effect on the development of the texture; however, the pattern is different in sections longitudinal and transverse to the direction of vibratory motion. In the longitudinal sections, the grain boundaries tend to be aligned in directions parallel and normal to the interface. The orientation of the boundaries in sections normal to the vibratory direction are more random.

This block structure has been observed in the face-centered-cubic alloys: K-Monel, Type 302 stainless steel, 2024 aluminum, Inconel X, L-605, Inco 702, and the body-centered-cubic phase of Ti-8 Mn alloy. Polonis and Par (35) have observed a block-type pattern in retained Beta phase of Ti-Ni alloys. They compare the structure to a similar one obtained by Barrett (15) in copper-silicon alloys which was interpreted as clusters of faults separated by relatively perfect crystal layers. Internal strain from quenching was proposed as an explanation of the origin of the structure.

B. Examination of Weldments by Autoradiographic Techniques

In ultrasonic welding surface-barrier films and scales are significant. Since bonding is initiated at the faying surfaces, interference by foreign materials may have an observable effect on the formation and characteristics of the bond.

Previous experience has demonstrated that surface films can play a role in the bonding process. Some materials develop greater bond strengths when welded with the mill-finish coating intact. Chemical cleaning procedures, which effectively remove the film, may decrease the bond strength (7), but this effect is obscure since, in addition, this chemical cleaning also affects surface roughness. The microstructural features of the weld interfaces of the mill-finish and chemically cleaned materials are characteristically different. Extensive deformation, film fragmentation and dispersion, and interpenetration of the faying surfaces occur when the mill-finish materials are ultrasonically welded. Chemically prepared surfaces, on the other hand, result in a bond with negligible interpenetration. The bond line is intermittently interrupted by breaks along its length, but the surface layer undergoes little dispersion.

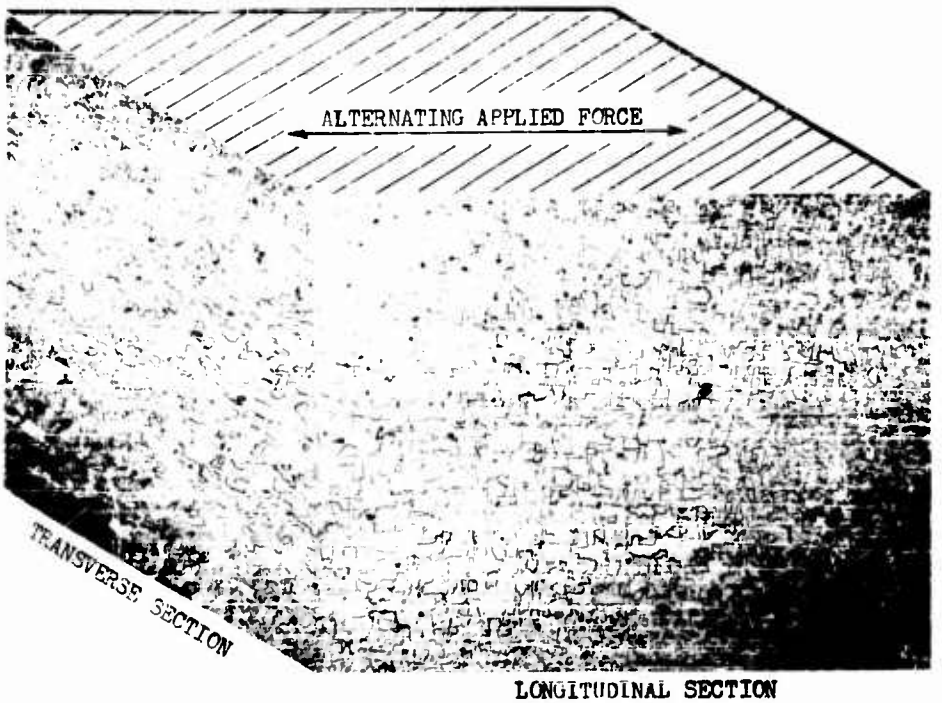


Fig. 64: PHOTOMICROGRAPHS OF 0.020-INCH THICKNESS OF TITANIUM-8 MANGANESE ALLOY SECTIONS TAKEN TRANSVERSELY AND LONGITUDINALLY TO THE VIBRATORY MOTION OCCURRING DURING ULTRASONIC WELDING--SHOWING BLOCK-LIKE ORIENTATION EFFECT

Etchant: HF + HNO_3
Magnification: 100X

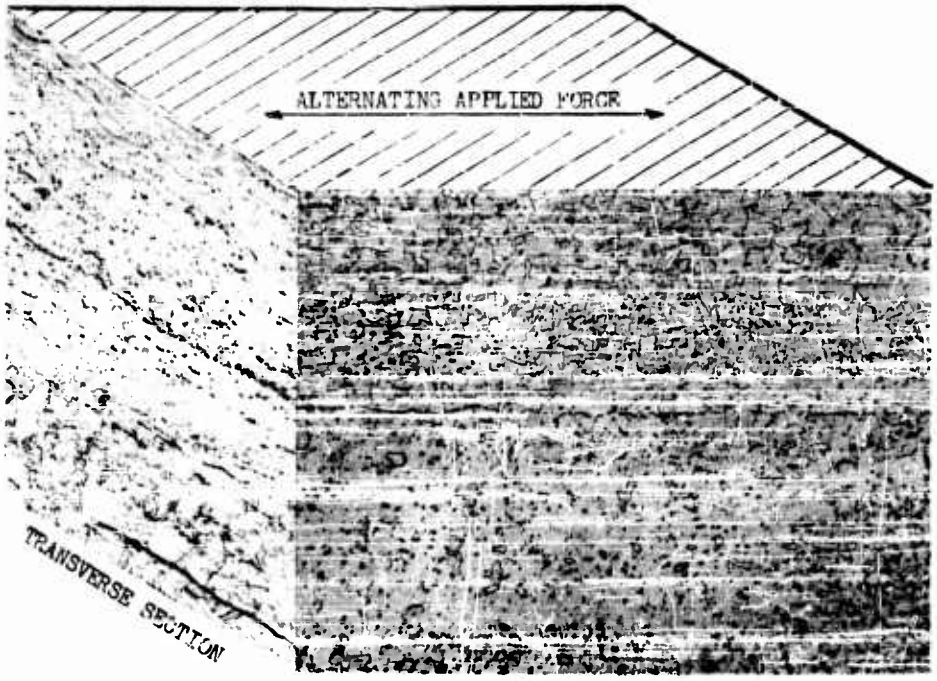


Fig. 65: PHOTOMICROGRAPHS OF 0.025-INCH THICKNESSES OF 302 STAINLESS STEEL TAKEN TRANSVERSELY AND LONGITUDINALLY TO THE VIBRATORY MOTION OCCURRING DURING ULTRASONIC WELDING--SHOWING BLOCK-LIKE ORIENTATION EFFECT

Etchant: Oxalic Acid
Magnification: 100X

The heat treated aluminum alloys with oxide films formed at elevated temperatures are generally more difficult to bond without prior removal of the adherent scale. In this case, somewhat more effective surface preparation is achieved by mechanical methods than by chemical treatments. The reasons for difficulty in bonding through this heat-treatment scale are not fully understood, but probably both the thickness and the composition of the oxide are contributing factors.

Figure 66 illustrates that bonding can be achieved through heat-treatment scales. These photomicrographs were made of welds in equivalent gages of Inconel X, (a) with the oxide intact and (b) with the oxide removed by chemical de-oxidation prior to ultrasonic welding. The differences in the microstructural characteristics are evident. In this instance, unlike aluminum, the surface scale is loosely adherent and supported by a hard substrate. It is likely that removal of the scale before welding induces less energy generation at the interface, whereas the presence of the scale localizes energy generation and degradation about the interface.

In an effort to consider the effect on weldability and the eventual distribution of surface films after completion of the weld cycle, an experiment was designed in which anodized coatings were used as the surface coating. This material was chosen for several reasons: (a) aluminum and aluminum alloys have been extensively investigated in previous Aeroprojects work; (b) anodized coatings are readily available in several thicknesses; (c) anodized coatings on aluminum can be produced which are porous and, therefore, amenable to radioactive tracer impregnation; and (d) welding parameters for aluminum alloys are within the capacity of the instrumented 2-kw research welder.

The alloy investigated was an aluminum alloy sheet of commercial purity containing 0.11 w/o iron and 0.06 w/o silicon. The specimens were first chemically polished in R5 Bright Dip* and then anodically coated with a 15% sulphuric acid electrolyte at 70°F at an imposed potential of 9-10 volts dc. After anodizing, the coatings were left unsealed and were, therefore, porous.

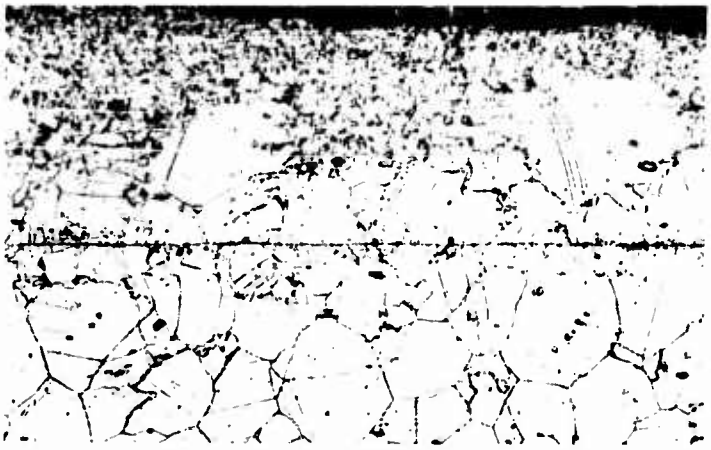
The preparation of the anodized sheet was carried out at the Finishes Division of the Alcoa Research Laboratories. Panels 12 in. x 12 in. x 0.025 in. with oxide coating thicknesses of 500, 1000, and 3000 Å were supplied for investigation. The panels were cut into test coupons 3/4 in. x 3/4 in. for the tracer study and into 3/4 in. x 3 in. strips for weld strength determination.

---

* Alcoa proprietary chemical finish.



A. Bonded Without Removing Heat-Treatment Scale



B. Chemically Deoxidized

Fig. 66: ULTRASONIC WELDS IN 0.012-INCH INCONEL X IN THE SOLUTION-HEAT-TREATED CONDITION

Etchant: Oxalic Acid (Electrolytic)
Magnification: 150X

In order to determine the effect of oxide thickness on the weld strength of ultrasonically welded aluminum sheet, the test strips described were ultrasonically welded with various combinations of ultrasonic power and clamping force. The tensile-shear strength of each of these welds was then determined. The results obtained are shown in Table X. Statistical evaluation of these results (Tables X and XI, p. 76), indicate that both the oxide coating thickness and the welding conditions have a significant effect on weld strength. It is of interest that the strongest weld was produced in the aluminum sheet with the thickest oxide film coating. The standard deviation of the tensile-shear strength measurements for the entire series of experiments is 10.75 lb/spot, a measure of the uniformity of the ultrasonic welding.

The 3/4-in. x 3/4-in. test coupons, described previously were impregnated with a radioactive tracer by treatment in a nickel acetate solution containing a small quantity of Ni^{63}. Good absorption of the tracer was obtained within 1/2 hr at 200°F, and the test coupons were then ultrasonically welded. The surface treatment appeared to have an adverse influence on the weldability of the test pieces. Several specimens failed to bond under the welding conditions used, while control specimens, which were treated only in boiling distilled water to seal the film, bonded without difficulty.

Subsequent metallographic examination of the weld region of the radioactive samples showed that bonding was achieved in the peripheral region of the weld spot as is not uncommon. The central portion of the weld area contained unbonded sections. The bonding in the peripheral region was quite adequate to carry out the autoradiographic investigation of the interface.

All specimens were then sectioned normal to the weld interface for metallographic examination. The Kodak permeable-base autoradiographic stripping film was used in the preparation of the specimens, an experimental technique described previously (4). Exposures were carried out for 120 hr for each oxide thickness (500, 1000, and 3000 Å units), and all specimens were then processed simultaneously to reduce processing variables. This technique permitted optical examination of the autoradiographic replicas in situ on the specimen surface.

The autoradiographic study revealed several features characteristic of the weld interface. The autoradiographic image delineated the oxide film dispersion along the weld interface and distinguished discrete oxide particles, or agglomerates, from small voids which are produced in the regions of high plastic deformation. These voids are

difficult to distinguish under bright-field optical illumination but usually can be identified by polarized-light methods. Voids seemingly occurred in those regions where the fragmented oxide particles "bridge" or restrain the material from making contact across the interface.

Close examination of the autoradiographs revealed that some material identified as oxide in the microstructure could not be observed on the autoradiographic replica. Since the aluminum oxide generated during the bonding process would not be radioactive, it can account for these nonradioactive particles. The photomicrographs, shown in Fig. 67, are illustrative of the observations described: A, the structure along the interface in a region near the bond periphery with accompanying artifact shadows resulting from focusing through the photographic film and, B, the autoradiograph. The microstructure in A and the radiographic image in B are not completely in register; the offset was caused by photographic film slippage during development. In Fig. 67A, the large oxide patch on the left appears as a continuous dark area in the microstructure, but in the autoradiograph in Fig. 67B, detail within this area is resolved. Polarized-light examination shows that the light areas within these patches are the microvoids, previously described. The dark oxide agglomerate on the right of Fig. 67A, has no counterpart in Fig. 67B. Since the autoradiograph cannot distinguish between nonradioactive oxide and a void area, a region such as this was not positively identified. However, failure to identify this area as a void, either with bright field or polarized illumination, suggests that the area is aluminum oxide generated during bonding.

This technique is, of course, limited by the inherent resolution provided by the film emulsion and the presence of background scatter radiation. Therefore, very high resolution cannot be provided. The results of the experiment indicate that although the method does produce valuable results, its application to the study of ultrasonic welding is restricted by this inherent lack of high resolution.

C. Characterization of Weldments by Electron Microscopy

Optical microscopy has been effectively utilized to characterize ultrasonic weldments. Metallurgical phenomena, such as recrystallization diffusion and cold-work effects, have been readily observed and catalogued. Although such effects are discernible with the optical microscope, their differentiation is difficult and sometimes impossible in monometallic weld systems.

The use of electron microscopy is necessary to augment the study of the interfacial mechanics and metallurgy of ultrasonic weldments. With the increased magnification and resolving power inherent in electron microscopy, more weld interface detail can be interpreted and correlated



A. Photomicrograph of Structure



B. Autoradiograph

Fig. 67: INTERFACIAL AREA OF ULTRASONIC WELD IN ANODIZED (3000 Å) ALUMINUM
Etchant: 0.5% HF
Magnification: 500X

with the previously accumulated knowledge of ultrasonic welding. Such a study provides an insight into the mechanism of ultrasonic welding.

1. Experimental Technique

Three metals -- Armco iron, 1100 H14 aluminum, and commercially pure copper -- were utilized in the electron microscopic studies. Sheets of these metals 0.032 in. thick were welded ultrasonically under conditions determined from the established welding threshold curves. The machine settings used are given in Table XII.

Table XII

MACHINE SETTINGS USED FOR WELDING SAMPLES EXAMINED BY ELECTRON MICROSCOPY

Material	Gage, in.	Surface Preparation	Machine Settings		
			watts	lb	sec
1100-H14 Aluminum	0.032	Degreased	1300	400	1.5
Armco Iron	0.032	Abraded	2000	250	1.5
CP Copper	0.032	None	1700	600	1

Two samples of each material were prepared in this manner. One of these samples was sectioned normal to the weldment and then polished and etched by standard metallographic techniques. The other sample of each material, after welding, was notched across the weld tab through the weld zone, cooled to -40°F, and then fractured. Positive film replicas of both the polished and etched end of the fracture surface for each material were then prepared. A schematic representation of the positive replica technique used in this electron microscope study is shown in Fig. 68. First, a thick plastic surface replica was formed on the specimen surface. This plastic replica was subsequently removed from the sample by gentle tapping. A positive replica was then prepared by vapor deposition of a thin film of silica normal to the plastic surface. After separation from the plastic, the positive silica replica was shadowed with chromium. These replicas were then examined using the electron microscope.

D. Results

1. Armco Iron

Optical photomicrographs of the weld zone between two ultrasonically welded sheets of 0.032-in. Armco iron are shown in Fig. 69A

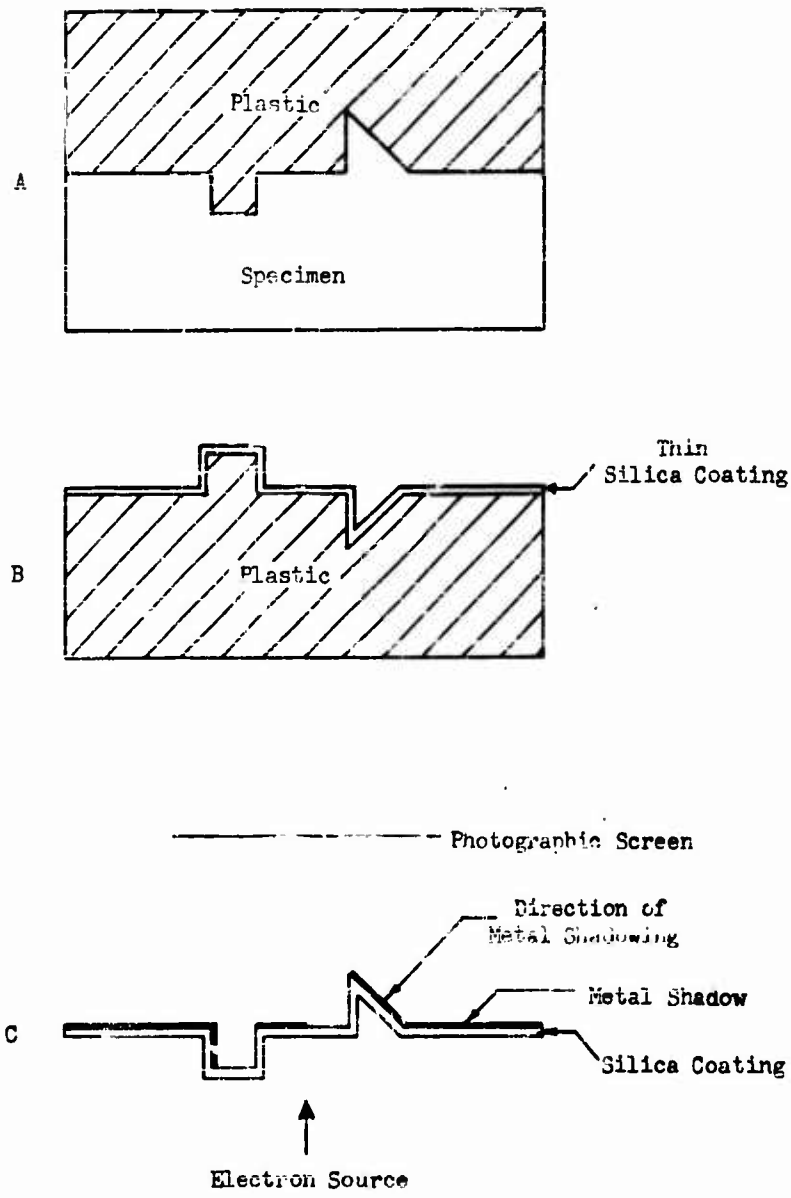


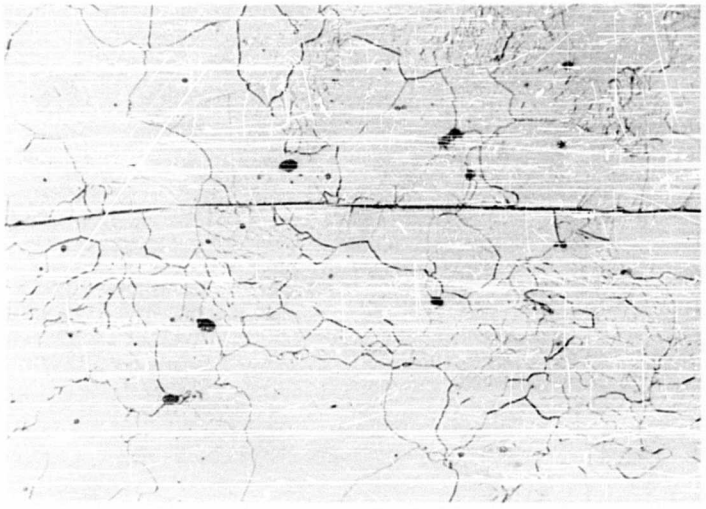
Fig. 68: SCHEMATIC REPRESENTATION OF CROSS SECTION OF POSITIVE SHADOWED REPLICA

and B. The weld interface is shown in the photomicrograph of Fig. 69A as an unbroken line. Bonding apparently did not occur in this area. The subgrain structure seen in the area about the weld interface indicates that, although seizure did not occur, plastic deformation accompanied by heat generation did. This type of structure is not typical of the entire weld interface. The photomicrograph shown in Fig. 69B depicts the weld interface near the periphery of the bond spot. Here seizure occurred with accompanying interfacial deformation and surface film dispersion. Extensive recrystallization is also evident. In addition, grain growth had proceeded in several areas establishing structural continuity between the weld members. Some subgrain development can be observed adjacent to the interfacial region.

Electron micrographs of areas equivalent to those shown optically in Fig. 69A and B were made. These electron micrographs are shown in Fig. 70, 71, 72, and 73. In Fig. 70 the weld interface runs obliquely across the micrograph. The microstructure revealed is quite different for the metal on one side of the interface than the microstructure for the other side. The substructure on the left side, is rather random in nature with little evidence of grain boundary shearing. The substructure on the right side of the weld interface, on the other hand, consists of elongated subgrains, evidently the result of considerable subgrain boundary shear. Void formation is apparent along some of these subboundaries, particularly at triple point intersections of three subgrains. Voids are also present in the interface between the two weld members. Fine particles of the surface film previously present on the weld members are dispersed in the weld zone structure near the interface.

Figure 71 is an electron micrograph taken at the weld zone showing the structure across the weld interface. In addition to the microstructural features which were revealed in Fig. 70, considerable etchant pitting is also evident. Here the subgrain structure is not well developed. Evidently little plastic deformation and heat generation occurred at this portion of the weld interface. Some particles of the original surface film on the weld member remain at the weld interface. Others are coarsely dispersed in the region about the weld interface.

In Fig. 72 the interpenetration of one weld member into the other, with apparently little degradation of the interface film, is shown. Rather coarsely dispersed interface film particles are seen in the region about the weld interface. In Fig. 73 the highly deformed region near the weld interface is illustrated. Here extensive subgrain structure has been developed with some evidence of grain boundary shearing. Incipient void formation is found at some of the subgrain boundaries, but it is not well developed. In addition, the surface film originally present on the weld members has been finely dispersed throughout the weld zone structure.



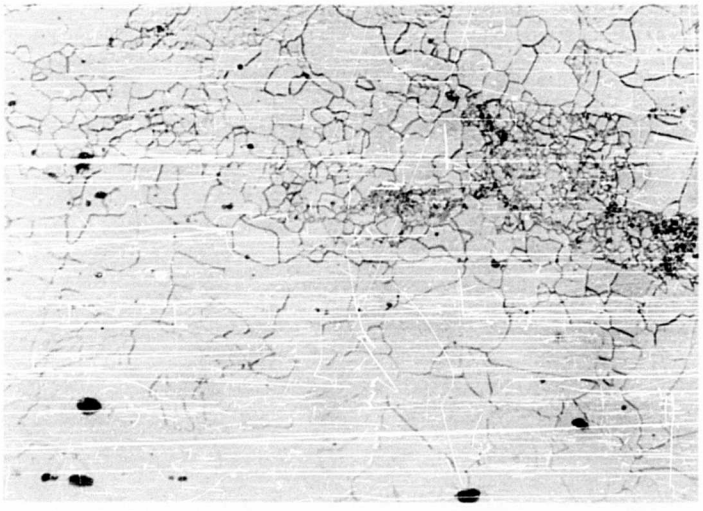


Fig. 69: OPTICAL PHOTOMICROGRAPHS OF INTERFACIAL AREAS IN ULTRASONIC WELD BETWEEN TWO SHEETS OF 0.032 INCH ARMCO INGOT IRON

Etchant: 2% Nital
Magnification: 500X

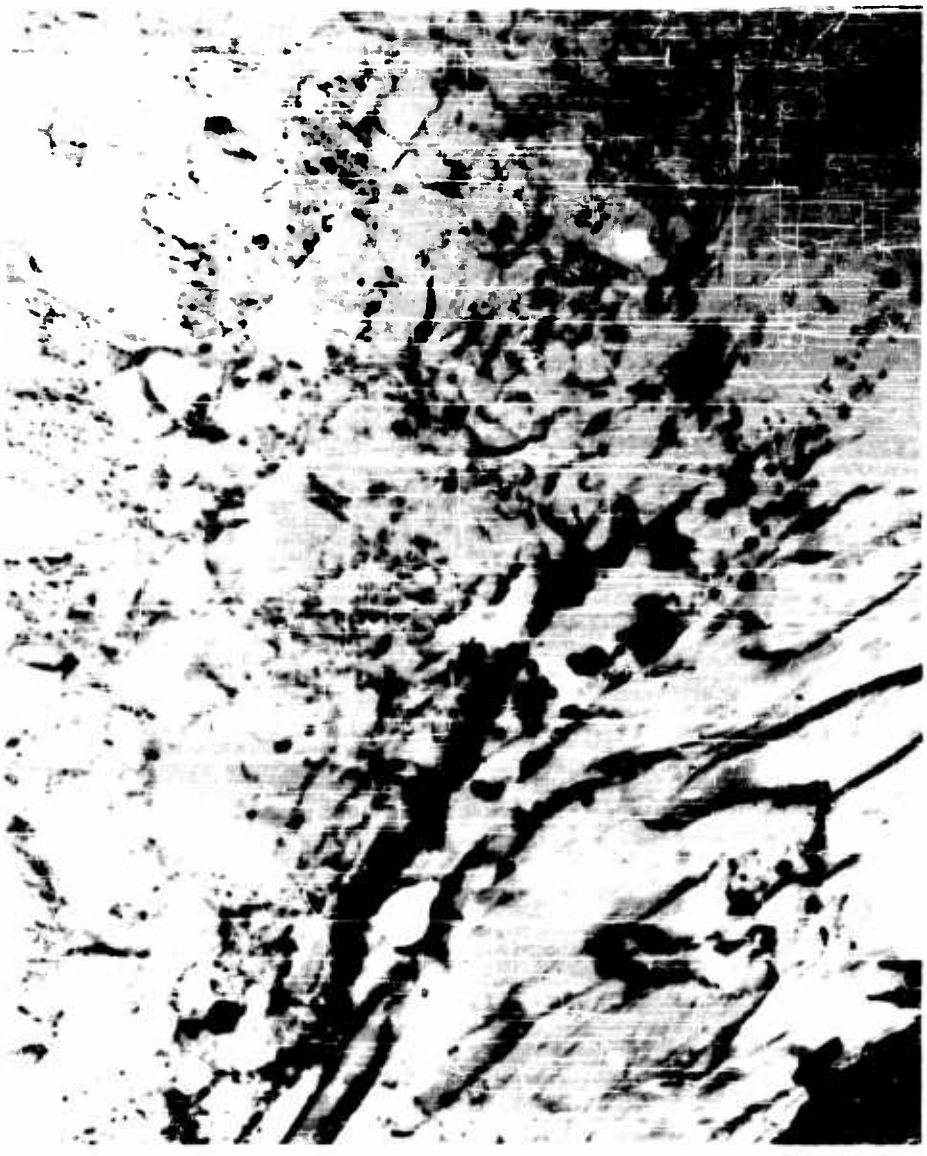


Fig. 70: ELECTRON MICROGRAPH OF POLISHED AND ETCHED IRON SHOWING CONSIDERABLE SUBGRAIN BOUNDARY SHEAR

Magnification: 20,000X



Fig. 71: ELECTRON MICROGRAPH OF POLISHED AND ETCHED IRON SHOWING PITTING FROM ETCHANT

Magnification: 20,000X



Fig. 72: ELECTRON MICROGRAPH OF POLISHED AND ETCHED IRON SHOWING CONTINUITY OF INTERFACE FILM

Magnification: 20,000X



Fig. 73: ELECTRON MICROGRAPH OF POLISHED AND ETCHED IRON SHOWING SUBGRAIN BOUNDARIES NEAR THE WELD ZONE

Magnification: 20,000X

2. Copper of Commercial Purity

Figure 74 is an optical photomicrograph of the weld zone between two sheets of 0.032-in. copper of commercial purity which have been bonded by ultrasonic welding. The weld zone runs horizontally across the photomicrograph. Extensive recrystallization with accompanying grain refinement has occurred throughout the region in and about the weld interface. The copper oxide surface film originally present on the weld members has been finely dispersed in the weld zone adjacent to the interface.



Fig. 74: OPTICAL MICROGRAPH OF WELD IN 0.032-INCH COMMERCIALLY PURE COPPER
Etchant: $NH_4OH + H_2O_2$
Magnification: 500X

Figures 75, 76, and 77 are electron micrographs taken of the weld interface, similar to that shown in Fig. 74. In Fig. 75 the weld interface runs horizontally across the electron micrograph. It is evident from this electron micrograph that pieces of the surface film originally present on the weld members have been finely dispersed in the region adjacent to the interface. The interface, itself, still contains a considerable amount of the original surface film and shows some void formation.

In Fig. 76, the weld interface again is clearly delineated showing somewhat more degradation of the original surface film with attendant dispersion of this film into the areas adjacent to the interface than is shown in Fig. 75. The electron micrograph shown in Fig. 77 indicates that, in this region of the weld interface, most of the original



Fig. 75: ELECTRON MICROGRAPH OF POLISHED AND ETCHED COPPER SHOWING FINELY DISPERSED SURFACE FILM ADJACENT TO WELD INTERFACE

Magnification: 20,000X



Fig. 76: ELECTRON MICROGRAPH OF POLISHED AND ETCHED COPPER SHOWING DEGRADATION OF ORIGINAL WELD INTERFACE FILM

Magnification: 20,000X



Fig. 77: ELECTRON MICROGRAPH OF POLISHED AND ETCHED COPPER SHOWING EFFECTIVE DISPERSION OF WELD INTERFACE FILM

Magnification: 20,000X

surface film present on the original weld members has been effectively dispersed into the region surrounding the interface. This produced a finely dispersed second phase within the copper matrix. The dark particles present in the micrograph are probably copper oxide particles from the sample retained on the surface replica.

Figure 78 is an electron micrograph of the surface of one of the weld members after the weld had been broken by peeling one weld member away from the other. The electron micrograph shows the peeled area through the original weld zone. The direction of peeling was parallel to the vertical axis of the electron micrograph. The surface shown is typical of that observed for materials which have failed by ductile fracture.

Figures 79, 80, 81, and 82 are electron micrographs taken of the fracture surface produced by breaking the weldment normal to the weld interface. In Fig. 79, the fracture surface of the weld interface is shown. For the most part, this fracture occurred ductilely, but some cleavage facets are evident in the electron micrograph. Figure 80 shows an electron micrograph of the fracture surface near the weld interface. Here extensive plastic deformation occurred prior to fracture, as evidenced by both the fine slip traces and the cusp and void formation attendant to these. In Fig. 81 an electron micrograph showing the fracture surface through the weld zone, near the periphery of the weld, indicates that in this region extensive plastic deformation has occurred during failure. In contrast to this, Fig. 82 is an electron micrograph of the fracture surface at the weld interface near the center of the weld zone. This demonstrates the inherently lower ductility in this area during fracture as compared with the previous electron micrograph.

3. Aluminum of Commercial Purity

Figure 83A and B are optical photomicrographs of the ultrasonic weld interface between two sheets of 0.032-in. 1100-H14 aluminum. The interface runs horizontally across each photomicrograph. Degradation of the original oxide surface film is apparent with attendant dispersion of the oxide within the aluminum near the weld interface. In addition, extensive plastic deformation has occurred; this produced interpenetration of the weld metal on one side of the interface into the metal on the other side. Subgrain formation near the weld zone is also shown.

Figures 84 and 85 are electron micrographs of the ultrasonically welded aluminum samples at the weld zone. In Fig. 84 some void formation is apparent at the weld interface. In addition, degradation of the original aluminum oxide surface film on the weld members has occurred, resulting in a finely dispersed second phase of aluminum oxide present in the aluminum near the weld interface. In Fig. 85 it is apparent that extensive plastic deformation has occurred at the weld interface, producing the oxide film degradation.



Fig. 78: ELECTRON MICROGRAPH OF COPPER PEELED SURFACE
Magnification: 20,000X



Fig. 79: ELECTRON MICROGRAPH OF COPPER SHOWING CLEAVAGE FACETS OF THE FRACTURE SURFACE OF THE WELD INTERFACE

Magnification: 20,000X



Fig. 80: ELECTRON MICROGRAPH OF COPPER SHOWING PLASTIC DEFORMATION ASSOCIATED WITH FRACTURE

Magnification: 20,000X



Fig. 81: ELECTRON MICROGRAPH OF COPPER SHOWING PLASTIC DEFORMATION WHICH OCCURRED DURING FAILURE

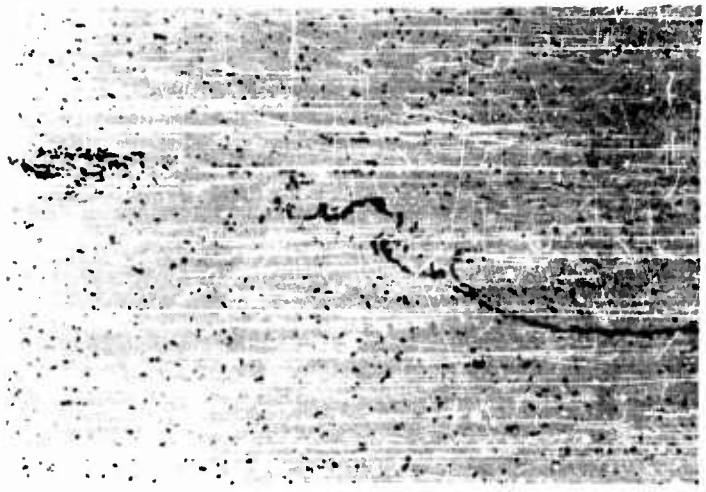
Magnification: 20,000X



Fig. 62: ELECTRON MICROGRAPH OF COPPER SHOWING LOWER DUCTILITY NEAR CENTER OF WELD ZONE

Magnification: 20,000X

A



B



Fig. 85: OPTICAL PHOTOMICROGRAPHS OF ULTRASONIC WELDS IN 0.032-INCH 1100-H14 ALUMINUM



Fig. 84: ELECTRON MICROGRAPH OF POLISHED AND ETCHED ALUMINUM SHOWING VOIDS AND DISPERSED MATERIAL AT WELD INTERFACE

Magnification: 20,000X



Fig. 85: ELECTRON MICROGRAPH OF POLISHED AND ETCHED ALUMINUM SHOWING DEGRADATION OF OXIDE FILM AT WELD INTERFACE

Magnification: 20,000X

Figures 86, 87, and 88 are electron micrographs of one surface of the aluminum weldment after the weld has been fractured by peeling one weld member away from the other. These electron micrographs illustrate the extensive plastic deformation attendant to the peeling operation. It is apparent that some of the specimen cracks have initiated at second phase particles present in the aluminum matrix. Figures 89 and 90 are electron micrographs of the fracture surface across the weld zone of this ultrasonically welded aluminum sheet. Figure 89 shows the fracture surface at the weld interface, while Fig. 90 shows the fracture surface in the weld zone near the interface. In both cases, failure was associated with extensive plastic deformation with crack propagation associated with the impurity particles and grain boundaries.



Fig. 86: ELECTRON MICROGRAPH OF THE PEELED WELD SURFACE OF ALUMINUM

Magnification: 20,000X

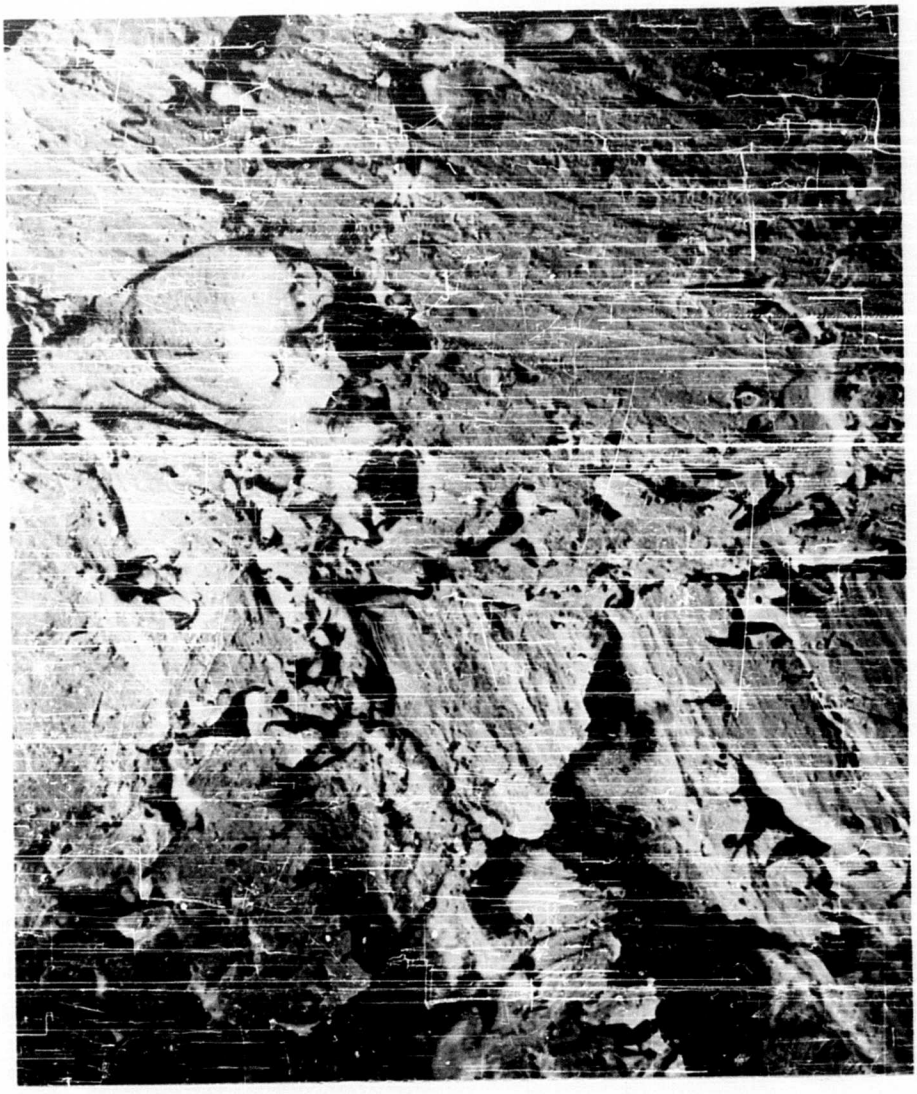


Fig. 87: ELECTRON MICROGRAPH OF THE PEELED WELD SURFACE OF ALUMINUM

Magnification: 20,000X



Fig. 88: ELECTRON MICROGRAPH OF THE PEELED WELD SURFACE OF ALUMINUM

Magnification: 20,000X



Fig. 89: ELECTRON MICROGRAPH OF FRACTURE SURFACE ACROSS WELD INTERFACE OF ALUMINUM

Magnification: 20,000X



Fig. 90: ELECTRON MICROGRAPH OF FRACTURE SURFACE NEAR THE WELD INTERFACE OF ALUMINUM

Magnification: 20,000X

VI. CONCLUSIONS

A. Photoelastic

Studies of models loaded at discrete conditions productive of ultrasonic welds between two sheets of metal show that:

1. Islands of local slip within areas of elastic strain and definitely not gross sliding, induce welding on the side of the sonotrode toward which the oscillating force acts.

> On the side away from which the oscillating force acts, the interfacial shear stress productive of welding collapses. Thus, welding is initiated first on one side and then on the other side of the powered sonotrode, and these small islands presumably run together. Hence, it is possible to produce welds overlapping each other.

2. Local slip clearly leads to a local temperature rise causing local softening of the material.

3. Welding is initiated as a result of the oscillating interfacial shear forces momentarily and locally augmenting the radial interfacial shear stress that results from the normal clamping force.

> The very high forces productive of the radial extrusion of metal and large deformations away from the tool locale, which are characteristic of pressure welding, are not observed in vibratory welding.

4. The stress gradients precisely at the tip-work interface could not be resolved with the techniques used, although the stress situation in this locale could be and was estimated.

> It is remarkable that vibratory welds can be generated between two sheets with relatively little tip-sticking difficulty. Precise resolution and analysis of the stress gradients at the tip-work interface should throw light on this seeming anomaly. The difference between the stress distributions that produce a weld between two sheets and the distributions that do not produce a weld seems to be fairly small suggesting that weldability should depend critically on clamping force, tip radius, and power, but in actual practice this is not the case, probably due to thermal and/or inertia effects not operable in the photoelastic models.

5. The concept of alternating and spaced areas of local interfacial slip explains the characteristic physical and metallographic asymmetry which is usually present in vibratory welds.

6. Interfacial relative displacements of the magnitude suggested by the photoelastic analysis apparently can not produce melting.

7. The behavior of the photoelastic models falls nicely into a concept of a "stress coefficient of friction" which is smaller than the classical coefficient of static friction.

> Investigations should be carried out to determine if this concept is applicable to metals.

B. Energy Delivered to the Weld Zone

1. The threshold curve for welding as defined by the power-clamping force relationship with its characteristic minimum energy condition (MEC) at a specific clamping force, defines a condition of best impedance match between the welding sonotrode and the materials being welded.

> The MEC was established on the basis that temperature in the weld zone, for a given power value, approximates a maximum under the conditions of power and clamping force associated with the minimum value of the threshold curve; there is no apparent close correlation between the MEC and the weld quality properties of tensile-shear and cross-tension strength, weld area, thickness deformation, etc. Low-quality welds (those having surface damage, cracks, poor bonds, etc) can be expected in regions of the curve far removed from the MEC.

2. Measurements show that the standing-wave ratio varies from about 1.5 to 2.5, during a single weld interval.

> For an efficient utilization of power, the standing-wave ratio should be close to unity; certainly, a minimum variation should occur during any weld interval.

3. Information required to permit calculation of the desirable terminal impedance of a coupling member for welding can be determined with the information obtainable by the standing-wave-ratio technique.

> Variations in the standing-wave ratio determined from the oscillogram ellipse indicate variations in the acoustic impedance of the weld zone.

C. Material Properties and Weldability

1. The ordinary room-temperature hardness of a metallic material (Vickers microhardness indentation number) can be used as a measure of the energy required to produce a weld between two sheets.

> It is well known that a temperature rise of some magnitude is associated with ultrasonic welding. It was shown that the weld zone temperatures measured during welding of seven representative metals, with melting points ranging between 933 and 3273°K (660 and 3000°C) were between 35 and 50% of the absolute melting point in all cases. Appropriate hardness measurements provide a composite of yielding behavior, crystal structure, elastic constants, and work-hardening rate, indicating material properties in a manner approximating the ultrasonic elasto-plastic bonding process. Recent studies of high-temperature metals have evaluated material properties at elevated-temperature in terms of an homologous temperature (the ratio of absolute test temperature to the absolute melting temperature) on the basis that within limits the critical material properties decline from the values at room-temperature along more or less parallel lines.

2. On the basis of a curve fitting process, it appears that the energy required to generate a weld between two sheets increases roughly as the 3/2 power of the thickness of the material to be welded.

3. Tentatively, and subject to further investigation, the energy, in joules, required to promote a weld may be expressed as

$$E = K(t^{3/2})(h^{3/2}),$$

where t and h are the thickness and Vickers microhardness indentation number of the material, respectively.

> Although K is considered a constant, it is almost certainly a complex function involving several material properties. When the energy considered is acoustic energy, K appears to have a value of about 63.

4. Surface condition was further investigated to the end that more more power is associated with welding materials having heavy-coating thicknesses.

D. Metallurgy and Interfacial Disturbance

1. For at least two materials the disturbance at the interface between two sheets known to be productive of ultrasonic welding confirms the conclusions reached in the photoelastic investigations.

2. Metallurgical reactions such as recrystallization, phase transformation, precipitation, and diffusion are readily observed and identified in ultrasonic welds by microscopic examination, but no one of these phenomena has as yet been established as a common denominator in the process.

3. Surface films originally present along the interface are observed to be effectively dispersed in ultrasonic welds.

4. There is a possibility that under some circumstances surface films are dispersed in ultrasonic welds to produce dispersion-hardening phenomena in the weld zone.

5. There is no evidence that melting occurs in any ultrasonic monometallic weld.

6. In most cases, extensive deformation has occurred at the weld zone interface. This deformation usually results in breakdown of the original weld member surface films, producing metal-to-metal contact from one member to the other. Sometimes, a finely dispersed second phase of the surface film is concurrently produced within the parent metal near the weld interface. This dispersion may produce (by dispersion strengthening a weld bond which is stronger than the parent metal.

7. Ultrasonic welding generates heat at the weld interface. This may result in extensive subgrain formation in the region adjacent to the interface.

8. Bond formation in an ultrasonic spot weld initiates at the periphery of the weld spot. As the process proceeds during the weld time interval, the bond does not increase very much in size; rather, it grows by increasing the quality of the bond within the initial bond envelope.

9. Grain boundary shearing was observed in some of the samples.

10. A study of the fracture surface of these samples showed that failure is usually in a ductile manner.

11. The autoradiographic studies show that additional oxide can be generated at the weld interface during vibratory welding.

APPENDIX A

PHOTOELASTIC STRESS ANALYSIS

Photoelastic methods are widely used in engineering problems for detection of stress concentrations, but the application of the technique to complete stress analysis is neither widely practiced nor well understood. Although there is no dearth of literature (21, 27) on the subject, there are so many approaches to the problem that it seems worthwhile to describe in some detail the actual process we have used. It will be convenient to divide this discussion into three parts: a brief outline of the theory, description of the experimental technique, and a sketch of the data analysis.

In the first place, as is quite generally known, in cases of plane stress, photoelasticity permits, at every point of the model, determination of the direction of the principal axes of the stress tensor, and of the magnitude of the difference between the principal stresses. This information does not, however, suffice to determine directly the individual principal stresses, and, hence, it is not possible to discover by casual inspection of photoelastic patterns the actual stress at a particular point. The method that we have selected (27) depends on numerical or graphical integration of certain forms of the stress equations of equilibrium, using as data the information obtained photographically.

Let us assume that at every point of the model we are given the difference of the principal stresses, $\sigma_1 - \sigma_2$, and the angle ϕ measured counterclockwise from the x-axis to the direction of the σ_1-axis. We shall further adopt the usual convention that a plus (+) sign indicates tension and a minus (-) sign, compression. In the cases under consideration, the direction of the σ_1-axis varies continuously from point to point, and ϕ varies accordingly, but only in the range $-90° < \phi < +90°$, a circumstance that greatly simplifies the otherwise troublesome sign conventions.

Given a small elementary area at right angles to the x-axis, σ_x is the normal component of the stress acting across it and τ_{xy} is the tangential component; similarly for σ_y and τ_{yx}. These quantities are all positive in Fig. A-1, and of course $\tau_{xy} = \tau_{yx}$, so that ordinarily only τ_{xy} need be mentioned.

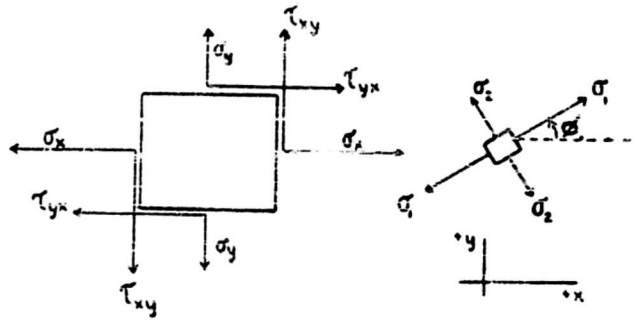


Fig. A-1: SIGN CONVENTIONS FOR PHOTOELASTIC DATA

Under the stated sign conventions, and with the stated limitation on the magnitude of ϕ, it may easily be shown that

$$\tau_{xy} = \tau_{yx} = 1/2(\sigma_1 - \sigma_2) \sin 2\phi \qquad \text{(A-1)}$$

and that

$$\sigma_x - \sigma_y = (\sigma_1 - \sigma_2) \cos 2\phi \,. \qquad \text{(A-2)}$$

These equations are not given the prominence that they deserve in some texts on photoelasticity. To prove them, consider Fig. A-2a, in which the vertical line represents a unit area at right angles to the x-axis. The principal stresses σ_1 and σ_2 act at right angles to areas of magnitude $\cos\phi$ and $\sin\phi$, respectively, and they represent the total force exerted on these areas.

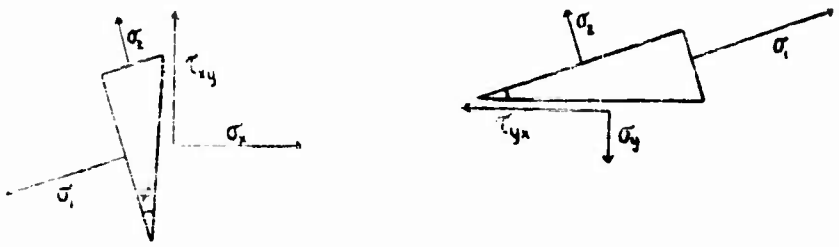


Fig. A-2: RESOLUTION AND TRANSFORMATION OF THE STRESS TENSOR

Summing horizontal components gives

$$\sigma_x = \sigma_1 \cos^2 \phi + \sigma_2 \sin^2 \phi ,$$

and summing vertical components gives

$$\tau_{xy} = \sigma_1 \sin \phi \cos \phi - \sigma_2 \sin \phi \cos \phi .$$

In Fig. A-2b, the horizontal line represents a unit area at right angles to the y-axis, while σ_1 and σ_2 now act at right angles to areas of magnitudes $\sin \phi$ and $\cos \phi$, respectively. We then infer that

$$\sigma_y = \sigma_1 \sin^2 \phi + \sigma_2 \cos^2 \phi$$

$$\tau_{yx} = \sigma_1 \sin \phi \cos \phi - \sigma_2 \sin \phi \cos \phi .$$

Algebraic manipulation yields Eq (A-1) and (A-2) immediately.

Equations (A-1) and (A-2) are particularly important in photoelasticity because the right members contain only the quantities that may be determined immediately from the photoelastic patterns. It will be noted that the component of shear across any plane at any point in the model may be directly determined from Eq (A-1). Equation (A-2), on the other hand, is convenient for discovering σ_x when σ_y has been computed or vice versa. But neither the equations nor any combination of them suffices to determine σ_x, σ_y, σ_1, or σ_2 separately.

Completion of the analysis depends on the use of either or both of the following equations (27)

$$\frac{\partial \sigma_x}{\partial x} + \frac{\partial \tau_{yx}}{\partial y} = 0 . \qquad \text{(A-3)}$$

$$\frac{\partial \sigma_y}{\partial y} + \frac{\partial \tau_{xy}}{\partial x} = 0. \qquad \text{(A-4)}$$

It will be noted that in each of these equations, the second term, though not directly observed in photoelasticity, can nevertheless be easily inferred by simple graphical methods, that is, by plotting τ_{xy} as a function of x or y as the case may be, and finding the slope. Let us assume that $\partial \tau_{yx} / \partial y$ has thus been found at every point of the model. We now select values of this derivative at points along any line parallel to the x-axis that we may choose, say $y = c$. Along this line, let $\partial \tau_{xy} / \partial y = f(x)$. Then along this same line, from Eq (A-3),

$$\frac{\partial \sigma_x}{\partial x} = -f(x) . \qquad \text{(A-5)}$$

Since the right member is, along the selected line at any rate, a function of x alone, this equation may be directly integrated in the form

$$(\sigma_x)_b - (\sigma_x)_a = -\int_a^b \frac{(\partial \tau_{xy})}{\partial y}\, dx \,. \qquad (A\text{-}6)$$

where a and b are the values of x between which the integral is evaluated. (Fig. A-3).

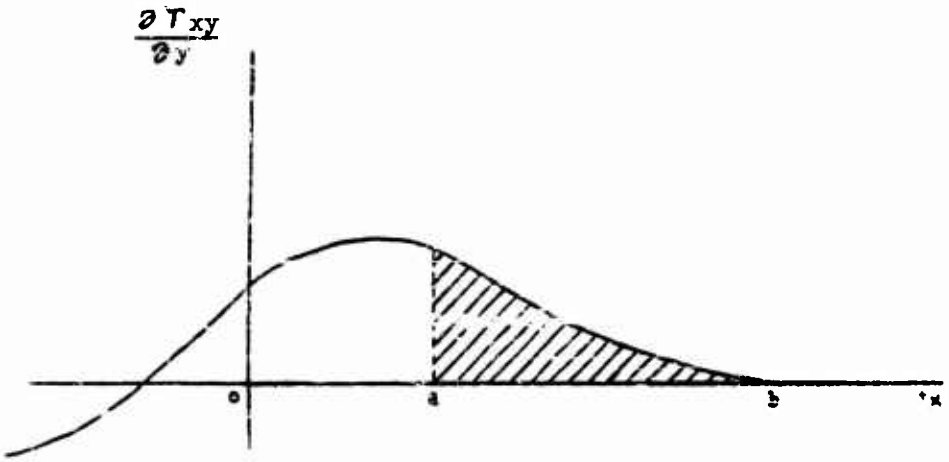


Fig. A-3: PLOT OF SHEARING STRESS SLOPE $\partial \tau_{xy}/\partial y$ AS A FUNCTION OF X

The shaded area is equal to $(\sigma_x)_a - (\sigma_x)_b$.

(Note the effect of the minus sign (-) in Eq (A-5). If $(\sigma_x)_b = 0$, this area represents σ_x, itself, at the point $x = a$, $y = c$.)

Refer now to Fig. A-4: σ_x is known at all points along the line $y = c$.

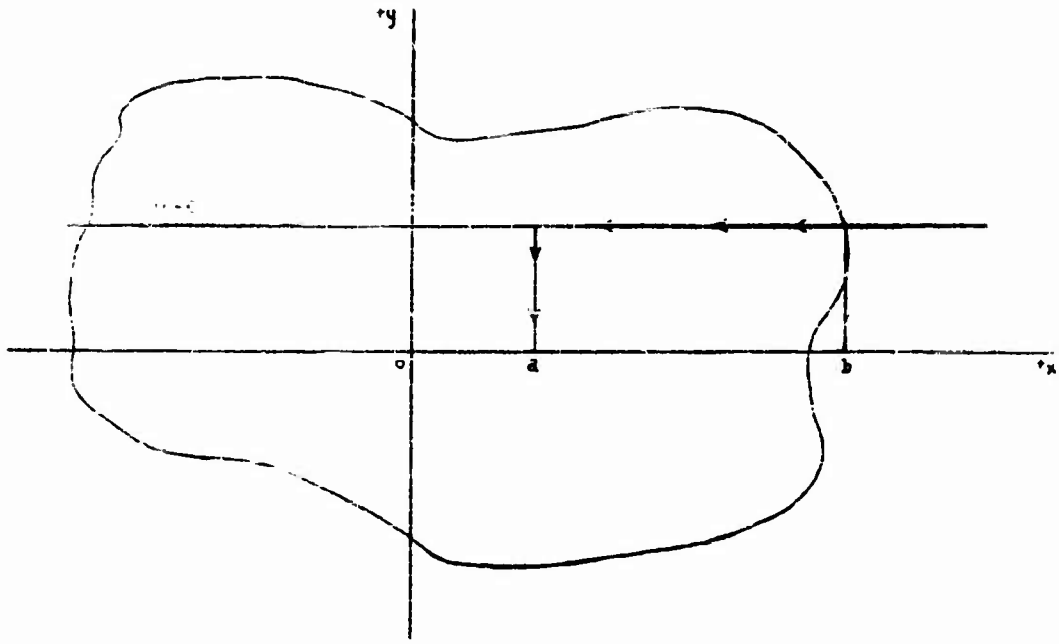


Fig. A-4: SKETCH SHOWING THE PATH OF INTEGRATION FOR DETERMINING σ_x AND σ_y AT THE ARBITRARY POINT $x = a$, $y = 0$.

By the use of Eq (A-2) we may now compute σ_y at all points along $y = c$. Assume that we next wish to find σ_x and σ_y at the point $x = a$, $y = 0$. For this purpose we need to integrate Eq (A-4) along the line $x = a$:

$$(\sigma_y)_c - (\sigma_y)_o = - \int_o^c \left(\frac{\partial \tau_{yx}}{\partial x}\right) dy \ . \qquad \text{(A-7)}$$

Since $(\sigma_y)_c$ has already been found, $(\sigma_y)_o$ may be calculated, and a further application of Eq (A-2) will yield both principal stresses at the arbitrary point $x = a$, $y = o$. However, for the purposes of the present work, the knowledge of σ_x and σ_y will suffice.

It is clear that great pains must be taken to systematize handling all the photoelastic data, in order to avoid errors in signs. However, before describing this, it seems advisable to explain the experimental technique by which $\sigma_1 - \sigma_2$ and ϕ are determined.

For our particular problem, a model was constructed of Catalin*, ten times as large as the actual specimens whose weldability is being studied. These specimens are of 0.050-in. thick metal sheet, which can be easily welded with sonotrodes of a wide range of tip radius. The ratio of tip radius, r, to thickness, t, for this particular experiment was $r/t = 60$. The two pieces of Catalin were 6 in. long, 3.5 in. high, and 0.25 in. thick; the lower piece rested on a flat surface, and the upper was loaded by a tip of 30-in. spherical radius.

A specimen of the material was calibrated by the compression method (21), in order to be able to convert the observed stress patterns into pounds per square inch. This procedure is particularly valuable when it becomes necessary to check numerically the results of the somewhat arduous analysis. The fringe value obtained was 38.6-psi shear stress per inch of thickness, which corresponds closely to the values published for this material. The usual precautions were taken to avoid "time edge effects", and in general standard experimental procedures were followed (21).

The difference in the principal stresses, $\sigma_1 - \sigma_2$, is revealed at all points in the model by a single photograph in circularly polarized monochromatic light (21). For this purpose it is convenient to load the model to almost the elastic limit. Each "fringe" in the resulting photograph shows the locus of points at which the difference in

* Catalin 61-893 Photoelastic Resin, Catalin Corp. of America, Fords, N.J.

the principal stresses has a fixed value, that is, the magnitude of the total shearing stress is constant along these curves, though the direction of maximum shear varies markedly. As long as the laws of linear elasticity are obeyed, this pattern is in one sense independent of load, for if the load were doubled, the result would be to interpose a new fringe between every pair of existing fringes. Thus, the greater the load, the more detailed are the available data.

The direction of the principal stresses, ϕ, is determined by a series of photographs in plane-polarized white light (21). Each individual photograph shows the locus of points at which the principal stresses make angles of precisely 45° with the plane of polarization. A series of 6 photographs, at 15° increments, will usually yield an adequate set of these isoclinic lines, though it may be convenient to choose the set in some other way. Figure A-5 reproduces the photographic data.

The quantitative analysis of these photographs in the light of the theory outlined above requires several steps. In this work, it is convenient to use the fringe order, itself, as the unit of stress; this is usually a small number (0-10), known at best to two significant figures, which can be easily converted into psi as required. It is first necessary to superpose all the photoelastic data on a single drawing to large scale. Care must, of course, be taken that all the experimental photographs be magnified to the same scale, that the origins and axis orientation coincide, and, unless the pattern is symmetric, that the negatives all be kept "right side up." Best results have been obtained by tracing the fringes by hand as they appear when projected optically onto the drawing. Figure A-6 shows a typical result of this procedure.

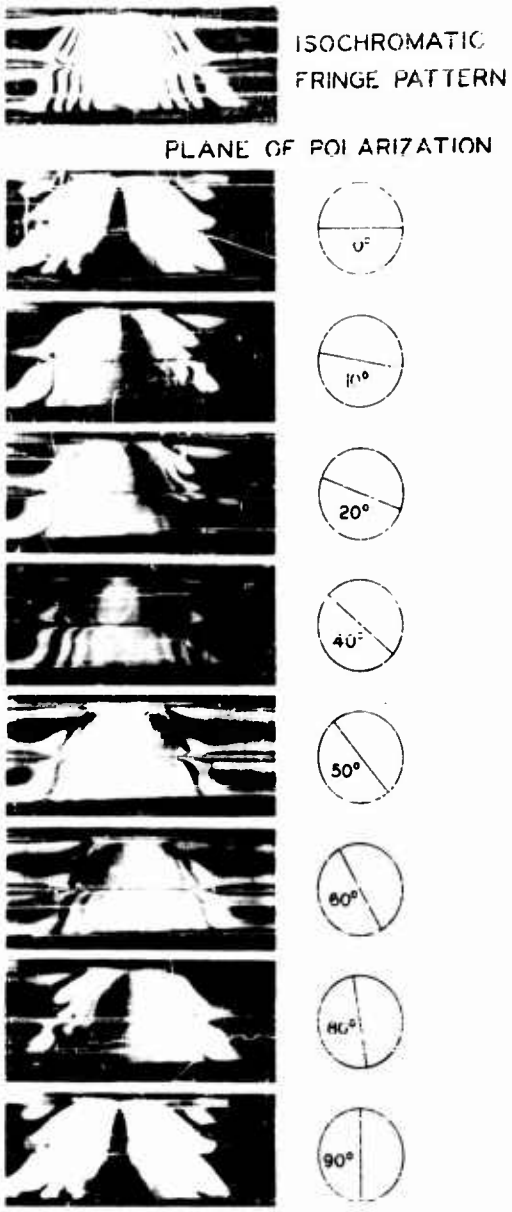


Fig. A-5: ISOCHROMATIC FRINGE PATTERN AND ISOCLINIC LINES

Taken at the indicated angles for a normal load of 300 lb and a transverse load of 52 lb (machine load of 76)

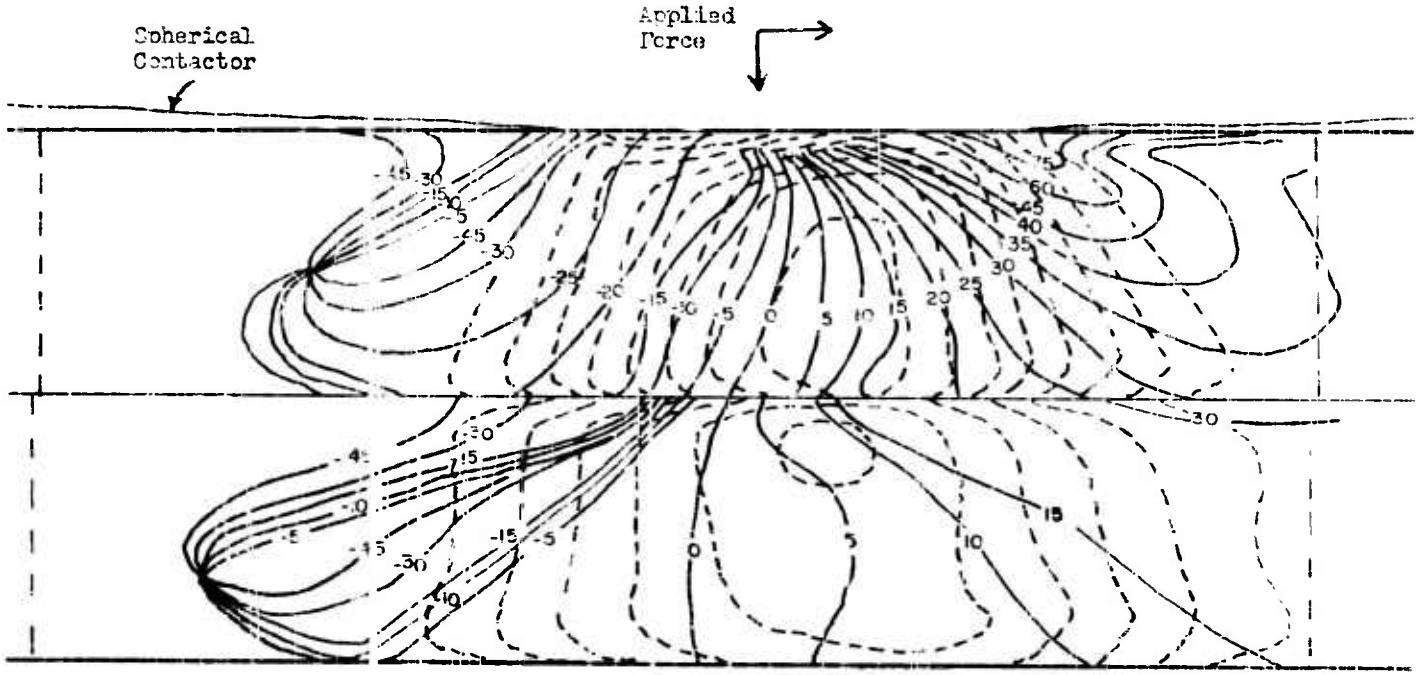


Fig. A-6: SUPERPOSITION OF RELEVANT PHOTOELASTIC DATA

A cartesian coordinate system is next introduced. Even though only a few regions are to be investigated, experience indicates that a complete grid should be initially assigned, preferably with one of the axes coinciding with the surface under study -- in our case with the weld interface. From the drawing, thus prepared, data for computation of τ_{xy}, as specified by Eq (A-1), can now be readily obtained. A few data of this sort are shown in Table A-I.

Table A-I

SAMPLE OF NUMERICAL DATA

Point	σ_1 σ_2	ϕ	Sin 2ϕ	τ_{xy} = $1/2(\sigma_1 - \sigma_2)\sin 2\phi$	$\frac{\partial \tau_{xy}}{\partial y}$*
$a_1(-7,c_1)$	0.9	-16	-0.530	-0.238 fringe	
$(-7,c)$					-0.063
$b\ (-7,c_2)$	0.9	-21	-0.669	-0.301 fringe	
$a_2(-5,c_1)$	2.6	-12.5	-0.423	-0.520 fringe	
$(-5,c)$					+0.096
$b_2(-5,c_2)$	1.6	-16	-0.530	-0.424 fringe	

* $\left(\frac{\partial \tau_{xy}}{\partial y}\right)_{y=c} \approx \frac{\Delta \tau_{xy}}{\Delta y}$; let Δy = 2 cm,

then $(\Delta \tau_{xy})_{y=c} = (\tau_{xy})_{y=c_2} - (\tau_{xy})_{y=c_1}$;

and $\left(\frac{\partial \tau_{xy}}{\partial y}\right)_{y=c} = \frac{(\tau_{xy})_{y=c_2} - (\tau_{xy})_{y=c_1}}{2}$, where the units are "fringes per centimeter".

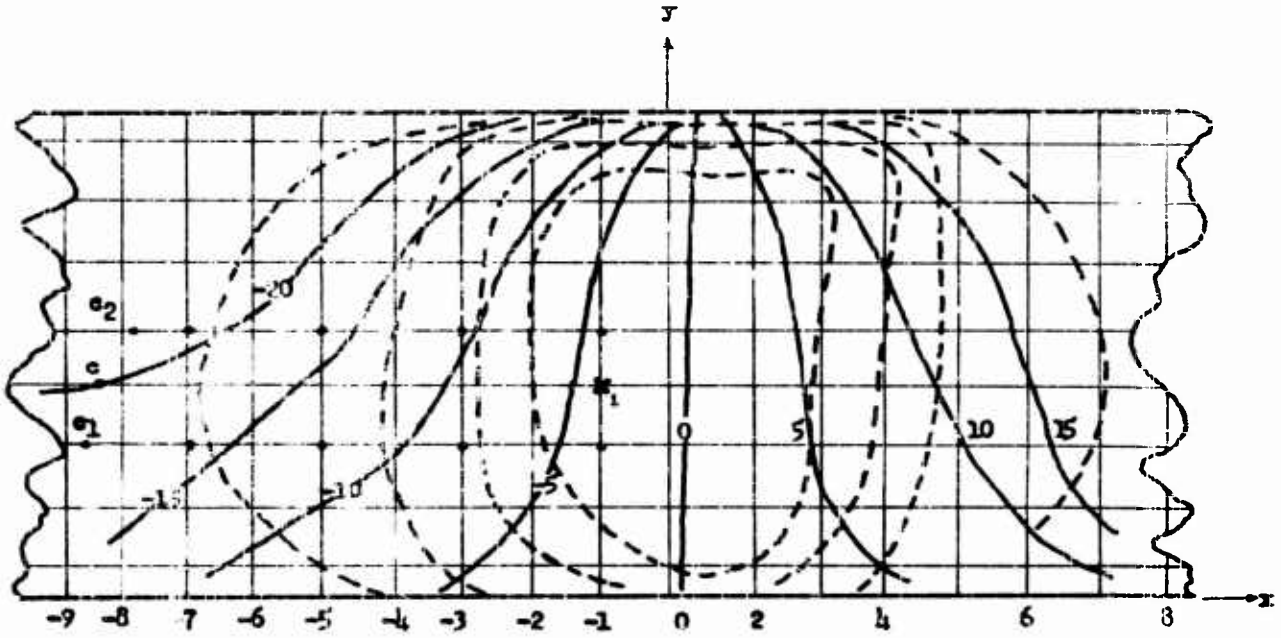


Fig. A-7: HYPOTHETICAL SKETCH OF ISOCHROMATIC FRINGES (dotted lines) SUPERPOSED ON ISOCLINIC LINES (solid lines) IN A PHOTO-ELASTIC MODEL

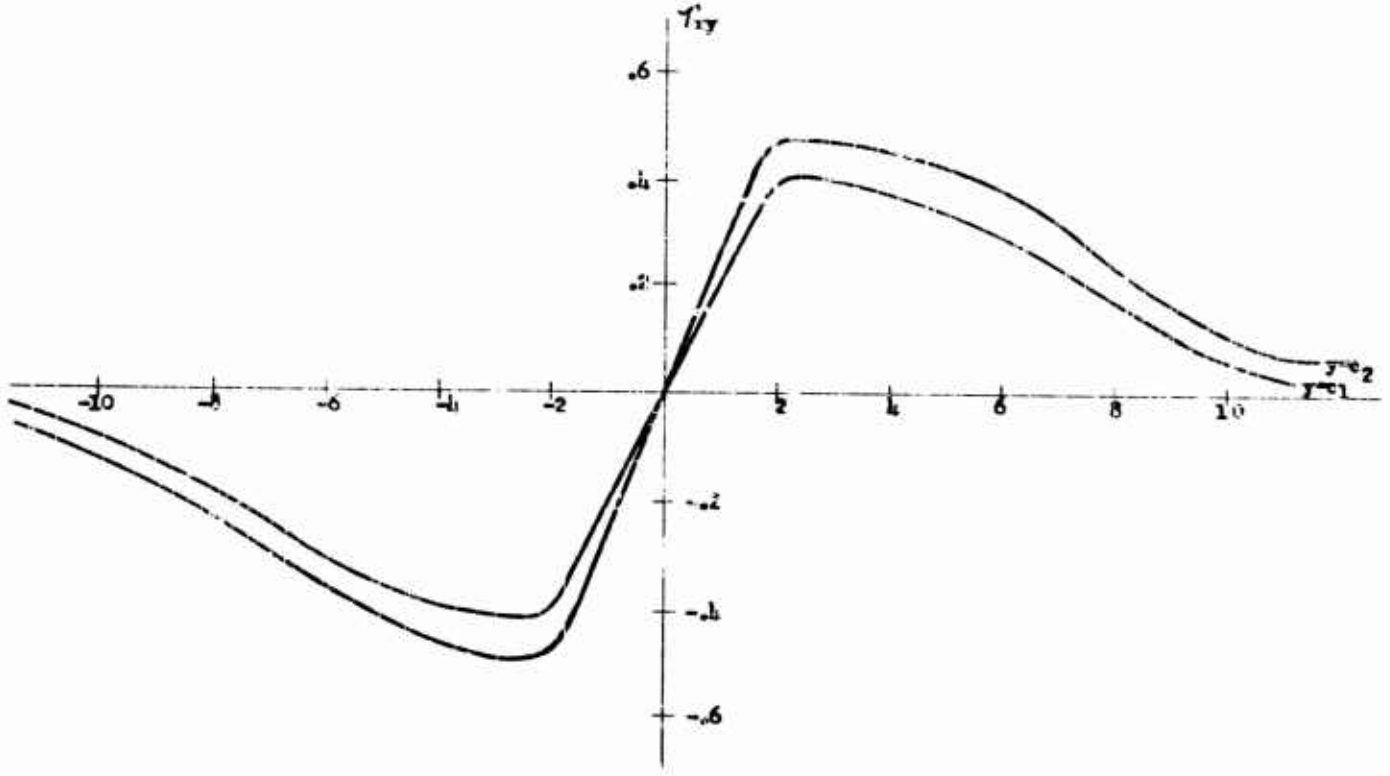


Fig. A-8: SHEARING STRESS DISTRIBUTIONS WITHIN THE MODEL

Values of $\partial \tau_{xy}/\partial y$ are approximated for use in the graphical integration as $\Delta \tau_{xy}/\Delta y$. In determining these increments, it is convenient first of all to plot on the same graph τ_{xy} as a function of x, first as evaluated along the line $y = c_1$, and next along the line $y = c_2$. These lines straddle the line $y = c$, and are separated by a distance $\Delta y = c_2 - c_1$. Such plots appear in Fig. A-8, and a portion of the relevant data appears in Table A-I. At this point, one may check numerically to discover whether or not the plotted values of shearing stress are compatible with the known transverse load L_T, for, of course, we expect that

$$L_T = \int_{-\infty}^{\infty} \tau_{xy} \, dx$$

for every horizontal line drawn across the model.

Table A-I also contains computed values of $\Delta \tau_{xy}/\Delta y$, which may be plotted as a function of x as representing $\partial \tau_{xy}/\partial y$ along the line $y = c$. It will be noted that the quantity $\Delta \tau_{xy}$ is represented by the difference in ordinate between the curves in Fig. A-8, and, accordingly, the area between these two curves is proportional to the integral of Eq (A-6). It has occasionally been convenient to evaluate this integral by measurement of this area instead of by plotting $\partial \tau_{xy}/\partial y$ separately, but this depends upon the suitability of the scale and upon the particular situation.

Completion of the problem merely requires integration down the various vertical lines to the interface. In order to "turn the corner", that is, to shift to integration involving σ_y instead of σ_x, we must compute σ_y at as many points along the line $y = c$ as may be required.

When this has been accomplished, a second numerical check is possible, for the vertical load L_y must be equal to the integral of σ_y taken along any horizontal line through the model:

$$L_v = \int_{-\infty}^{\infty} \sigma_y \, dx.$$

This check on L_y and that previously noted for L_x are likewise applied to the stresses evaluated at the weld interface as a final check on the accuracy. In general these integrals may be verified to an accuracy of about 10%.

When this has been accomplished, a second numerical check is possible, for the vertical load L_y must be equal to the integral of σ_y taken along any horizontal line through the model:

$$L_v = \int_{-\infty}^{+\infty} \sigma_y \, dx.$$

This check on L_y and that previously noted for L_T are likewise applied to the stresses evaluated at the weld interface as a final check on the accuracy. In general these integrals may be verified to an accuracy of about 10%.

APPENDIX B

INVESTIGATION OF CONTACT SURFACE SHEARING STRESS

The ratio of shearing stress τ_{xy}, to normal stress σ_y, productive of slip, is deemed important. In particular, the original hypothetical curves of normal stress and observed shearing stress postulated that local slip and, therefore, welding should occur in the locale where the observed shearing stress before slip equalled the maximum supportable shearing stress. Furthermore, the maximum supportable transverse thrust at the tip-work interface must somehow be greater than the corresponding maximum at the "weld" interface, or slip will occur at the former instead of the latter so that no weld will result.

Thus, it has been clear that interpretation of the photoelastic analysis depends to a considerable extent on the magnitude of the shearing stresses that can exist at the weld interface, and at the sonotrode tip, without slip. No glib comment based on the "coefficient of friction" can yield an intelligible explanation because the ratio of shearing stress τ_{xy} to normal stress σ_y varies over a large range and even reverses sign at the weld interface. However, some estimate must be made of the maximum allowable value of τ_{xy}/σ_y, preferably in a specimen where both are constant.

The experimental arrangement chosen for this determination is shown schematically in Fig. B-1. Two tubes of Catalin, the same material used for earlier work with photoelastic models, were pressed together by an axial load. The annular contact area was carefully polished and, in fact, repolished after each initiation of slip, to eliminate uncertainties due to surface damage when slip occurs. Slip was induced by means of a carefully measured torque, and ball bearings were used in the force system to minimize friction except at the surface under study. The shearing stress does vary somewhat across the annular contact area, for the shear in a tube under torsion is proportional to the radius. Thus, initial

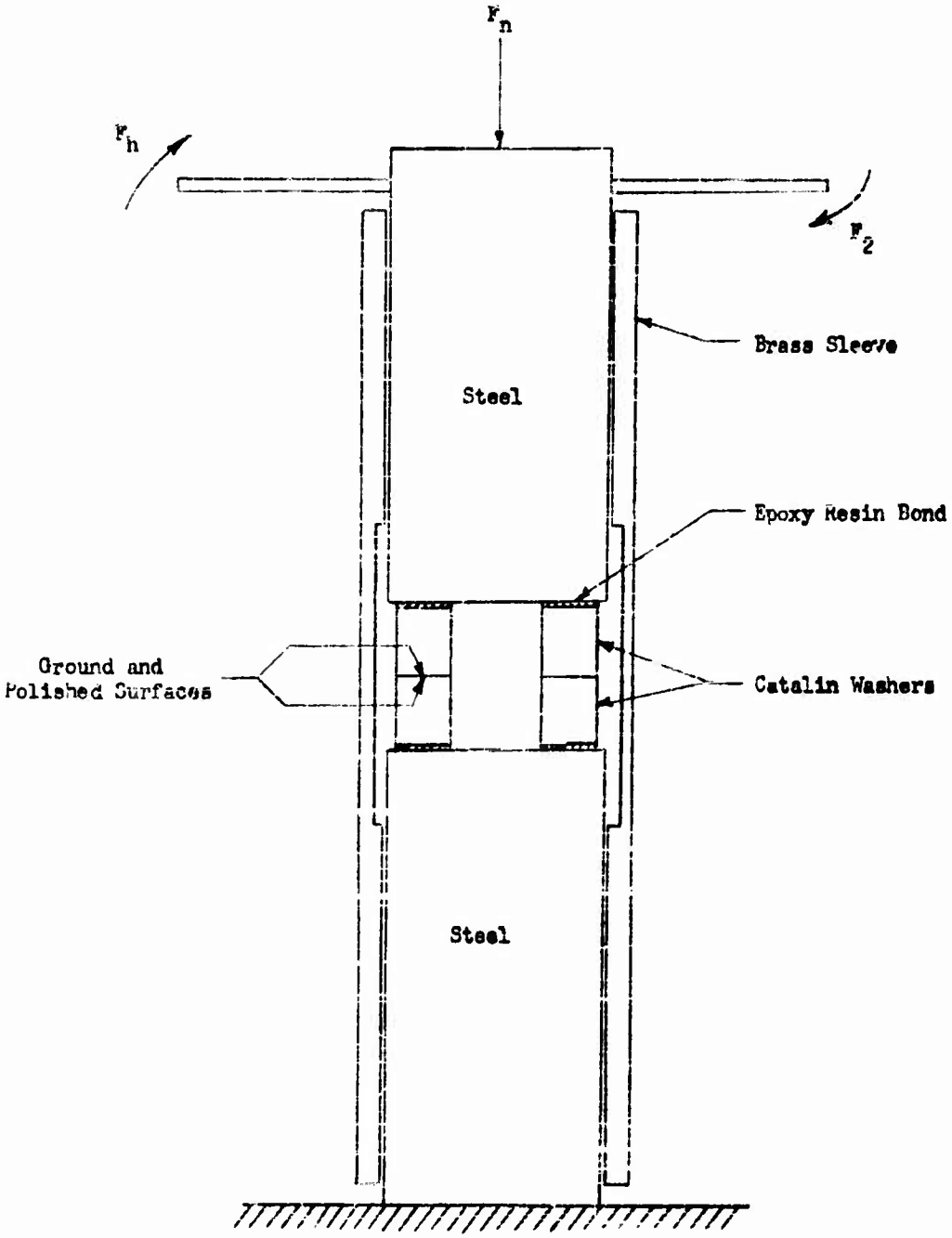


Fig. B-1: SCHEMATIC OF APPARATUS USED TO ESTABLISH MAXIMUM SUPPORTABLE SHEARING STRESS

slip is to be expected at the outside of the annulus, but, when gross sliding occurs, the shearing stress should be practically constant, independent of radius, since it is presumably limited by a constant normal stress σ_y. Under such conditions, the shearing stress, τ_{xy}, may be computed from the formula:

$$L = 2\pi \tau_{xy} \int_a^b r^2 \, dr,$$

where L is the torque required to produce sliding, and a and b are the inner and outer annular radii.

Figure 10 implies an almost classic example of constant "coefficient of friction", particularly at the higher stresses even though these greatly exceed those encountered in the present photoelastic investigation. Below a stress of six fringes, which is the range of critical interest, there is a variation of perhaps 15%, which, while interesting, probably will not affect the interpretation of the photoelastic analysis.

In connection with this type of measurement, it will be observed that the ratio of transverse load to normal load that corresponds to incipient slip (Case II, Table I) is 52/300 = 0.17. This figure is approximately one-third the value corresponding to the classical "coefficient of friction" deduced from the torsional tests and indicates clearly why the gross concept of "coefficient of friction" in terms of total applied load components is valueless in an investigation of this kind.

APPENDIX C

MEASUREMENT OF TRANSMITTED ULTRASONIC POWER

Analysis (4) has shown that it is possible to measure the acoustic power passing along a uniform cylindrical rod by sensing the standing wave ratio (SWR) therein. A subsequent physics experiment established that the technique could be utilized to determine the vibratory power necessary to calibrate equipment by calorimetric methods. The SWR technique has been routinely used in the course of these investigations to ascertain relationships between the net energy required to accomplish a weld and specific materials and thicknesses.

However, the obtainment of specific data involves motion picture photography of an oscilloscope trace, enlargement thereof, manual integration of included areas, additional plotting, etc, all of which are laborious and time consuming. This Appendix is concerned with the instrumentation necessary to eliminate the work of photographing the oscilloscope trace and converting the information so obtained into useful numbers.

The following analysis assumes an instrument for measuring average electrical power at 20 kilocycles per second over the necessary time interval. Such an instrument is manufactured by the John Fluke Manufacturing Company and is designated as VAW meter, Model 102. This instrument is designed to indicate $P = ei$, each in its appropriate phase.

Therefore, the following analysis can be made:

$$\left.\begin{aligned} e &= E \cos \omega t \\ i &= I \cos(\omega t + \delta) \end{aligned}\right\} \qquad \text{(C-1)}$$

$$P = ei = EI \cos \omega t \left[\cos \omega t \cos\delta - \sin \omega t \sin\delta\right] \qquad \text{(C-2)}$$

$$P = \frac{1}{T}\int_0^T ei\,dt = EI\cos\delta/2 \qquad \text{(C-2a)}$$

The pickup outputs are (4):

$$\Xi_1 = \xi_+ \cos 2\pi\left(\frac{t}{T} - \frac{x}{\lambda}\right) + \xi_- \cos 2\pi\left(\frac{t}{T} + \frac{x}{\lambda}\right) \qquad \text{(C-3)}$$

$$\Xi_2 = \xi_+ \cos 2\pi\left(\frac{t}{T} - \frac{x}{\lambda} - \frac{\pi}{2}\right) + \xi_- \cos 2\pi\left(\frac{t}{T} + \frac{x}{\lambda} + \frac{\pi}{2}\right) \qquad \text{(C-4)}$$

$$= \xi_+ \sin 2\pi\left(\frac{t}{T} - \frac{x}{\lambda}\right) - \xi_- \sin 2\pi\left(\frac{t}{T} + \frac{x}{\lambda}\right)$$

By suitable circuitry, one can advance the phase of Ξ_1 or retard the phase of Ξ_2 by 90°. Considering the latter, it becomes:

$$-j\,\Xi_2 = \xi_+ \cos 2\pi\left(\frac{t}{T} - \frac{x}{\lambda}\right) - \xi_- \cos 2\pi\left(\frac{t}{T} + \frac{x}{\lambda}\right) \qquad \text{(C-5)}$$

Now replacing in Eq (C-2) i by Ξ_1, and e by $-j\,\Xi_2$ as inputs to the VAW meter, it will indicate the mean value of the product (ei), the mean value of

$$(\Xi_1)(-j\,\Xi_2) = \frac{1}{T}\int_0^T \left[\xi_+ \cos 2\pi\left(\frac{t}{T} - \frac{x}{\lambda}\right) + \xi_- \cos 2\pi\left(\frac{t}{T} + \frac{x}{\lambda}\right)\right] \qquad \text{(C-6)}$$

$$\left[\xi_+ \cos 2\pi\left(\frac{t}{T} - \frac{x}{\lambda}\right) - \xi_- \cos 2\pi\left(\frac{t}{T} + \frac{x}{\lambda}\right)\right] dt$$

$$= \frac{1}{T}\int_0^T \left[\xi_+^2 \cos^2 2\pi\left(\frac{t}{T} - \frac{x}{\lambda}\right) - \xi_-^2 \cos^2 2\pi\left(\frac{t}{T} + \frac{x}{\lambda}\right)\right] dt$$

$$= \pi\left(\xi_+^2 - \xi_-^2\right) = P,$$

The design of necessary instrumentation is thus clearly defined as:

a. A VAW meter of up to 20 kilocycles per second frequency response, which is available. From correspondence with the manufacturer it appears that the meter indicating circuit contains the greatest time delay, increasing the over-all instrument response to approximately one second. Taking an output signal from the VAW ahead of the meter circuit and applying this to a strip chart recorder of 100 cps response will permit determination of the instantaneous power transmitted over any average period of 0.01 sec.

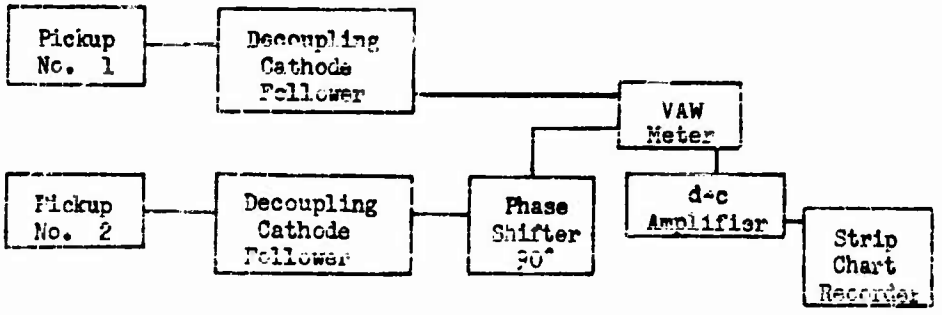
b. Cathode follower circuits to decouple the crystal pickups from the phase-shifting network.

c. Adjustable phase-shifting network to shift the signal of one pickup by 90° prior to its application to the VAW meter.

d. Adjustable detection circuit which will yield a d-c signal proportional to the signal feeding the meter circuit of the VAW meter.

e. A d-c amplifier and strip chart recorder for recording these signals.

In the block form, the following results:



It is thus indicated that the vibratory power traversing an acoustical coupler, averaged over 0.01 sec, can be recorded on a strip chart Brush or Sandborn-type oscillograph.

Up to and including the slow-response VAW indicating meter, this instrumentation was assembled. Vibratory power data obtained therefrom, at one second plus time intervals, compared favorably with previously obtained vibratory power data from the photographed and integrated oscilloscope ellipse traces.

APPENDIX D

DETERMINATION OF THE TRANSDUCER TERMINAL IMPEDANCE

A method for determining the transducer load impedance utilizes a knowledge of the characteristic impedance of the transmitting rod and the instrumentation thus far developed for the standing wave ratio technique of power measurement. Given the standing wave ratio and the distance from the end of the coupler to the nearest maximum in the standing wave pattern, the terminal impedance can be defined through the equation:

$$\frac{Z_t}{Z_c} = \frac{\xi_{min} \cos \frac{2\pi}{\lambda} X_o - j\, \xi_{max} \sin \frac{2\pi}{\lambda} X_o}{\xi_{max} \cos \frac{2\pi}{\lambda} X_o - j\, \xi_{min} \sin \frac{2\pi}{\lambda} X_o} \qquad \text{(D-1)}$$

where the notation for this and the following equation is:

Z_t = the acoustic impedance which terminates the bar

Z_c = acoustic impedance which characterizes the transmitting or coupling bar

λ = wavelength of the sound waves in the bar

X_o = distance from the termination to the nearest particle displacement maximum

ξ = instantaneous longitudinal displacement of a particle, a function of both time and position along the bar

ξ_{max} = maximum particle displacement

ξ_{min} = minimum particle displacement

ξ_+ = amplitude of a wave traveling toward the load

ξ_- = amplitude of a reflected wave traveling back toward the transducer

A = area of the cross-section of the bar

ρ = density of the bar

c = velocity of longitudinal waves along the bar

f = frequency of oscillation

ω = angular frequency

k = wave number

t = time

X = position along the rod

E = Young's modulus

F = force associated with a wave.

Acoustic power is transmitted practically by longitudinal, radial, torsional, transverse, or other well known oscillatory type vibrations. The following theory developed for deriving Eq (D-1) is developed specifically for longitudinal vibrations; however, it is sufficiently general to permit application to any vibrational mode provided the measurements are related to the appropriate particle motions.

The following equations hold for a longitudinal wave on a uniform slender rod of less than one-quarter wavelength diameter

$$\frac{\partial^2 \xi}{\partial X^2} = c^2 \frac{\partial^2 \xi}{\partial t^2} \qquad \text{(D-2)}$$

$$c = \sqrt{\frac{E}{\rho}} \qquad \text{(D-3)}$$

$$F = -AE \frac{\partial \xi}{\partial X} . \qquad \text{(D-4)}$$

It is assumed that a source of acoustic power is delivering energy in the form of wave motion. Unless the load exactly matches the characteristic impedance of the coupling system (Apc), waves are reflected from the load to the transducer, and a pattern of standing waves is

established on the rod. If an origin for X is chosen at a position of the maximum particle displacement, and the positive direction is from the transducer toward the load, the pattern of standing waves is given by

$$\xi = \xi_+ e^{j(\omega t - kX)} + \xi_- e^{j(\omega t + kX)} \qquad \text{(D-5)}$$

where the actual displacement ξ is equal to the real portion of the equation.

The particle velocity $\dot{\xi}$ is found by differentiating Eq (D-5) to be

$$\dot{\xi} = j\omega \left[\xi_+ e^{j(\omega t - kX)} + \xi_- e^{j(\omega t + kX)} \right] \qquad \text{(D-6)}$$

The strain in the rod $\partial \xi / \partial X$ is on the other hand given by

$$\frac{\partial \xi}{\partial X} = -jk \left[\xi_+ e^{j(\omega t - kX)} - \xi_- e^{j(\omega t + kX)} \right]. \qquad \text{(D-7)}$$

The force F, Eq (D-4), is found in terms of this strain to be

$$F = jkAE \left[\xi_+ e^{j(\omega t - kX)} - \xi_- e^{j(\omega t + kX)} \right]. \qquad \text{(D-8)}$$

The impedance across a section of the rod specified by the coordinate X is the ratio of force to velocity. Thus, if Z_c represents the impedance of a rod extending indefinitely to the right, so that reflected waves are never observed, ξ_- is zero and it is easily seen that

$$Z_c = \frac{F}{\dot{\xi}} = \frac{kAE}{\omega} = A\rho c. \qquad \text{(D-9)}$$

For this analysis the coordinate X = 0 was chosen to correspond to a position of maximum particle displacement, ξ_{max} in the standing wave. With this hitherto arbitrary origin chosen to correspond

to the maximum nearest the terminal impedance, the distance from $X = 0$ to the terminal surface will be designated X_o. Then at this coordinate is found

$$Z_t = \frac{F}{\dot{\xi}} = \frac{EAk}{\omega} \frac{\xi_+ e^{j(\omega t - kX)} + \xi_- e^{j(\omega t + kX)}}{\xi_+ e^{j(\omega t - kX)} - \xi_- e^{j(\omega t + kX)}} \tag{D-10}$$

$$Z_t = \frac{EAk}{\omega} \frac{(\xi_+ - \xi_-) \cos kX_o - j(\xi_+ + \xi_-) \sin kX_o}{(\xi_+ + \xi_-) \cos kX_o - j(\xi_+ - \xi_-) \sin kX_o}. \tag{D-11}$$

Examination of equation 5 reveals that the maximum and minimum particle displacements ξ are respectively

$$\begin{aligned} \xi_{max} &= \xi_+ + \xi_- \\ \xi_{min} &= \xi_+ - \xi_- \end{aligned} \tag{D-12}$$

Then combining Eq (D-11) and D-12) gives

$$Z_t = \frac{EAk}{\omega} \left[\frac{\xi_{min} \cos kX_o - j \xi_{max} \sin kX_o}{\xi_{max} \cos kX_o - j \xi_{min} \sin kX_o} \right] \tag{D-13}$$

Accordingly for the ratio Z_t/Z_c from Eq (D-1) it is found from Eq 9 and 13

$$\frac{Z_t}{Z_c} = \frac{\frac{EAk}{\omega}}{\frac{EAk}{\omega}} \left[\frac{\xi_{min} \cos kX_o - j \xi_{max} \sin kX_o}{\xi_{max} \cos kX_o - j \xi_{min} \sin kX_o} \right]$$

$$\frac{\xi_{min} \cos \frac{2\pi}{\lambda} X_o - j \xi_{max} \sin \frac{2\pi}{\lambda} X_o}{\xi_{max} \cos \frac{2\pi}{\lambda} X_o - j \xi_{min} \sin \frac{2\pi}{\lambda} X_o} \tag{D-14}$$

APPENDIX E

THE POWER-FREQUENCY INTERACTION

The power delivered by a transducer-coupler system varies as the square of both the frequency and the amplitude. Thus, ultrasonic welding which is dependent upon vibratory energy is related to frequency and amplitude.

A priori considerations show that a vibratory amplitude of, say, 1/10 in. which might be possible at 100 cps would be impractical for joining foil of 0.001-in. thickness, and a vibratory amplitude of, say, 0.0001 in. would elastically deform only the surface of a 1-in. plate and be unproductive of ar interfacial disturbance between two 1-in. plates.

The relation between frequency and amplitude is imposed by the transducer and its coupler system because of the limits inherent in the properties of the materials of which they are made.

Larger amplitude levels but at lower force levels can be achieved through the use of velocity transformers (31), but, in any case, a limiting amplitude (dependent upon the strain and shape factor) exists for any resonant coupler element. The allowable elastic strain in an element of a resonant coupler system is determined by the fatigue strength of the material of which the coupler system element is made.

The interrelationship which does exist and the "level" of mechanical vibration can be expressed in the following manner (22).

The particle displacement at any section of a 1/2-wavelength resonant ultrasonic element can be expressed as:

$$\xi = \xi_m e^{j(\omega t - kx)}, \qquad \text{(E-1)}$$

where ξ is the particle displacement at any time (t) and position (x); ξ_m is the maximum value; ω is the radial frequency, $2\pi f$, in radians/sec; k is the wave number, $2\pi/\lambda = \omega/c$; and λ is the wavelength of sound traveling at velocity c in the material.

A solution of this equation with

$$c = \omega/k \tag{E-1a}$$

relates the particle velocity ($\dot{\xi}$) and the strain $\partial\xi/\partial x = \xi_x$ to the displacement which for magnitudes only yields

$$\dot{\xi} = \omega\xi$$

and $$\xi_x = k\xi . \tag{E-2}$$

Combining with Eq (E-1a) yields the amplitude dependence upon the strain:

$$\xi = \frac{c}{\omega}\,\xi_x . \tag{E-3}$$

The stress (σ) and frequency (f) interaction is obtained by appropriate substitutions for the strain (from Hookes' Laws) and wavelength from which the amplitude varies as

$$\xi_m = \frac{\sigma_m}{E}\,\frac{c}{2\pi f}, \quad = \frac{\sigma_m\, c}{\omega E}, \tag{E-4}$$

and for $c = \sqrt{E/\rho}$

$$\xi_m = \frac{1}{f} \cdot \frac{\sigma_m}{2\pi\sqrt{E\rho}} . \tag{E-5}$$

Thus, the maximum amplitude of any resonant element (even multiples of 1/4 wavelength) in a transducer-coupler system varies linearly with the maximum allowable stress, which is a mechanical property of the material; inversely with the modulus and density, which are physical properties of the material; and inversely with the frequency.

Transposing this equation reveals further that

$$\xi_m f = \frac{\sigma_m}{2\pi\sqrt{E\rho}} = \text{a constant} \qquad \text{(E-6)}$$

and depends upon the mechanical and physical properties of the material.

It was shown in the Final Report of Phase I of this project (4) that the acoustical power delivered by any ultrasonic system can be defined by the equation:

$$P = \frac{Rc\,\omega^2}{2S}\,\xi^2 \qquad \text{(E-7)}$$

or

$$P_m = \frac{1}{2} A\rho c\,\omega^2\,\xi_m^2, \qquad \text{(E-8)}$$

where $Rc = A\rho c$ is the characteristic impedance of the coupler, A is the cross sectional area of the coupler, and S is the elastic standing-wave ratio ($S = 1$ for P_m).

Combining Eq (E-5) and (E-8) leads to the power equation:

$$P_m = \frac{1}{2} A \frac{\sigma_m^2}{\sqrt{E\rho}} . \qquad \text{(E-9)}$$

Thus, the maximum power that can be delivered by a transducer coupler system for welding appears to be independent of frequency and to depend upon the mechanical and physical properties of the material of which the system is made.

REFERENCES

1. Aeroprojects Incorporated, AEC Report No. DP-168, Jan. 1957, (CONFIDENTIAL).

2. Ibid., "Feasibility Investigation of Ultrasonic Welding as a Means for Joining Heat Exchanger Components", RR-56-50, Final Report on Pratt and Whitney-AEC Contract No. AT(11-1)-229, Oct. 1956. (Available from Pratt and Whitney Aircraft Div., United Aircraft Corp., East Hartford, Conn.)

3. Ibid., "Feasibility Study for Ultrasonic Roll-Bonding of Flat Plate Fuel Elements", RR-60-57, Final Report on Subcontract 1 of CEND-AEC Contract AT(30-1)-2379.

4. Ibid., "Fundamentals of Ultrasonic Welding", RR-59-105, Final Report on Contract NOas 58-108-c, May 1959. (Available from OTS as PB 16 1677.)

5. Ibid., "Further Developments in Ultrasonic Welding of Structural Aluminum Alloys", RR-58-35, Final Report on Contract NOas 57-480-c, Oct. 1958.

6. Ibid., "Ultrasonic Energy Applied to Aluminum Extrusion Cladding of Tubes", Report DP-418 on duPont-AEC Contract AT(07-2)-1, Nov. 1959.

7. Ibid., "Ultrasonic Welding of Aluminum", Report DP-107, duPont-AEC Contract AT(07-2)-1, Feb. 1955. (Available from LC.)

8. Ibid., "Ultrasonic Welding of Aluminum Alloys for Missile Use", RR-59-84, Final Report on Contract No. DA-36-034-ORD-2424, Aug. 1959.

9. Ibid., "Ultrasonic Welding of Metals", RR-55-30, Final Report on Contract DA-36-034-ORD-1403, April 1955. (Available from OTS as PB 131084.)

10. Ibid., "Ultrasonic Welding of Metals for Ordnance Applications", RR-56-14, Final Report on Army Contract No. DA-36-034-ORD-1665, Mar. 1956. (Available from ASTIA).

11. Ibid., "Ultrasonic Welding of Structural Aluminum Alloys", RR-57-13, Final Report on Navy Contract No. NOas 56-161-c, Jan. 1957. (Available from OTS as PB 131680.)

12. Aeroprojects Incorporated, Unpublished research, March 1955.

13. Aeroprojects Incorporated, Unpublished research.

14. Al'tan, E. A., "Ultrasonic Treatment ... olid Metals and Alloys for Accelerated Diffusional and Diffusionless Process." Nauchnyye Doklady Vysshey Shkely Metul urgiya, 1, 1959, pp. 19-24.

15. Barrett, Imperfections in Nearly Perfect Crystals, John Wiley and Sons, Inc., N. Y., 1952.

16. Battelle Memorial Institute, "Research and Development of Procedures for Joining of Similar and Dissimilar Heat-Resisting Alloys by Ultrasonic Welding", WADC Technical Report 58-479.

17. Blaha, F., and B. Langenecker, "Plastizitätsuntersuchungen von Metallkristallen in Ultraschallfeld". Acta Metallurgica, Vol. 7 (Feb. 1959), pp. 93-100.

18. Camp, J. M., and C. B. Francis, Making, Shaping, and Treating of Steel, Fifth Edition, Carnegie-Illinois Steel Corp. 1940.

19. Coker, E. G. and L. N. G. Filon, A Treatise on Photoelasticity, Cambridge U. Press, 1957.

20. Cottrell, A. H., "Theory of Dislocations", Progress in Metal Physics, Vol. IV, Pergamon Press Ltd., 1953.

21. Frocht, Max M., Photoelasticity, I and II, John Wiley and Sons, New York, 1941.

22. International Nickel Co., Design of Nickel Magnetostrictive Transducer, New York.

23. International Nickel Co., Magnetostriction, New York, April 1948.

24. Jhanke, Met. Progress 74, Nov. 1958.

25. Karnov, M. Ya., and S. N. Shestakov, "Vibro-Forging of Aluminum Alloys", Metallovedenie i Termich. Obrabotka Metallov, 1 (Jan. 1959), pp. 57-59.

26. Karnov, M. Ya., and A. A. Voronin, "Metal Forming by Vibration," Kuznechno-Shtampovochnoye Proizvodstvo, 3 (March 1960).

27. Lee, George H., An Introduction to Experimental Stress Analysis, John Wiley and Sons, New York, 1950.

28. Love, A. E. H., A Treatise on the Mathematical Theory of Elasticity, Dover Publications, New York, 1944.

29. McCarthy, D. J., Vladimir Pirc, and W. H. Hannaks, "Ultrasonic Welded Aluminum-Copper Junctions as Electrical Connections", In Reliable Electrical Connections, (Proc. of Third E I A Conf.), Interscience Pub., New York, 1958.

30. Mahoux, G., and L. Guillet, "Influence des oscillations a haute frequence sur les traitements des produits metallurgique", Comptes rendus, Académie des Science, Paris, 191 (1930), pp. 1329-1332.

31. Mason, W. P., Physical Acoustics and Properties of Solids, D. Van Nostrand Co., Inc., Princeton, N. J., 1958.

32. Mason, W. P., Piezoelectric Crystals and Their Application to Ultrasonics, D. Van Nostrand Co., Inc., New York, 1950.

33. Nevill, G. E., Jr., and F. R. Brotzen, "Effect of Vibrations on the Yield Strength of a Low-Carbon Steel," Technical Document No. AFOSR-TN-57-170, Rice Institute, Houston, Texas, Air Force Contract AF 49(638)-78, April 15, 1957.

34. Pogodin-Alekseev, G. I., "Influence of Ultrasonics on Diffusion Processes in Steels and Alloys at Elevated Temperatures," Metallovedenie i Obrabotka Metallov, 6, 1958, pp. 14-17.

35. Polonis and Par, J. of Met. Trans., May 1956.

36. Quenouille, M. H., The Design and Analysis of Experiment, Hafner Publishing Co., New York, 1953.

37. Shestakov, S. N. and M. Ya. Karnov, "Structure and Properties of Alloys (and Steels) After Vibrational Working." Metallovedenie i Obrabotka Metallov, 7 (July 1958), pp. 35-38.

38. Smith, P. H., "Transmission Line Calculator", Electronics, Jan. 1944.

39. Sogrishin, Y. P., "Vibrational Working of Metal." Metallovedenie i Termich. Obrabotka Metallov, 1 (1959), pp. 55-57.

40. Timoshenko, S., and J. N. Goodier, Theory of Elasticity, McGraw Hill, New York. 1951.

UNCLASSIFIED

UNCLASSIFIED